Theory and Production of Hyperpolarized Xenon Gas

by

Avner Fitterman

for the degree of

Master of Science

Graduate program in Physics

August 2015

Acknowledgements

I would like to thank my supervisor, Dr. Mitchell Albert, for giving me the opportunity to engage in science research, and for his support throughout my two years of Master's studies. I would like also to thank Dr. Alla Reznik and Dr. Hubert de Guise with whom I had interesting and constructive conversations.

I convey my sincere appreciation to Dr. Alexei Ouriadov and Dr. Matthew Fox who helped at the most critical point when my project was being formulated. Dr. Matthew Fox enriched my knowledge with topics related to MRI and HP gas.

I would like also to thank the members of Dr. Albert's lab. Special thanks are reserved for Mr. Marcus Couch, who was willing to help with the smallest concern with much kindness, and with whom I could always consult, and for Mr. Tao Li for the kind support.

Finally, I would like to thank Anthea Kyle and Patrick Gauthier from the Lakehead University Writing Centre who kindly helped me with the English writing.

Above all, I would like to dedicate this thesis and convey my love to my parents who devotionally support me even though they live on another continent.

Table of contents

A. Abstract

Conventional magnetic resonance imaging (MRI) modality is based on the magnetization that is formed by the influence of a strong polarizing magnetic field on the spin of protons, typically those of water molecules within the body. In Hyperpolarized (HP) gas MRI, a dramatic increase in spin polarization is achieved using spin-exchange optical pumping (SEOP), which allows images to be obtained with a high signal-to-noise ratio (SNR). Batch-mode custom-built polarizers can serve to produce the HP gas, however, such custom-built systems require optimization in terms of pressure and temperature parameters. This study is comprised of three objectives: i) Gaining understanding regarding the physics of the nuclear polarization process of ^{129}Xe; ii) Examining experimentally the pressure and temperature dependences of the polarization, similarly to the way it was done in previous studies; iii) Exploiting this knowledge for the benefit of the optimization of the custom-built polarizer in our lab.

B. Theory and Production of Hyperpolarized Xenon Gas

1. Introduction

Magnetic resonance imaging (MRI) is one of the leading technologies in medical imaging. Nevertheless, some MRI utilizations may undergo substantial upgrading by the introduction of hyperpolarized gas; the most eminent example is lung imaging where the MRI is not efficient. The hyperpolarized gas technique, which was developed during the 1990's, relies on an external source of hyperpolarization, and the optimization of a custom-built polarizer, which produces the hyperpolarized gas, is one of the main concerns of this project.

It should be disclosed that all the theoretical knowledge upon which this thesis is based was developed by previous studies. The experimental section is also based upon previous work, but only partially and only in its general ideas. See the end of the discussion section for precise disclosure regarding the sections that were contributed from previous work.

1.1 Principles of Magnetic Resonance Imaging (MRI)

1.1.1 Spin Dynamics

The basic idea behind the MRI modality is the magnetic resonance of the spin of protons. Unlike other modalities, such as Computerized Tomography (CT), Positron Emission Tomography (PET) and ultrasound that are based upon external source of radiation or sound waves, the MRI modality is based upon radiation originating from spin resonance. The concept of magnetic resonance of spin-1/2 particles can be discussed using different levels of accuracy, some relate more profoundly to quantum mechanics, and some based on a classical description [1-4]. Nevertheless, an important quantity for all of those descriptions would be the polarization vector having components defined as the expectation values of the spin components [5].

The spin resonance is obtained under the influence of a strong longitudinal magnetic field, and a small oscillating transverse magnetic field. Without the oscillating field, the longitudinal component of the polarization vector is constant over time, while the transverse component rotates about the longitudinal axis at the Larmor frequency. Even in a 3T magnetic field as in the present study, the ratio of the excess of spins that are aligned with the magnetic field over the spins that are anti-aligned, and the total number of spins is only a few parts per million (ppm). In the quantum mechanical view, that would be equivalent to the following: for each one of the spins, the probability of finding the longitudinal spin component in the spin up state is slightly higher than the probability of finding it in the spin down state. Since there is no preferred direction in the transverse plane, the rotations of the spins are completely out of phase, and thus, there is no net transverse component. The polarization is then completely aligned with the magnetic field (see figure 1.1a).

1.1.2 Flip Angle

In the presence of an oscillating magnetic field, the description becomes more convenient by transforming the system of coordinates to a new Cartesian system which rotates with the Larmor frequency about the longitudinal direction. In that system of coordinates the transverse component of the spin is constant over time (in the rotating wave approximation [1,2]), and the oscillating magnetic field acts as a rotation operator about the x (given a certain coordinate labeling) axis operating on the polarization vector (see figure 1.1b), given that it oscillates at the Larmor frequency that is usually in the radio frequency (r.f.) range. For spin-1/2 nuclei, the net magnetization, $\vec{M}$, is related to the polarization vector, $\vec{p}$, by [6],

$$\vec{M} = N\mu_B\vec{p}, \qquad 1.1$$

where *N* is the total number of spins and $\mu_B = \frac{e\hbar}{2m}$ (in MKS). The extent of the rotation of the polarization can be modulated according to the pulse duration and its amplitude. The angle that the net magnetization vector forms with the longitudinal axis after it has been rotated is known as the flip angle (FA). Since the frequency of rotation about the x axis depends on the power of the r.f. pulse, one may obtain different flip angles for the same pulse duration but for different r.f. pulse amplitude, and vice versa.

Regardless of the flip angle that was applied, there will be a break of rotational azimuthal symmetry. In the lab system of coordinates, the spins will start their rotation as they point towards a specific direction, and will continue to rotate about the longitudinal axis at the Larmor frequency, ideally with no phase accumulation (see figure 1.1b), namely, in unison. Hence the r.f. pulse forms a time-dependent net magnetization that in its turn, results in radiation at the rotation frequency, i.e. the Larmor frequency. The actual signal is,

$$s_\alpha(t) = s(t)sin\alpha\ , \qquad 1.2$$

where $s(t)$ is the signal obtained by applying a $\frac{\pi}{2}$ flip angle. The flip angle is denoted by α. However, as has been implicitly stated, realistically, there are processes that have to be considered in order to be more accurate in terms of an environmental influence which destruct the coherence of the spin precession.

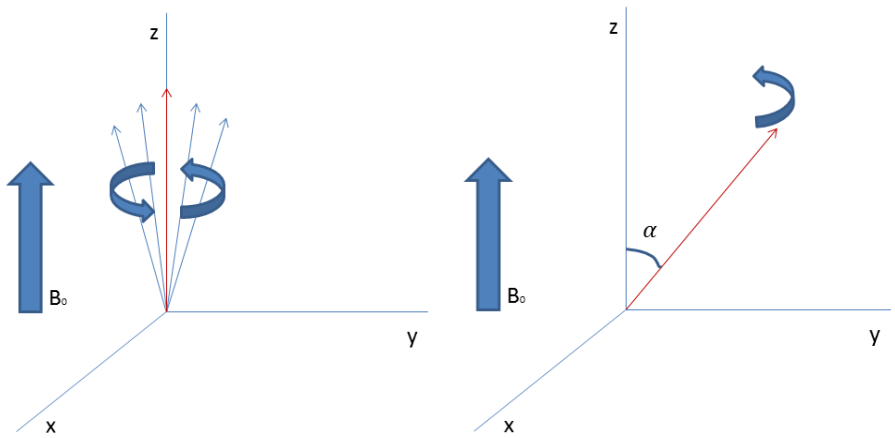

a b

Figure 1.1. The net magnetization is presented by the red arrow. **a** The spins are subject to a high longitudinal static magnetic field only. No net transverse magnetization is formed. **b** After the exertion of an RF pulse, net transverse component is formed.

The amplitude of the resonating r.f. magnetic field, denoted by B_1, and the duration of the r.f. pulse, τ_{rf}, determine the flip angle, according to,

$$\alpha(\tau_{rf}) = \int_0^{\tau_{rf}} \gamma_{Xe} B_1(t) dt \,, \qquad 1.3$$

where $\gamma_{Xe} = \frac{e}{2m_{Xe}}$ is the xenon gyromagnetic ratio (m_{Xe} is the mass of the xenon nucleus).

1.1.3 Preliminary Signal Process

The time dependent transverse component of the magnetization gives rise to radiation that serves as the signal from which an image or an NMR analysis will eventually be processed. The signal received by a coil is amplified and continues to the receiver. Since the information can only be processed in a digital format, the signal then continues to the analogue-to-digital convertor (ADC). However, as the voltage oscillates at a frequency of about tens of MHz, it is difficult to process it into digital information [4]. Therefore, the receiver reduces the frequency to about 1 MHz. In NMR experiments, a few MHz (in a 3T field) is the order of magnitude between two Larmor frequencies of two different types of nuclei. Hence, given a certain Larmor frequency, ω_0, and a reduction of a frequency, Ω, by the receiver, the new frequency,

$$\omega = \omega_0 - \Omega, \qquad 1.4$$

can be either positive or negative. The signal that will be presented will be then proportional to,

$$\tilde{s}(t) \sim e^{-\frac{t}{T_2^*}} cos(\omega t), \qquad 1.5$$

which does not distinguish between positive and negative frequencies (adding a phase or using a sine function will keep the frequencies (positive and negative) indistinguishable). However, knowing the sign

of the frequency may be crucial to determine the origins of a chemical shift, for example. Thus, a second role of the receiver is to create two signals in its output, $s_r(t)$ and $s_i(t)$, with a phase difference of $\frac{\pi}{2}$ between them, so that the signal can be presented as a complex number,

$$s(t) \sim e^{-\frac{t}{T_2^*}} e^{i\omega t}. \qquad 1.6$$

This presentation preserves the information regarding the sign of the frequency [4]. That information is stored in the phase between the real part of the signal and the imaginary part of the signal.

1.1.4 Relaxation

There are two relaxation mechanisms by which the ensemble of spins tends to return to the initial state before the application of an r.f. pulse: (1) de-phasing of the collective rotation of the spins (T_2), and (2) aligning back to the direction of the magnetic field (T_1). The time constant of the former is shorter than the latter, since once the longitudinal component has fully recovered, the question of whether coherence persists is meaningless.

The relaxation time T_1 is also known as the spin-lattice relaxation. It originates in the interaction of the spins with the electromagnetic environment [4]. The fact that different substances in a sample have different values of T_1, leads to the contrast in MRI [1]. After the application of an r.f. pulse, substances with a long T_1 will not produce as much signal as a substance with a short T_1. Cerebrospinal fluid (CSF) protons have a relatively long T_1 (i.e. 2.5 seconds) compared to fat protons (with T_1 of 0.2 seconds) [2] (see figure 1.2).

The transverse component decays due to spin interactions and inhomogeneity in the magnetic field. The coherence decay constant refers to the actual decay, which includes both of the causes, is known as the free induction decay (FID), and is denoted by T_2^*. Typical values for T_2 and T_2^* are hundreds and tens of milliseconds, respectively [2]. However, the T_2 of the signal can be recovered by application of a spin-echo pulse sequence, where each coherence recovery can be exploited for another signal readout used for the image construction.

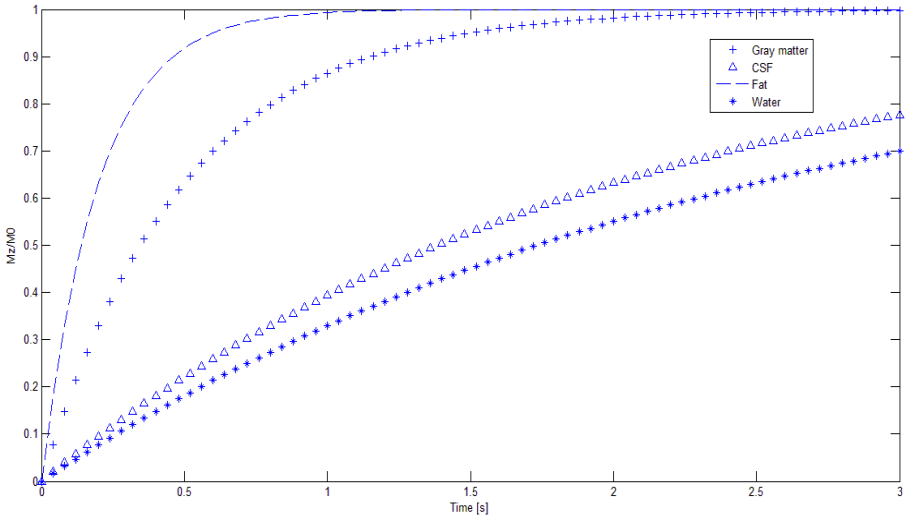

Figure 1.2. Different T_1 characteristic curves. A T_1 curve refers to the longitudinal magnetization immediately after an RF pulse was exerted. The next RF pulse will give rise to the contrast due to the differences in the recoveries that presented in this figure. Adapted from reference [2].

1.1.5 Thermal polarization in Image Acquisition

The longitudinal polarization is an important quantity for estimating the signal to noise ratio (SNR). The longitudinal polarization is related directly to the number of spins participating in producing the polarization. With basic statistical physics considerations, it can be shown that the excess in spins which are at up state over those which are at down state, is given by [7],

$$1.7 \qquad N_+ = N_\uparrow - N_\downarrow = Np = N \cdot tanh\left(\frac{\mu B_0}{\tau}\right),$$

Where B_0 is the magnetic field; N is the number of spins in the sample; $\tau = k_B T$, where T is the temperature and k_B is Boltzman constant; p is the thermal average of the polarization, defined as the excess of the spins at up state over the spins at down state, divided by the total number of spins[1].

In order to exploit eq. 1.7, it is useful to expand it under the condition $k_B T \gg \mu B_0$ that applies to a 3T field at room temperature ($\frac{\mu B_0}{k_B T}$ is about few parts per million), corresponding to the conditions in this study. The expansion results in,

$$1.8 \qquad N_+ \cong N\frac{\mu B_0}{k_B T}.$$

The expression for the signal produced at a point $\vec{r}$ inside the sample can be obtained by taking the time derivative of the magnetic flux through the coil (Faraday's law). The flux, on the other hand, depends on the transverse magnetic field received in the coil per unit current, $\mathcal{B}_\perp(\vec{r})$. This leads to the following expression of the signal produced within a voxel ΔV that contains the point $\vec{r}$ in it [1],

[1] An equivalent and more formal definition of the polarization will be given in section 2.1.2.1.

1.9 $\Delta s(\vec{r}) \sim N_+ \mathcal{B}_\perp(\vec{r}) \Delta V.$

As expected, the signal is proportional to the excess in spins in the up state, and therefore so is the more practically meaningful quantity of the SNR. In order to evaluate the latter, a thermal white noise will be assumed [1],

1.10 $\sigma = (k_B T \cdot R \cdot BW)^{\frac{1}{2}},$

where *R* is the coil resistance and *BW* is the bandwidth of the RF pulse. Thus, the SNR is just eq. 1.9 divided by eq. 1.10,

1.11 $SNR \sim \frac{N_+}{BW^{\frac{1}{2}}}.$

It is evident from eq. 1.9 that there is a trade-off between the signal intensity and the resolution. However, if one of the dimensions of the voxel is decreased by a factor a, the SNR will decrease only by a factor $\sqrt{a}$ given that it was decreased by reducing the bandwidth, due to the fact that each dimension of the voxel is given by [2],

1.12 $\Delta x = \frac{BW}{\gamma G_x N_x},$

where γ is the gyromagnetic ratio, G_x is the x component of the magnetic field gradient, and N_x is the number of voxels in the x direction. According to 1.11, the SNR will decrease only by a factor of $\sqrt{BW}$ as was stated.

As noted above, a higher SNR can be achieved by reducing the resolution. One way to reduce the effects of this trade-off is by acquiring more images and then averaging them. However, this approach has its drawback too: it multiplies the acquisition time by a factor of the number of averages. Since the SNR is proportional to the magnetic field, a gain can be achieved by using higher fields. However, the exposure of the human body to high magnetic fields involves higher specific absorption rate (which is proportional to the squared of the external magnetic field), a measure for the rate of energy absorption by tissues per unit mass [8]. All of these considerations can be evaluated with respect to the needs of the specific acquisition. Nevertheless, a pure gain in the SNR, that can be translated to improve any of the parameters mentioned above (SNR, resolution, acquisition time), can emerge if somehow N_+ can be increased. The fact that this parameter is independent of all the others, assures that no trade-off will occur.

1.1.6 Chemical Shift

The slight deviation from the nominal value of the magnetic field in the vicinity of the spin is known as chemical shift, as it stems from the chemical environment characterizing the atomic or molecular structure of which spin particle is part.

The local magnetization at a certain point in the sample can be assumed to be proportional to an oscillatory function, such as [6],

1.13 $$m(t) = m_0 e^{i\omega t},$$

where ω is the local Larmor frequency. The position of this point in the sample can be uniquely determined by the relative phase of the magnetization, given that the sample is in the presence of gradients. Hence, the spatial dependence in eq. 1.13 can be given by expressing the Larmor frequency in terms of the magnetic field, and the magnetic field in terms of the gradient. Given an initiated gradient G and a gradient, *G',* which is associated with a slightly different magnetic field resulting from a different chemical environment, the phase in eq. 1.13 can be written as,

1.14 $$\emptyset(x) = k_x x\left(1 + \frac{G\prime}{G}\right),$$

where the quantity $k_x = \gamma G t$ is defined. This quantity, along with its equivalent in the y direction, constitutes the coordinate system of the 'k-space', from which the image is constructed by Fourier transform. Note that k_x depends on time, but this time cannot exceed $2\pi/\gamma G L$ (setting *G'*=0 for simplicity, and where L is the dimension of the sample), because otherwise, the Nyquist condition[2] cannot be met. Certain objects in the image obtained from an area with a different chemical environment with respect to the rest of the sample, will be shifted according to

1.15 $$x' = x\left(1 + \frac{G\prime}{G}\right),$$

where x is an arbitrary point that represents the position of the shifted object (or locally speaking, the voxel) without chemical shift.

The chemical shift can be expressed in terms of the Larmor frequency and the slight variation in the magnetic field, δB, which is small in comparison to the external magnetic field,

1.16 $$\omega = -\gamma(B + \delta B).$$

In other words, there is a small correction to the Larmor frequency that stems from a contribution to the longitudinal magnetic field that is not from the initiated magnetic field.

The slight deviations from the nominal value of the magnetic field can be explained in terms of the bound currents induced by the external strong magnetic field. The intra-molecular currents that it produces create a residual weak magnetic field in the vicinity of spins in the same molecule, spins that are used for MRI. The resultant induced magnetic field is generally not in the direction of the external field. The tensor that relates those two fields together depends on the symmetry properties of the sample [4]. For anisotropic samples, for example crystals, the magnitude of the energy correction in eq. 1.16 will depend on the angle between the external field and the symmetry axes. However, in liquid samples (and gas) it can be assumed that the sample is isotropic, an assumption that can be justified by the fact that the molecules are moving freely in the sample.

[2] The Nyquist sampling rate restricts the maximal frequency that the RF pulse can contain by the sampling rate. Frequencies above that maximal frequency will not contribute information that wasn't included in the lower frequency and the image will contain artifacts known as 'wrap-around'.

Another source of chemical shift emerges from interactions between two adjacent nuclear spins [4]. The two adjacent nuclei usually belong to atoms of the same molecule, and consequently, the spectrum that corresponds to the various interactions of a certain nucleus can provide information regarding the molecular structure [9].

1.2 Utilization of Hyperpolarized (HP) Gas

1.2.1 Principles

Hyperpolarized (HP) gas MRI was developed in 1994 by Albert *et al* [10]. Instead of relying on thermal polarization created by proton spins in the human body, this technique exploits an external source of polarization, that is, the HP gas. HP helium-3 (^{3}He) or xenon-129 (^{129}Xe) is inserted into the region of interest and it dramatically increases the signal in comparison to the signal that is acquired by the thermal polarization of proton spins. In order to have gas in such a hyperpolarized state, it has to go through a process in which it is being polarized. That process is the main concern of this study.

There are three main domains where conventional MRI can be significantly improved by the utilization of HP gas: (1) lung imaging, (2) brain imaging, and (3) molecular imaging [8].

Perhaps the most basic demonstration of an HP gas utility is with lung imaging. There is a vast presence of air in the lungs and a very low density of water protons; therefore, the thermal signal is insufficient for detection, and that is the reason behind the observed dark areas in a chest MRI image (see figures 1.3a and 1.3c). With HP gas MRI, the subject lies down in the MRI magnet bore and HP gas is inhaled into the lungs, thereby giving rise to a substantially larger signal that is observed from areas where the gas reaches [11,17]. The oxygen in the lung is absorbed at the alveolus and reaches other parts of the body through the blood stream. If the ^{129}Xe nuclei remain polarized long enough, a signal can be obtained from other parts of the body, including the brain, which is the most highly perfused organ in the body.

Hyperpolarized gases, and specifically HP xenon gas, can serve in magnifying the signal in cases where high sensitivity is needed, such as in chemical shift experiments [9]. This becomes possible due to the high sensitivity of xenon to the electronic environment, which manifests in variation of the magnetic field in the vicinity of the xenon nucleus (denoted as δB in eq. 1.12). In other words, the value of the Larmor frequency is highly dependent on the environment [4]. Hyperpolarized chemical exchange spin transfer (HyperCEST) is a technique that exploits this feature (see section 1.2.4).

1.2.2 Lung Imaging

Although the lack of protons in the lungs provides sufficient reason to search for a new approach, there are additional reasons that make the lung region difficult to image. One of them is the fact that the lungs are prone to movement. The issue of lung movement can be resolved to some extent by having the subject to hold his breath, which limits the time of signal acquisition. Moreover, another source of movement that affects lung imaging is the patient's heartbeat. The fact that the heartbeat is

not controllable by the subject also conceals an advantage: the regular periodicity of the movement can be taken into account in the pulse sequence design, or in the post image processing, and can be cancelled [2]. However, both the motion of the lungs and heartbeat can never be resolved completely, and artifacts will always manifest to a certain extent.

Another fundamental issue which causes artifacts is the magnetic susceptibility [1]. The lung's structure poses difficulty due to the large interface of the alveolar tissues with the air. The alveoli and the air are entangled with each other in a complex manner which spans over an order of magnitude of only a few hundred microns [12]; this entanglement results in a severe reduction in the FID time constant, so that the signal does not persist long enough to be exploited.

A priori, the signal intensity that gas can produce is smaller compared to a solid or liquid sample. Although the gas density is 3-4 orders of magnitude smaller than the density of soft tissues, the polarization that can be achieved with HP gas is of 4-5 orders of magnitude larger than the thermal polarization, so that it compensates the lower density of the gas.

Among the disadvantages of HP gas usage is the limiting depolarization time. On top of that, the non-renewability of the polarization presents an additional disadvantage. Thus, an alternative approach using inert fluorinated gases has been developed [13] (which also does not require the cost of a polarizer). While thermal polarization is recoverable after the application of an r.f. pulse, the HP gas polarization has to be wisely consumed. Therefore, low flip angles are typically used in HP gas MRI, so that much of the longitudinal magnetization will be preserved.

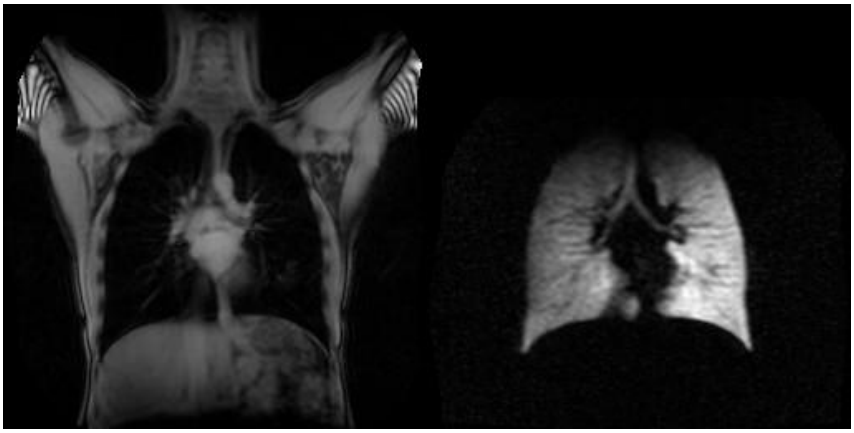

a **b**

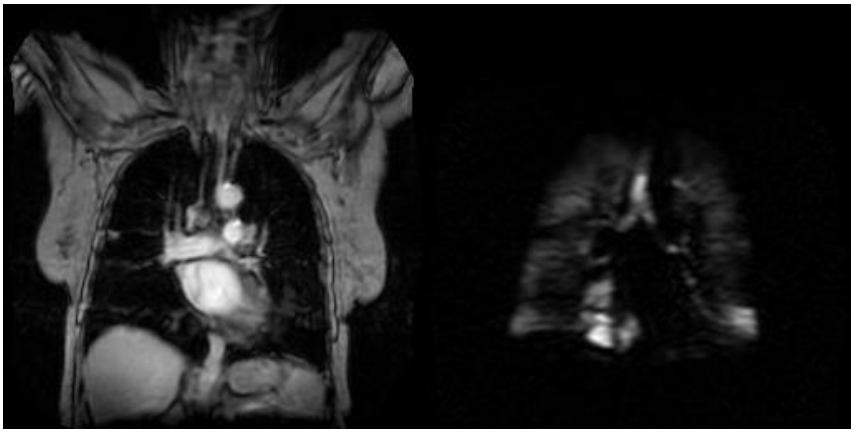

c **d**

Figure 1.3. **a** and **c**: A conventional proton MRI. **b** and **d**: A HP helium gas MRI. The top row images were taken from a healthy volunteer, and the bottom row were taken from a chronic obstructive pulmonary disease (COPD) patient. The images were taken at the Thunder Bay Regional Research Institution.

Hyperpolarized gas MRI can provide localized functional information [8, 12, 14]. An additional benefit to using HP xenon gas for the purpose of lung imaging is through exploiting the chemical shift (see sections 1.1.6) and distinguishing between a signal that originates in xenon in the gas phase, and xenon that originates in the dissolved phase [15,16,19]. That way, an image of only xenon that had been dissolved in the blood can be obtained, thereby giving functional information regarding gas exchange in the lungs [18].

Localized functional information can be used as an efficient tool to monitor the response of the lungs to a variety of different treatments, as the air accessibility to different areas in the lung can be examined. Although the image resolution may not be as good as in CT scans, important parameters for assessing the lung functionality that cannot be obtained by CT, can be obtained by HP gas MRI. Monitoring the development of lung diseases is crucial for research and for saving lives. However, CT scans for adults are severely limited, and avoided completely for children due to the ionizing radiation that it involves. Therefore, finding a substitute for CT, such as HP gas MRI that does not involve ionizing radiation, can accelerate research by providing more frequent information from the same subject and potentially save lives.

1.2.3 Brain Imaging

In the case of lung imaging, there is a satisfactory substitute for a HP xenon gas, that is a HP ^{3}He gas. The latter is obtainable in a similar SEOP method, and its polarization is characterized with longer T_1. However, the ^{3}He, besides being much more scarce and expensive than xenon, is not soluble in blood, and therefore cannot be transferred through the blood stream into other body organs. Besides being soluble, xenon is highly effected by the electronic environment, and consequently has a high range of chemical shift (200 ppm, whereas a proton has a range of 5 ppm [4]). That property makes the utility of xenon in brain imaging an excellent tool with respect to several aspects of brain imaging.

One of these aspect is related to the previously described chemical shift. The xenon that reaches the brain is expected to produce a signal originating from different chemical environments that may be detectable in the resultant NMR spectrum with different distinguishable peaks. The intensity of each peak is related to the concentration of each of the substances corresponding to its specific chemical environment. The presence of a certain substance can indicate irregularities and diseases [20].

Another effect that the blood environment has on the polarization however is a substantial decrease of T_1 value. While in the gas phase, T_1 is of the order of tens of minutes, dissolved in the blood T_1 is about a few seconds. In the presence of oxygenated blood, T_1 is around 9 seconds, while in deoxygenated blood, T_1 is around 3 seconds [22, 23]. The longer T_1 in the oxygenated blood environment can be accounted for the fact that the depolarization in the blood occurs due to the presence of an iron atom in the haemoglobin, where its magnetic property is being mitigated by the presence of oxygen [1]. The relaxation time of HP gas in oxygenated blood, amounting to a few seconds, is comparable to the amount of time needed for the blood that is absorbed in the lung to reach the brain. So practically, in HP gas brain MRI, one works with the remnants of the polarization.

The aspects described above are some of the reasons for of the importance of increasing the polarization rates. Moreover, once the image relies on a signal source that is not inherent to the biological components, the signal will lack the background noise. However, due to the limited time of signal availability, the use of HP gas brain imaging is still in a preliminary stage.

1.1.4 Hyperpolarized Chemical Exchange Spin Transfer (HyperCEST)

In this imaging technique, a special kind of molecules that serve as a biosensor, is selectively attached to cells that one hopes to detect by spectroscopic analysis or imaging [9]. Those molecules are designed to trap a xenon atom by their unique structure that resembles a cage or a bowl. Due to the different electronic environment inside that structure and the large range of NMR frequencies of xenon, the Larmor frequency of xenon inside the structure will deviate significantly from the Larmor frequency of xenon in the dissolved or the gas phase. This fact makes those molecules detectable [24].

Hence, one expects to find two peaks in the NMR spectrum of a sample that includes dissolved xenon and cage molecules: one large peak that corresponds to most of the ^{129}Xe nuclei from the dissolved phase, and another smaller peak that corresponds to xenon atoms that are trapped in the molecular structure. The peak associated with the trapped xenon may be so small such that regular NMR spectroscopy is not sufficient for determining whether it is noise, or indeed originated in trapped xenon.

To resolve this issue, saturating pulses are exerted exactly on the frequency that is suspected to be the frequency of the trapped xenon, causing a destruction of the longitudinal polarization of xenon in the structure. If the suspected frequency is the frequency of the trapped xenon, after repeating this process several times, the large peak that is associated with the xenon in the dissolved phase should be reduced due to spin exchange between the dissolved xenon and xenon that is in the structure, as the xenon that returns to the dissolved phase returns depolarized. Hence the reduction in the dissolved phase signal implies that the biosensors are present in the sample, or the human body [25].

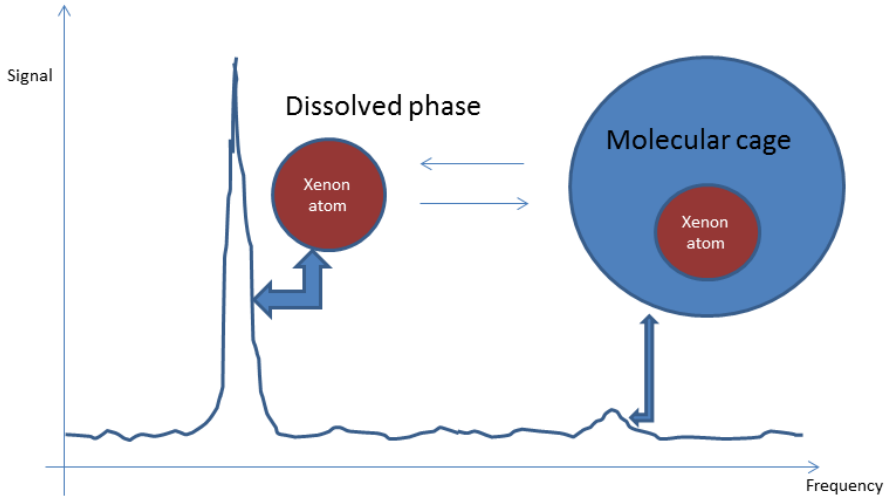

Figure 1.4. The NMR spectrum of a HyperCEST experiment. The large peak corresponds to xenon in a dissolved phase, and the smaller peak corresponds to xenon in a molecular cage. Repeated saturation pulses of the later will cause signal depletion from the dissolved phase peak.

1.3 Spin-Exchange Optical Pumping (SEOP)

So far, the utilization of HP gas was demonstrated, but only the physics of the conventional proton MRI (and its limitations) was discussed. According to this discussion, it is evident that the nature of the HP polarization is completely different: it does not rely on an external magnetic field and the T_1 in the context of HP gas refers to the decay of the longitudinal component of the polarization to thermal polarization (in the case of proton polarization, the T_1 relaxation was associated with the regrowth of the longitudinal component of the thermal polarization). Moreover, and most importantly, the hyperpolarization state corresponds to a polarization level that is approximately 10^5 larger than the thermal polarization in a conventional MRI. The goal of the spin-exchange optical pumping (SEOP) process is to form a high level of polarization based on the spin of the ^{129}Xe nuclei, which like the protons, are spin-1/2 particles.

The SEOP is one of two ways in which such polarization can be produced. Another way, which is a direct way, applies to the ^{3}He nucleus. It is direct in the sense that a laser beam causes the helium nuclei to form polarization by a direct interaction with helium atoms. In this method, the laser light excites the helium's valence electron to an excited state from which it decays into a metastable state. The long duration of the electron in the metastable state permits the hyperfine interaction to be sufficiently effective for the angular momentum to be transferred to the nuclear spin (thus, it is called meta-stability exchange optical pumping) [26]. However, that approach is impractical since it is feasible only at very low ^{3}He pressures, and it cannot be used to optically pump ^{129}Xe nuclei.

In this work, polarization of xenon ^{129}Xe nuclei by the indirect process of SEOP is discussed [27]. In this process, the light polarizes alkali metal atoms (in this work, rubidium) by the excitation to the

$^2P_{\frac{1}{2}}$ energy level and the decay back to the ground state, in a process known as optical pumping. The rubidium gas resides in a cell with the xenon gas that is not directly affected by the laser light. As the rubidium atoms become polarized, the collisions between rubidium and xenon atoms result in angular momentum transfer from the rubidium atoms to the xenon nuclei. Steady state in terms of the xenon nuclear polarization is achieved after several minutes. Then, as the gas leaves the cell, a rubidium filter purifies the sample from rubidium and the gas is ready to be used.

1.3.1 Theory

The appendix of this work concerns mainly the physics of the SEOP. However, it is beneficial to provide in this section a general overview on some physical aspects that concern the experimental work.

Given that the optical pumping rate is γ_{op} and the rubidium spin destruction rate is Γ_{sd}, the rubidium polarization is given by (see section 5.2.5),

$$1.17 \qquad p_{rb} = \frac{\gamma_{op}}{\Gamma_{sd}+\gamma_{op}}\left(1 - e^{-t(\Gamma_{sd}+\gamma_{op})}\right).$$

In order to relate the ^{129}Xe polarization to the rubidium polarization, one can use the relation between the latter to the expectation value of the z component (where z is the direction of the external magnetic field) of the ^{129}Xe's nuclear spin. This relation can be expressed as [61],

$$1.18 \qquad \frac{d}{dt}\langle K_z\rangle = -(T_{SE}^{-1} + \Gamma)\langle K_z\rangle + \frac{\hbar}{2}T_{SE}^{-1}p_{Rb},$$

where Γ is the xenon polarization relaxation rate and T_{SE}^{-1} is the spin exchange rate between the rubidium and the ^{129}Xe (see section 5.3). Given a completely unpolarized initial state, and the fact that $\langle K_z\rangle = \frac{\hbar}{2}p_{Xe}$, the solution for 1.18 will be,

$$1.19 \qquad p_{xe}(t) = p_{Rb}\frac{T_{SE}^{-1}}{T_{SE}^{-1}+\Gamma}\left(1 - e^{-(T_{SE}^{-1}+\Gamma)t}\right),$$

and for the steady state,

$$1.20 \qquad p_{xe}(t \to \infty) = p_{Rb}\frac{T_{SE}^{-1}}{T_{SE}^{-1}+\Gamma}.$$

Two processes may contribute to the spin exchange rate (see section 5.3): binary collisions and three-body collisions between rubidium atoms to xenon atoms. These two terms can be extracted using the theoretical expression that was derived in [61],

$$1.21 \qquad T_{SE}^{-1} = [Rb]\left[\frac{\gamma_M\zeta}{[Xe]}\left(\frac{1}{1+0.275\frac{P_{N_2}}{P_{Xe}}}\right) + \langle\sigma v\rangle\right].$$

The first term accounts for the spin-exchange due to the formation of VDW molecules via 3-body collisions; $\gamma_M = \left(\frac{\alpha\kappa}{\hbar}\right)^2\frac{1}{Z}$, where *Z* is a constant associated with the rates of formation and disassociation

of the VDW molecules, and κ is the chemical equilibrium constant, given by $\kappa = \frac{[RbXe]}{[Rb][Xe]}$; ζ is a parameter that emerges from the spin-exchange equations that were discussed in section 2.3.2. The factor $\frac{1}{1+0.275\frac{P_{N_2}}{P_{Xe}}}$ accounts for the presence of nitrogen as a buffer gas, and was derived in [62]. The second term is explained through eq. 1.21 in the appendix. By the dependence on the rubidium density, the value of the total spin-exchange rate can be extracted, using dynamic measurement of the polarization decay curve. For different values of rubidium density, the slope of the decay constant will be the spin-exchange rate per rubidium density. That process can be done multiple times with different values of xenon partial pressure, and thus similar to the way that the spin exchange-rate was extracted, the contribution from the spin exchange via 3-body collisions can also be extracted. It is reported in [63] that the decay constant dependence of the rubidium density was as predicted; however, the spin-exchange rate dependence on the xenon partial pressure did not present the expected trend. To account for this discrepancy is a topic for a future work.

In terms of the temperature, experiments show that for a given xenon and buffer gas pressures, there is an optimal temperature where the maximal polarization value is obtained [63-67]. In the lower temperature limit, the density of the rubidium vapour is too low to form ^{129}Xe polarization. In the limit of the high temperature, the spin destruction becomes dominant and the spin transfer deteriorates. For optimal temperature and xenon partial pressure of about 0.5 Atm with total cell pressure of about 3 Atm, considerably high levels of polarization were achieved, mainly for high power pumping light. For pumping light of 200 W, around 90% and more ^{129}Xe polarization was obtained [64-66]. In terms of variable partial xenon pressure with constant total cell pressure and nitrogen being the other gas in the cell, lower xenon pressure is expected to give rise to higher ^{129}Xe polarization, which is also due to the increasing significant of spin exchange through the 3-body collisions channel [63, 64]. Moreover, it was found [63] that higher xenon pressure gave rise to a lower optimal temperature. This inverse relation is not fully understood.

To conclude, three main characteristics are expected from the dependencies of the ^{129}Xe polarization with respect to the temperature and the xenon partial pressure: (i) an optimal temperature should be obtained (regardless of the xenon partial pressure) in which the polarization is maximal, (ii) higher ^{129}Xe polarization is expected to be obtained for lower values of xenon partial pressure, and (iii) a higher optimal temperature for lower partial xenon pressure is expected.

The purpose of this project is to examine these dependencies, and by doing so, to provide a comprehensive procedure for optimizing a batch-mode xenon polarizer. Although the work is essentially experimental, an elaborative coverage on theoretical selected topics and aspects of the hyperpolarized gas physics is provided in the appendix.

1.3.2 Logistic Setups

Any polarization mechanism that is based upon SEOP can be achieved by two primary methods: in the first one, the gas mixture that contains the xenon continuously flows through a cylindrical tube that contains the alkali metal gas; as the mixture passes through the tube it is being polarized and an

outflow of hyperpolarized xenon can be continuously collected. This method is known as continuous-flow [28-30]. The method that is discussed in this project is known as batch mode, in which the gas mixture is inserted into a cell with the alkali metal gas, the cell is then being sealed and the polarization process takes place in a static state.

Not all the xenon nuclei can contribute to the polarization. ^{129}Xe consists 26.4% of the natural abundance xenon gas. Furthermore, as was previously implied, sometimes the xenon is more efficiently polarized in a mixture with other gases, mainly nitrogen and helium. The xenon portion in this study ranges from 100% to about 1%, but basically the polarization rates tend to deteriorate as the concentration of the xenon increases. In order to address the first difficulty, the xenon can be enriched, and thereby the fraction of ^{129}Xe isotope will be larger. However, this is not always done, since the cost of the enrichment increases exponentially with the enrichment percent. The second difficulty can be overcome by isolating the xenon from the mixture in a method called freeze-and-thaw [31]. In this method, the mixture is let into a glass tube (called a cold finger) that is placed in liquid nitrogen. The temperature inside the tube drops, such that the xenon freezes and the other gas components remain in the gas phase and continue to flow out to the atmosphere. Above certain levels of xenon-to-total-gas density ratio, the freeze-and-thaw method becomes uneconomical in terms of the xenon polarization because the polarization rates deteriorate during the time it is being performed, although the polarization relaxation time constant of xenon in the solid state is longer in comparison with xenon in the gas phase [31]. However, since the xenon has to go through a liquid phase which has a large polarization relaxation rate, the polarization level may be reduced dramatically. In order to minimize the polarization lost, the xenon is brought back to the gas phase by placing the cold finger it in boiling water, to minimize the time the xenon spends in the liquid phase.

2. Methods

2.1 Xenon Polarizer

2.1.1 Overview

The experiments were conducted on a custom-built polarizer situated near the MRI scanner (see diagram 2.1). The polarizer is consist of several components that were combined together previously in our lab: (1) a semiconductor laser with detection devices and a fiber optic connected to (2) a quarter wave plate. From the quarter wave plate, the radiation is directed into (3) a glass cell where the SEOP takes place. The cell resides between (4) two Helmholtz coils that produce the magnetic field. Finally, (5) a pipe system that includes oxygen and rubidium purifiers, gauges and valves, connects the cell to specific gas tanks, according to the need. A summary of the polarizer structure can be found in figure 2.2.

The gas mixture that ultimately serves as the HP gas sample was formed inside the cell. Once the mixture had been prepared, the temperature was set to the desired level, the laser was turned on and the polarization process took place. At the end of the process, the gas was collected into 150 ml Tedlar and was then transferred to the MRI scanner to measure the polarization.

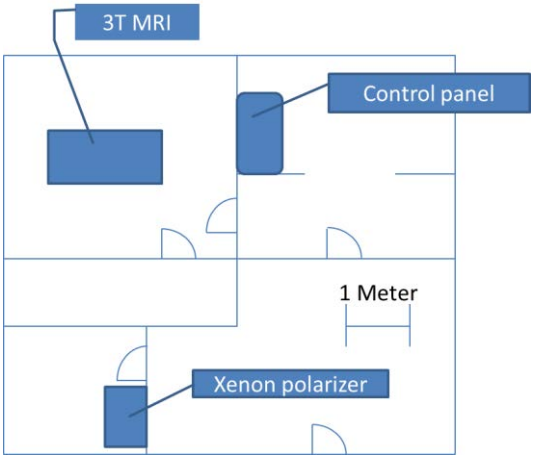

Figure 2.1. A schematic of the laboratory space containing the polarizer, MRI, and control panel.

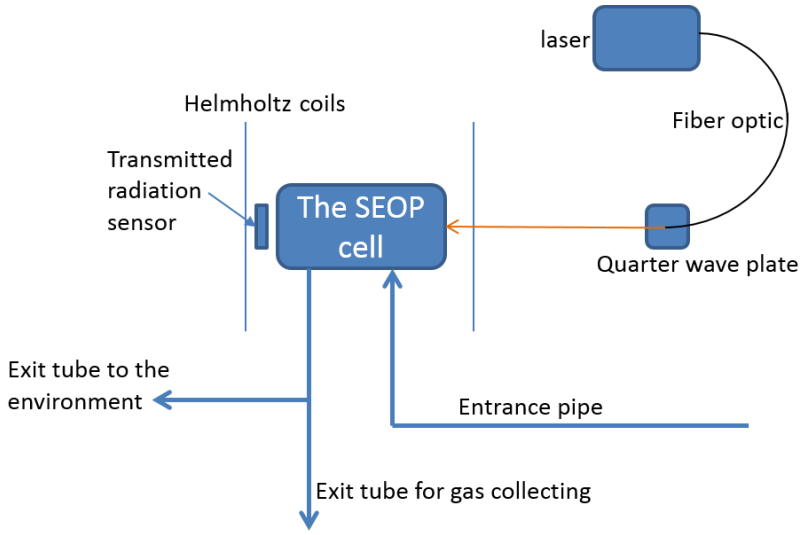

Figure 2.2. The polarizer's arrangement. The light beam produced by the laser reaches the quarter wave plate through the fiber optic and continues in open air to the cell. The cell resides between two Helmholtz coils and has two gates; one for letting gases in, and the other for depleting the gas mixture either to open air, or to be collected in a Tedlar bag.

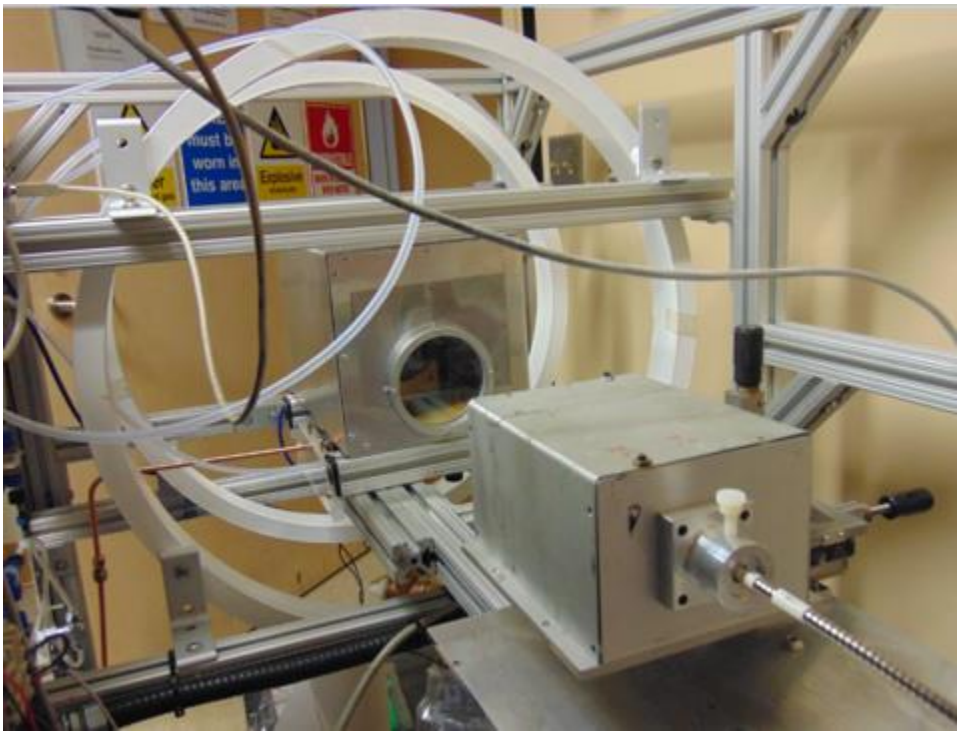

Figure 2.3. The Polarizer setup. The fiber optic can be seen in the bottom-right, guiding the laser beam into the quarter wave plate inside the near box. The laser beam continues to the round-shaped glass window of the oven where the SEOP cell resides. The white rings encircling the oven are the Helmholz coils.

2.1.2 Laser and Sensors

The Laser is an Integra MP industrial semiconductor laser manufactured by Spectra-Physics Company. The nominal power level of the beam as it enters the optic fiber is 60 W, with a nominal wavelength of 794.7 nm and a narrow spectral line of 0.2 nm. The laser is controlled by a laptop with a unique program developed for that laser (see figure 2.4).

Two detection systems provided information on light intensity. The first one is a powermeter head (PMH) that is manufactured by Coherent Company. The PMH is manually inserted to the path of the light beam before it enters the cell (in figure 2.2 that path is represented by a red line). Once the PMH is situated there, the light beam hits a lead surface and the power associated with the light is converted into a voltage with each 40 mV corresponding to 1 W.

The measurement that was described above aims to monitor the incoming radiation, but contains no information about the optical property inside the cell. As will be discussed in section 2.3, detection of the transmitted light through the cell provides information from which the rubidium polarization can be evaluated. For that purpose, a sensor that was installed in the back of the cell, converts the light power into electric current. The data is read as "counts", which represents the number of photons that have hit the sensor per unit time. The sensor is also sensitive to the frequency of each photon. Thus, a spectrum is produced. The spectrum presents a continuous distribution of the counts with respect to the frequency.

For illustration purposes, the light spectrum at room temperature (with negligible rubidium vapour in the cell), is presented in figure 2.4.

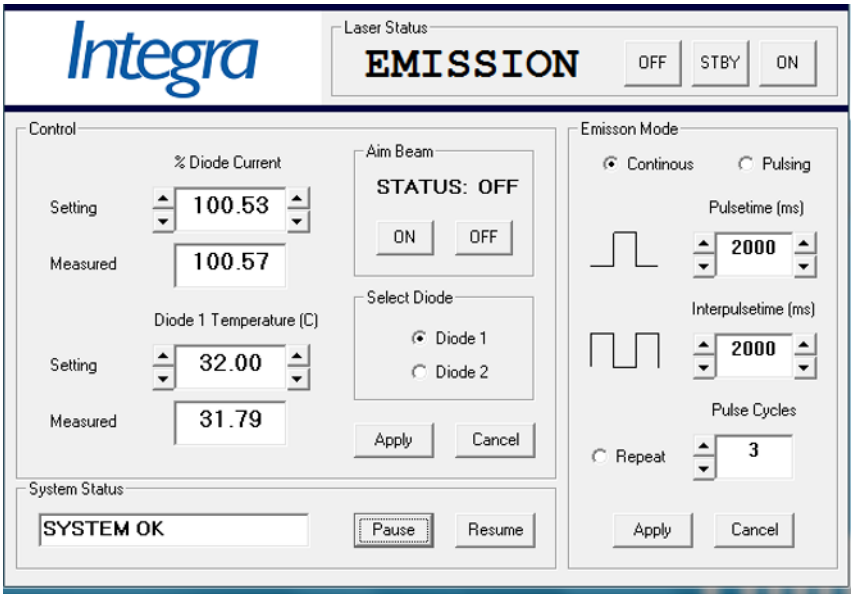

Figure 2.4. The Integra program to control the laser parameters.

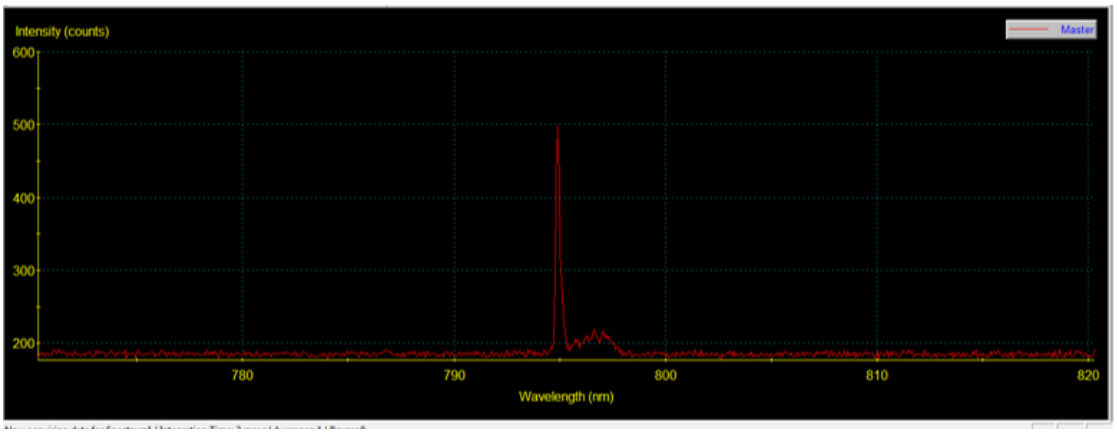

Figure 2.5. The laser light spectrum at room temperature. At the temperature maximal counts is obtained.

2.1.3 The SEOP Cell

The main component of the polarizer where the actual polarization process takes place is the SEOP cell. It is a glass cell with a measured volume of 265±11 ml, and that was purchased from Polarean Company.

Two g of liquid rubidium resides permanently inside the cell. The melting point of rubidium is 39.45^{0}C, so as long as the cell is at room temperature, the rubidium is in a solid phase, and cannot act in intermediating the angular momentum. Above the melting point temperature, it is assumed that the rubidium gas density is governed by the saturated vapour density [76],

$$[Rb] = \frac{10^{10.55-\frac{4132}{T}}}{1.38\cdot 10^{-16}T}[cm^{-3}]. \qquad 2.1$$

The saturation assumption means that the two phases of the rubidium, liquid and gas, are in equilibrium with respect to one another; for each atom of rubidium that leaves the liquid phase, there is one that enters the liquid phase.

Creating the rubidium vapour is the main reason for heating the cell. The heat is produced by a resistor situated beneath the cell. The heat is transferred by an airflow that also distributes the heat approximately uniformly across the cell's outer surface. The airflow also provides a safety net in case the thermostat fails. Without the airflow, the temperature may rise to dangerous levels that might damage the cell. Although the airflow poses a limitation on the maximal temperature that can be achieved (about 170^{0}C with the laser on), it is a necessary safety measure. Moreover, an electronic sensor was installed which stops the current in the resistor in case the airflow stops.

A temperature sensor is taped into the cell from the outside, which can be seen in figure 2.6. Since the sensor is taped to the cell from the outside, the temperature reading only approximately reflects the actual temperature inside the cell. A more precise evaluation should take into account the fact that thermal conductivity of the glass is not ideal.

Figure 2.6. The SEOP cell inside the oven seen in figure 3.3. The entrance and the exit gates are seen on the top of the cell (with a stabilizing rod between them). The white wire connects temperature sensor. The heat supply emerges from below. The gray hue inside the cell is the rubidium.

The maximal pressure that has been employed in the cell was about 3.5 atmospheres. The reason for the upper limit is simply to avoid pressure that might jeopardize the stability of the glass.

2.1.4 Gas Circulation System

The gas mixture in each batch was nourished from either a tank that contains a lean xenon mixture, a tank that contains pure xenon, or from two tanks, one containing pure nitrogen and the other pure xenon. The lean xenon mixture composed out of 1% xenon, 10% nitrogen and 89% helium.

The gas circulation system was designed such that the cell interior can be exposed to any of the tanks' content with the intermediary of the oxygen purifier. Moreover, each pipe segment is in contact with a vacuum pump, so that the pipes can be vacuumed from their gas content according to the need. The SEOP cell, the oxygen purifier and the rubidium purifier can be protected from the vacuum operation by valves.

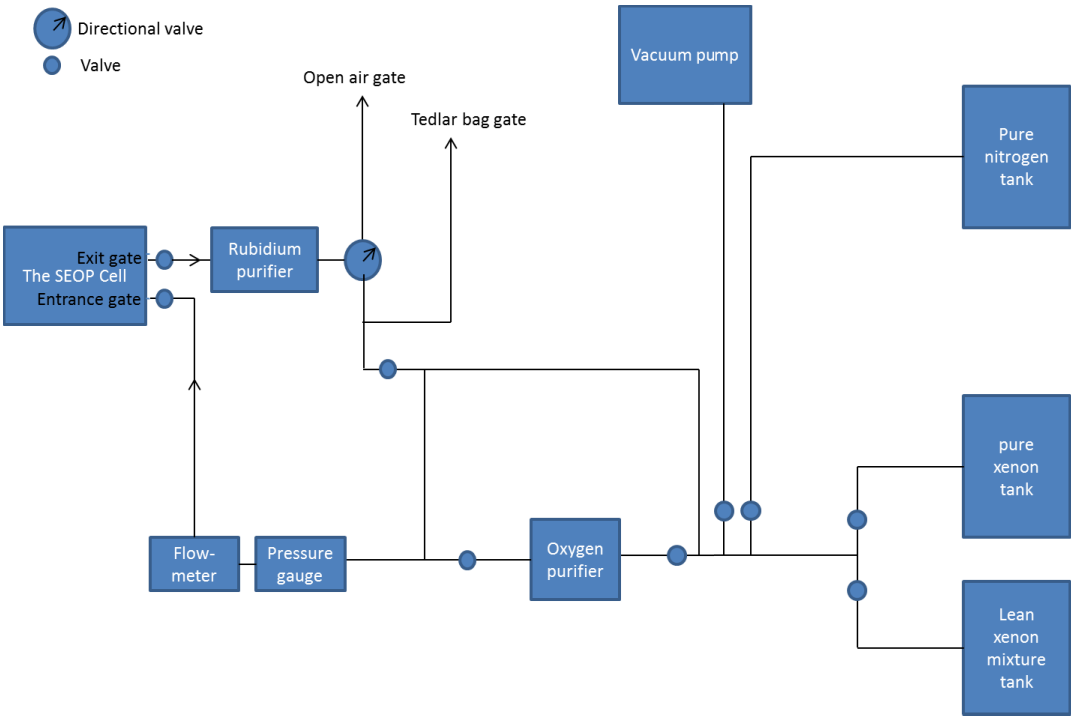

Figure 2.7. The gas circulation system.

2.2 Nuclear Magnetic Resonance (NMR) Coil and Receiver

2.2.1 Coil's Geometry

One of the roles of the NMR coil is to provide a transverse oscillating magnetic field that was described in section 1.1, which is also referred to as the r.f. pulse. It may also be referred to as the resonator, as it resonates the spins in the sample when tuned to the Larmor frequency (see section 1.1). In the case of this study, the coil is a cylindrical head coil (Clinical MR Solution). In the case of cylindrical coils, the magnetic field that is produced is perpendicular to the resonator symmetry axis due to the fact that the current is longitudinal with respect to the resonator symmetry axis, and flows in two opposite direction at each half of the resonator. The direction of the resonator symmetry axis coincides with the direction of the 3T magnetic field inside the MRI magnet bore, and hence the physical configuration inside the resonator described in section 1.1 is obtained.

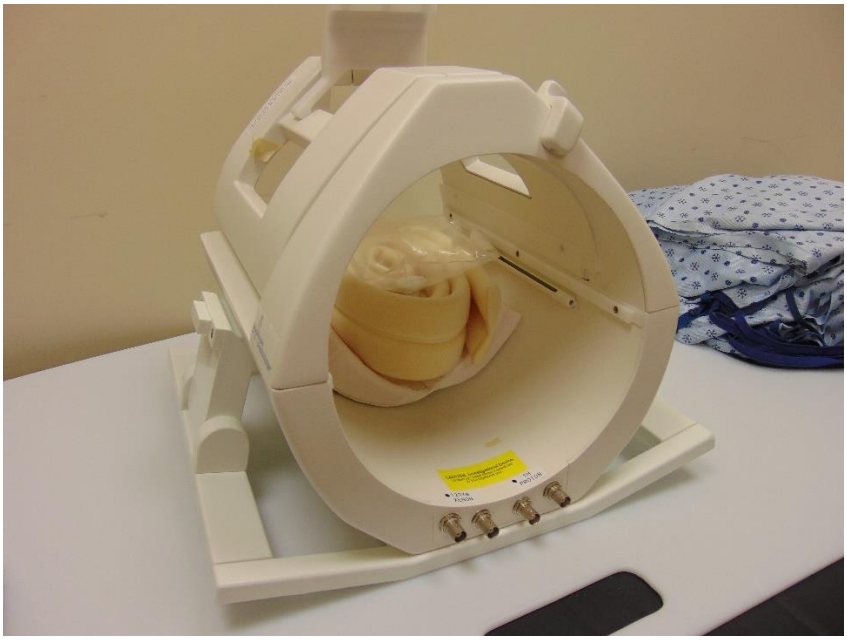

Figure 2.8. The head coil (Clinical MR Solution) that is used in this study, with a 200 ml Tedlar bag.

For the purpose of measurements, the coil was placed in the magnet bore of the Philips Achieve 3T scanner shown in figure 2.9.

Figure 2.9. The Philip Achieve 3T MRI used in xenon measurements.

2.2.2 Flip Angle Calibration

The signal obtained by an NMR examination does not contain information regarding the flip angle that was actually used to create the transverse polarization, nor can one know *a priori* the actual flip angle. Hence, the nominal signal intensity is without any reference scale. A certain flip angle can be selected but would not necessarily be the actual flip angle.

To resolve this issue, prior to each NMR examination, a series of 18 spectra of a high pressure (3.03 Atm) xenon gas phantom was taken (the xenon gas composed of 90% ^{129}Xe, compared to 26.4% in its natural abundance). The high xenon pressure and enrichment guarantee enough signal even from a sample that is thermally polarized. Each spectrum in the series was acquired with an increment of 10^0 in the flip angle with comparison to the preceding spectrum. If the flip angle was completely calibrated, one expects to see the maximal signal obtained in the ninth spectrum corresponding to a flip angle of 90^0, and no signal at all obtained in the 18^{th} spectrum. Exaggerated assessment of the flip angle is correspond to a shift in the position of the peak towards spectra with a higher nominal value of flip angle than the ninth. A lower value of the nominal flip angle in comparison to the actual flip angle is correspond to a shift towards spectra with lower nominal values of flip angle.

A way to verify the calibration of the flip angle is by using a HP gas sample. An application of 90^0 pulse demolishes the polarization completely, and hence one should expect to obtain no signal in a sequential 90^0 pulse. If any signal is obtained in the sequential r.f. application, then the flip angle is not corresponding to a 90^0 pulse. Evidently, this method does not provide information regarding whether the actual flip angle is higher or lower than the nominal value.

2.3 Measurements and Procedures

2.3.1 Rubidium Polarization Measurement

The rubidium polarization can be calculated based on the measured transmitted intensity of the pumping light by making several simplifying assumptions [39]. It is assumed that the rubidium polarization is uniform across the cell. Although in reality the rubidium polarization is not uniform, this assumption is sufficient for obtaining a rough estimate, of which most of the error comes from the transmitted radiation measurements. In addition, it is be assumed that the absorption coefficient is proportional to the spin independent cross section σ_0 and to the number of rubidium atoms with the valance electron in the down state, N_-,

$$A(B) \sim \sigma_0 N_- . \qquad (2.2)$$

As suggested in eq. 2.2, the absorption coefficient depends on the magnetic field. Another simplifying assumption which relates to that fact, is that in a case where there is no magnetic field, the rubidium is completely unpolarized. Hence, in that case, eq. 2.2 becomes,

$$A(0) \sim \sigma_0 \frac{N}{2}. \qquad (2.3)$$

Another assumption that assists to relate the absorption coefficient to the measured transmitted light intensity, is the relation,

$$2.4 \qquad \frac{d}{dx} I(x,B) = -A(B)I(x),$$

where $I(x)$ is the measured transmitted light intensity after a passage of distance x through the SEOP cell, which is the cell longitudinal length (although it will be eliminated from the calculation). Given that I_0 is the light intensity as the beam enters the cell, eq. 2.4 can be equivalently written as,

$$2.5 \qquad \frac{1}{x} lan\left(\frac{I_0}{I(x,B)}\right) = A(B),$$

and thus a relationship between the intensities and the absorption coefficient has been established.

As N_+ denotes the number of rubidium atoms with the valance electronic spin in the up state, the rubidium polarization can be written as,

$$2.6 \qquad p_{Rb} = \frac{N_+ - N_-}{N} = 1 - \frac{2N_-}{N}.$$

Using eq. 2.2, 2.3 and 2.5, eq. 2.6 can be written as,

$$2.7 \qquad p_{Rb} = 1 - \frac{A(B)}{A(0)} = 1 - \frac{lan\left(\frac{I_0}{I(x,B)}\right)}{lan\left(\frac{I_0}{I(x,0)}\right)}.$$

It is clear from eq. 2.7 that 3 measurements of the transmitted light intensity are required to determine the rubidium polarization: (1) the measurement of the light intensity under the conditions at which the rubidium is polarized ($I(x,B)$), (2) another measurement under the same conditions but without the magnetic field ($I(x,0)$), and (3) a background measurement with no rubidium present in the cell (I_0). By assuming that at low temperature no power attenuation occurs as the radiation travels through the cell, I_0 can be assumed to be the light intensity as it enters the cell, regardless of the specific conditions of a certain measurement.

2.3.2 Xenon Polarization Measurements

In essence, the signal in every MRI scan is the radiation emitted due to the coherent precession of magnetic dipoles. The time-dependent magnetic fields induced on the coil results in a time-dependent voltage that can reach hundreds of millivolts after amplification. The conversion of the signal represented as electric voltage to a signal represented as the amplitude of the magnetic field produced by the sample is impractical and unnecessary. In spectroscopy, as well as in imaging, the important quantity is the magnitude of the signal, which happens to be at the millivolts level, relative to the background signal, better known as noise. Thus, in imaging for example, the signal to noise ratio (SNR) will be the major factor in determining the quality of an image, whether it is in terms of brightness or resolution, or in determining the acquisition time. (In many cases it would be more accurate to consider the contrast to noise ratio (CNR) as the major factor for the image quality, but it is usually possible to

approach maximization of the CNR by a proper pulse sequence. Nevertheless, high SNR is a necessary condition for achieving high CNR. Moreover, CNR is irrelevant to spectroscopy experiments).

However, the SNR of a certain sample does not indicate the polarization, since a high SNR, for example, can stem from high number of spins per unit of volume. Hence, in order to measure the polarization, the number of spins has to be normalized. For doing so, each NMR scan has to be accompanied by a normalizing reference scan, which is done in two manners.

The first manner uses a xenon polarization control SNR measurement (denoted by s_{th}) of another sample, whose properties are known. Given a measurement of the HP xenon gas SNR, s_{hp}, the polarization of the HP xenon gas sample can be calculated by using the fact that the ratio of the two SNRs is equal to the ratio of the polarizations, up to factor, c, which depends on the ratio of the number of spins in each sample and on acquisition parameters, namely,

$$\frac{p_{hp}^{m}}{p_{th}} = c\frac{s_{hp}}{s_{th}}, \qquad 2.8$$

where p_{hp}^{m} is the calculated HP xenon gas polarization (the m index stands for 'measured'), and p_{th} is the theoretical value of the thermal polarized xenon gas in 3T magnetic field and room temperature, which is $p_{th}=2.84\cdot10^{-6}$ (see section 1). By expressing c explicitly, the HP xenon gas polarization can be calculated according to,

$$p_{Xe}^{m} = \frac{s_{hp}}{s_{th}}\frac{sin(\alpha_{th})}{sin(\alpha_{hp})}\frac{N_{th}}{N_{hp}}\frac{\xi_{th}}{\xi_{hp}}N^{\frac{1}{2}}p_{th}, \qquad 2.9$$

where α_{th} and α_{hp} are the flip angles used for the measurements of the thermal polarized sample and the HP gas sample respectively; N_{th} and N_{hp} are the number of xenon atoms in the thermal polarized sample and the HP gas sample, respectively; ξ_{th} and ξ_{hp} are the fraction of ^{129}Xe atoms from the total number of atoms in the thermal polarized sample and the HP gas sample, respectively; and *N* is the number of acquisition repetitions performed on the thermal polarized sample in order to obtain sufficient SNR such that the background signal will not pose a significant error (that issue usually does not exist with the HP gas sample, due to the high value of the SNR). However, in this study, in the case of a phantom thermal control sample, the SNR obtained in one acquisition is high enough, and hence *N* is set to *N=1*. A factor of the ratio of the gyromagnetic ratios, $\frac{\gamma_{th}}{\gamma_{hp}}$, (which equals to the ratio of the masses of the two type of nuclei) should appear if the control measurement were performed with other type of nuclei.

In order to extract the quantity of the number of atoms in the i gas sample, N_i, one can assume ideal gas and use the ideal gas law,

$$N_i = \frac{P_i V_i}{k_b T}, \qquad 2.10$$

where P_i and V_i are the pressure and volume of the i gas sample. Thus, eq. 2.9 becomes,

2.11 $$p_{Xe}^{m} = \frac{s_{hp}}{s_{th}} \frac{sin(\alpha_{th})}{sin(\alpha_{hp})} \frac{P_{th}V_{th}}{P_{hp}V_{hp}} \frac{\xi_{th}}{\xi_{hp}} p_{th}.$$

The volume of the phantom was measured and its pressure was given. To measure the volume of the HP gas sample the gas was sucked out of the Tedlar bag with a syringe; the reading of the syringe implied the gas volume in the Tedlar bag. The pressure in the Tedlar bag can be assumed to be 1 Atm, based on the following argument: as gas depletes the SEOP cell towards the Tedlar bag, the pressure inside the Tedlar bag is essentially zero. Since the pressure inside the SEOP cell is always kept above 1 Atm, as the Tedlar bag is exposed to the content of the cell, the pressure inside the Tedlar bag slightly exceeds 1 Atm, and thus the gas inside the Tedlar bag exerts force towards the outside, expanding and the Tedlar bag. In other words, the expansion of the Tedlar bag occurs isobarically, and thus the pressure can be assumed to be equal to the pressure outside the Tedlar bag, i.e., 1 Atm. The temperature was the room temperature in all cases, and thus is cancelled in the calculations.

In cases where the HP gas sample contained enough ^{129}Xe to produce sufficient thermal signal for the purpose of SNR normalization, the same HP gas sample was used as the control sample. That is the second method in which the xenon polarization was measured. Since in this case the HP gas sample was the same as the control sample, formally, $P_{th}=P_{hp}$, $V_{th}=V_{hp}$ and $\xi_{th} = \xi_{hp}$, which simplify the calculations. However, two additional measures had to be taken: since the signal of naturally abundant xenon gas at 1 Atm is very low, the control measurement had to be averaged over many repetitions, and N (see eq. 2.) was typically set to 100. Moreover, oxygen gas was added to the sample (see the discussion about TR in section 1.1.5). Using this method, the xenon polarization was calculated according to,

2.12 $$p_{Xe}^{m} = \frac{s_{hp}}{s_{th}} \frac{sin(\alpha_{th})}{sin(\alpha_{hp})} N^{\frac{1}{2}} p_{th}.$$

2.3.3. Echo Time (TE) and Recovery Time (TR)

The term 'echo time' may be misleading in the context of this work as there is no echo involved, but since it is used in the literature to denote more generally the time that elapses between the r.f. pulse and the readout, this notation will be adapted. The ‘echo’ refers to the ‘echo’ of spins. Spin echo is a pulse sequence designed to recover the signal that decays with the T^*_2 time constant. At a certain point in time, an inversion pulse (corresponding to a 180^0 flip angle) is applied, which eventually causes the cancelation of the effect of the T^*_2 decay on the signal. The position of the inversion pulse on the time axis is determined according to which contrast is desired. Once the inversion pulse was applied, the signal reappears after a period of time equal to the time duration between the r.f. pulse and the inversion pulse, with an intensity equal to the value that it had were it decays with time constant T_2 from the moment the r.f. pulse was applied. The time between the r.f. pulse and the inversion pulse is TE/2, and in case that there is no inversion pulse, and thus, no echo, it is simply the time between the r.f. pulse and the moment of readout. In both cases, when the pulse sequence is designed to acquire an image, the TE (along with the TR) determines the kind of contrast.

The time that elapses between two sequential r.f. pulses is known as the recovery time. The word ‘recovery’ refers to the longitudinal component of the thermal polarization. In an HP gas sample, the term 'recovery' is misleading, since in that case, the T_1 relaxation is associated with the polarization decay. Moreover, T_1 of an HP gas is much longer than a typical T_1 value of proton nuclear spin polarization, and can reach duration of hours.

Although the TR used for sequential measurements of HP gas polarization is arbitrary, it is not arbitrary in the case of a thermal polarization measurement that is used as a control measurement of the polarization of an HP gas sample. The thermal measurement of a sample that contains pure xenon gas at 1 Atm (as in this study) is impractical because of the infrequent nuclear spin interactions between the xenon atoms. Those spin interactions permit the recovery of the longitudinal thermal polarization component, and without it, the spins will maintain their transverse component. To resolve this issue, oxygen gas is added to the sample. As the total pressure increases, the spin interactions between two colliding xenon and oxygen atoms become more frequent, but more importantly, as will be stressed in section 5.4.2.3, those collisions involve a strong dipolar interaction between the nuclear spin of the xenon and the magnetic moment of the oxygen molecule, and T_1 is decreased to the order of seconds. The TR can then be made long enough to enable complete recovery of the longitudinal component of the polarization, and short enough to enable many acquisitions in reasonable amount of time.

Moreover, the reduction in T_1 by the insertion of oxygen enables to perform the control measurement few minutes after the polarization measurement was performed without risking in 'contamination' of the thermal signal by the HP signal.

2.3.4 Measurement of the Xenon-Nitrogen Mixture Composition

One of the HP gas mixture whose polarization was measured is composed of naturally abundant xenon gas and nitrogen gas. It is almost impossible to determine the ratio between the xenon pressure and the nitrogen pressure prior to the measurement. However, it is possible to assess that ratio after the gas mixture has been prepared.

For that purpose, a control measurement of thermally polarized pure xenon was performed. Assuming that the control sample has volume of V_c at 1 Atm, and produces SNR of s_c, and that the i composition of xenon gas and nitrogen gas has volume of V_i at 1 Atm and produces SNR of s_i, the ratio of the xenon pressure to the total pressure in the i mixture is given by the ratio,

$$\chi = \frac{\frac{s_i}{V_i}}{\frac{s_c}{V_c}}. \qquad 2.13$$

2.3.5 Procedures of Measurements

The first stage was to optimize the polarization of the pure xenon sample in terms of the temperature. Then the same procedure was done with the lean xenon mixture (composed out of 1% xenon, 10% nitrogen and 89% helium). The two procedures were done under total cell pressure of 3 Atm.

The second stage was to optimize the polarization of a mixture composed out of xenon and nitrogen in terms of the ratio between the two components, at a constant temperature. The partial xenon pressure was always maintained a value between the value of the pure xenon pressure (i.e., ratio of unity) and of the lean xenon mixture (i.e., the xenon partial pressure will not be reduced below 1%). According to the inverse relation that is stressed in section 1.3.1 between the optimal temperature and the partial xenon pressure, the constant temperature of this stage was the average temperature of the optimal temperatures obtained in the first stage for the pure xenon and the lean xenon mixture. This temperature choice for the second stage does not stem from profound physical principles, besides the fact that this is the first best guess of optimal temperature for any mixture composed out of those intermediate values of xenon partial pressure.

Independently of the main goal of establishing the relation between the xenon polarization and the xenon partial pressure, a polarization optimization was done also with respect to the total cell pressure, where 4 polarization measurements for both the lean xenon mixture and pure the xenon were performed at total cell pressures that range between 3 Atm to 1.5 Atm. A similar procedure was done with the lean xenon mixture.

The measurement procedures were done according to the following routines:

1. The Procedure of the Rubidium polarization measurements:

(1.a) The transmitted light intensity (see section 2.1.2) was registered with the SEOP cell containing only rubidium vapour, in temperature range of 80^0-130^0C with intervals of 10^0C, and the magnetic field off. The measured values were denoted by $I(x,0)$.

(1.b) (1.a) was repeated with the magnetic field on. The measured values were denoted by $I(x,B)$.

(1.c) Measurements at room temperature and no magnetic field were taken. This set of measurements was denoted with I_0.

2. The lean xenon mixture polarization procedure and measurements:

(2.a) The gas circulation system was vacuumed as the SEOP cell was sealed. Nitrogen gas at pressure of about 2 Atm was injected into the circulation system to clean any oxygen remnants. After about 1 minute the circulation system was vacuumed again.

(2.b) The required pressure of the lean xenon mixture was set at the gas circulation system, and both the entrance and the exit gate of the SEOP were opened. The pressure at the gas circulation system was always set above 1 Atm, and thus the gas flows constantly from the gas tank to the open air.

(2.c) After about two minutes of gas flow, the lean xenon mixture was assumed to be the only content inside the SEOP cell. Then the SEOP cell was sealed again with the required content and pressure for the polarization process.

(2.d) After the temperature was set to the desired value, the laser and the magnetic field were turned on and the polarization process began.

(2.e) In parallel to the polarization process, a 150 ml Tedlar bag was connected to the Tedlar bag gate. The Tedlar bag, also connected to the vacuum pump and the nitrogen tank, was vacuumed, filled with nitrogen for cleaning any oxygen remnants, and then vacuumed again. This procedure was performed twice, to insure no oxygen remnants inside the Tedlar bag.

(2.f) At the end of the polarization process, both the SEOP cell exit gate and the Tedlar bag gate were opened, and the HP gas filled the Tedlar bag due to the pressure difference.

(2.g) The Tedlar bag was transported to the MRI magnet bore. That had to be done quickly to avoid a signal decay. On the other hand, to make all the measurements compatible with one another, a time duration of 45 sec was allocated for each Tedlar bag transfer. Forty five seconds is a short duration in comparison with the T_1 constant decay (which is of order of magnitude of an hour), but it is long enough to perform the transfer for each one of the measurements.

(2.h) An NMR scan was performed. The scan parameters were: 5 repetition[3]; FA=6^0; TR=5000 ms; TE=0.11 ms (shortest); BW=2000 Hz. No averages. Prior to the scan, scans with the xenon phantom were performed to determine the off-set frequency and to perform the FA calibration (see section 2.2.2).

(2.i) A control NMR scan was performed. The control sample was a spherical glass xenon container, containing 90% ^{129}Xe enriched xenon at 3.03 Atm. The scan parameters were: no repetition; FA=90^0; TR=12,000 msec; TE=0.25 ms (shortest); BW=2000Hz. No averages. Prior to the scan, scans with the xenon phantom were performed to determine the off-set frequency and to perform the FA calibration.

(2.j) The raw data of the scan were processed by MATLAB to create the time domain signal diagrams, and the spectrum corresponds to each of these diagrams. Moreover, numerical values of the peak and the background signal standard deviation were extracted, in order to calculate the SNR, which is defined here as the quotient of these two values.

3. The pure xenon polarization procedure and measurement:

(3.a) (2.a) was repeated.

(3.b) (2.b) was repeated, only with the pure xenon tank.

(3.c) (2.c)-(2.h) were repeated.

[3] The term repetition should not be confused with the term average: while averages will form eventually one spectrum data, two repetitions will correspond to two different spectra data.

(3.d) A control NMR scan was performed. 100 ml oxygen (at 1 Atm) was added to the HP gas sample that serves as the control sample. The scan parameters were: no repetition; FA=90^0; TR=12,000 ms; TE=0.25 ms (shortest); BW=2000 Hz. 100 averages.

(3.e) (2.j) was repeated.

4. The xenon and nitrogen mixture polarization procedure and measurements

In this part of the experiment there was the challenge of preparing the gas mixture according to the nominal values of xenon pressure to total cell pressure ratio. The composition of the gas mixture could be done only in such a way that actual values of the ratio may be very different from the nominal values. However, by using the method described in section 2.3.3, a good assessment of this ratio was obtained. Below is the method to approach the nominal value of the ratio described, although quantitatively it has very little significance.

(4.a) (2.a) was repeated.

(4.b) The required pressure of the mixture component whose nominal pressure value is higher was inserted into the cell, similar to the way described in (2.b).

(4.c) The gas component with the lower nominal pressure value was inserted into the gas circulation system and blocked by the valve of the entrance gate at a pressure that was equal to the nominal total pressure in the SEOP cell.

(4.d) The valve of the entrance gate was opened. The gas in the circulation system, which was at higher pressure, flowed into the cell until the pressure was equalized with the nominal value of the total pressure.[4] Under the assumption that there is only flow into the cell, the total pressure inside the cell was composed out of the nominal value of the two gas components. The valve at the entrance gate was resealed at the moment the flow-meter reads zero, as equilibrium had been achieved.

(4.e) Steps (2.d)-(2.h) were repeated.

(4.f) Step (3.d) was repeated.

(4.g) The volume of gas inside the Tedlar bag was measured (see section 2.3.3).

(4.h) Step (2.j) was repeated.

[4] Note another assumption that been made: the gas tank continues to provide the same pressure into the gas circulation system.

3. Results

3.1 Rubidium Polarization Measurements

The following laser parameters were measured:

Laser beam power as entering the cell: 13.7 ± 0.5 W

Wavelength: 794.90 ± 0.01 nm

Bandwidth: 0.2 ± 0.05 nm

The results of the measurements of the transmitted radiation are given in figure 3.1 for measurements with and without a magnetic field. The theoretical curve of the rubidium density in the cell with respect to the temperature is also given, and it was normalized to match the scale of the ratio between the transmitted radiation for variable temperature and the transmitted radiation at room temperature.

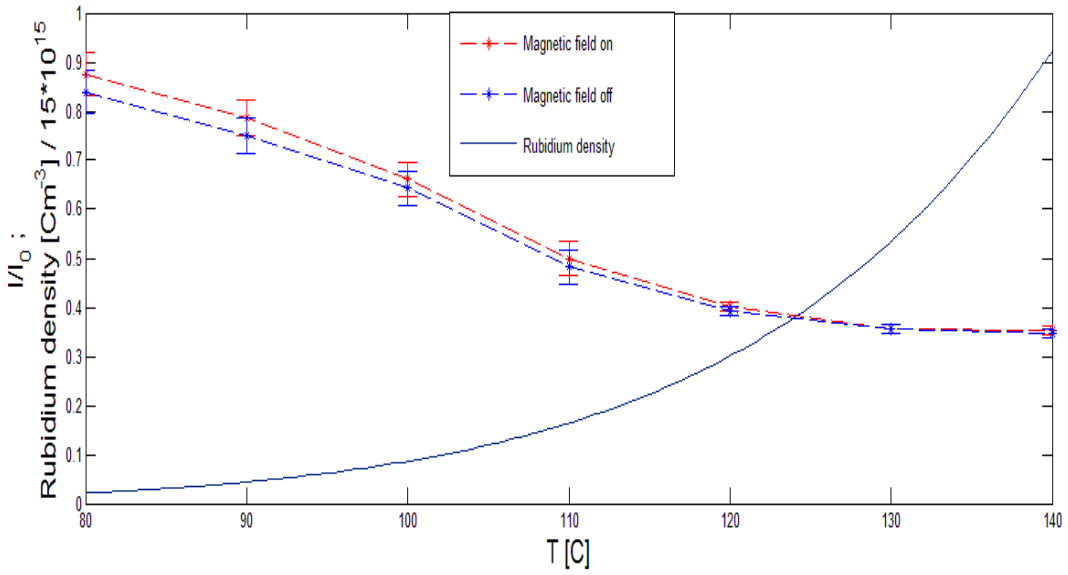

Figure 3.1. Transmitted radiation and the theoretical rubidium density as a function of the temperature.

The polarization as a function of the temperature was calculated according to eq. 2.7, and the results are given in figure 3.2 (again, the green curve is the theoretical rubidium density).

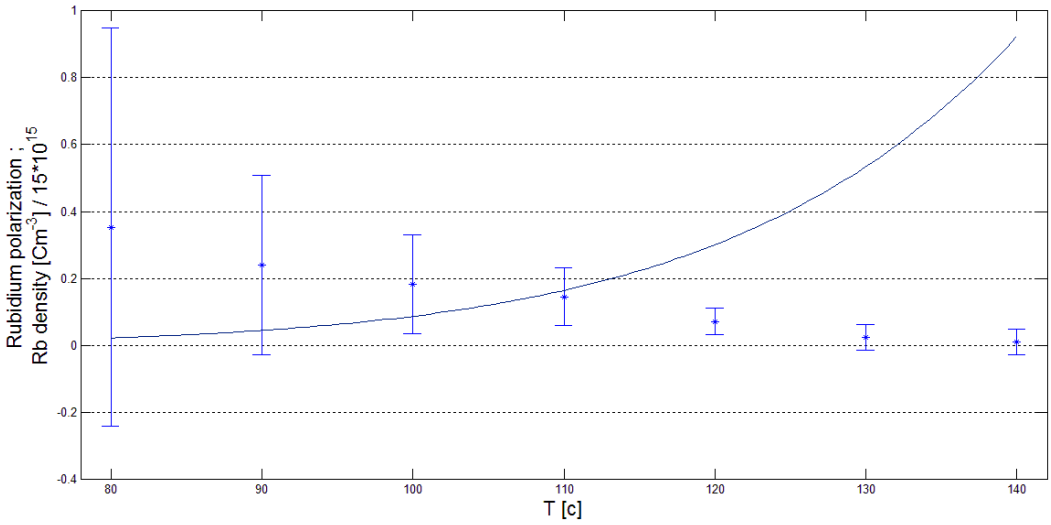

Figure 3.2. Rubidium polarization and the theoretical rubidium density as a function of the temperature.

3.2 Xenon Nuclear Polarization Measurements

The results in this section are presented as the processed data acquired from the MRI scanner. The raw data that was registered by the scanner encodes the signal produced by the transverse magnetization. The sampling time was 0.5 ms (thus the bandwidth is 2 KHz). The signal decay that is shown in the time domain should correspond to the T_2^* decay discussed in section 1.1.4.

The error bars presented in the figures are attenuated by a factor of $n^{\frac{1}{2}}$ in comparison to the cited numerical values of polarizations, where n is the number of repetitions of the measurement.

3.2.1 Flip Angle Calibration

The calibration of the flip angle was performed according to section 2.2.2. Eighteen spectra are presented in figure 3.3 after a calibration. The spectra are numerated such that the sequential number of each spectrum corresponds to 10^0 increasement of nominal flip angle. Thus, spectrum number 7, for example, was acquired with application of 70^0 flip angle.

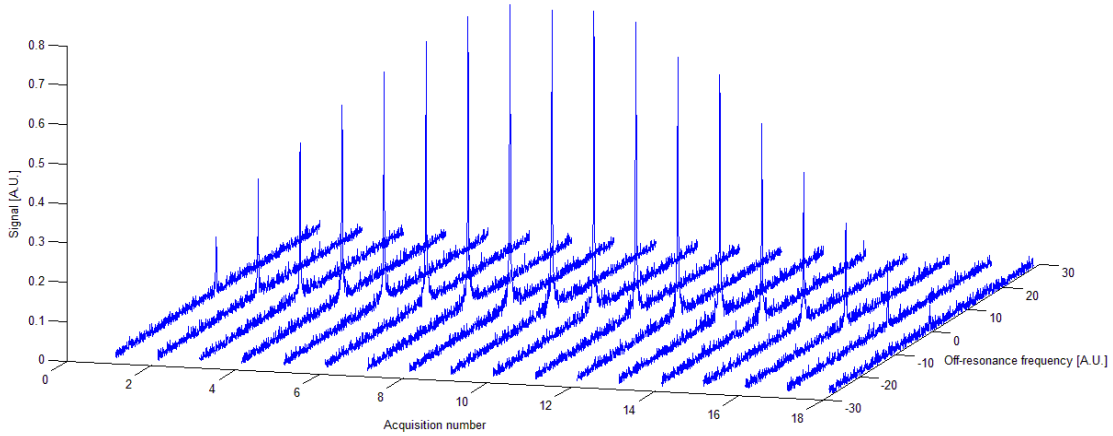

Figure 3.3. Flip angle calibration spectra. The x axis corresponds to different nominal flip angle application. The y axis is the off-resonance frequency given in an arbitrary unit, and the z axis is signal.

3.2.2 Pure Xenon

Figure 3.4 presents the time domain signal of the HP gas of the sample that was acquired with the optimal temperature for the series of the pure xenon samples.

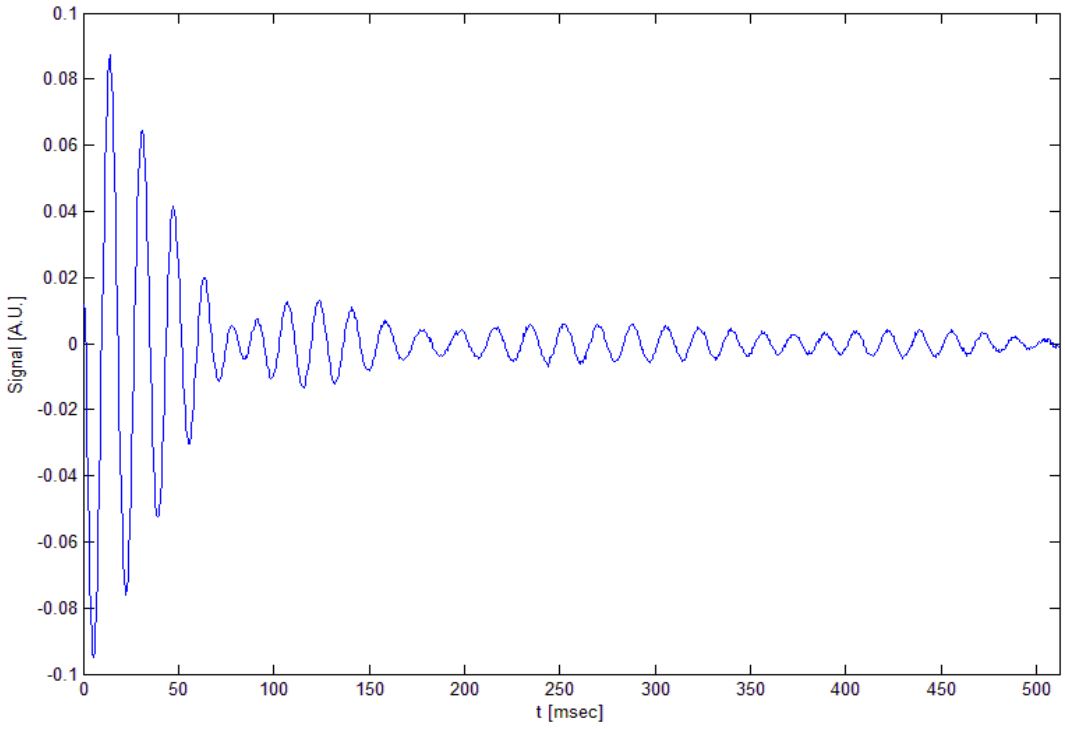

Figure 3.4. Signal as a function of time for the optimized pure xenon sample. TE=0.11 ms. FA=6^0.

The Fourier transform (F.T.) of the data presented in figure 3.4, is shown in figure 3.5.

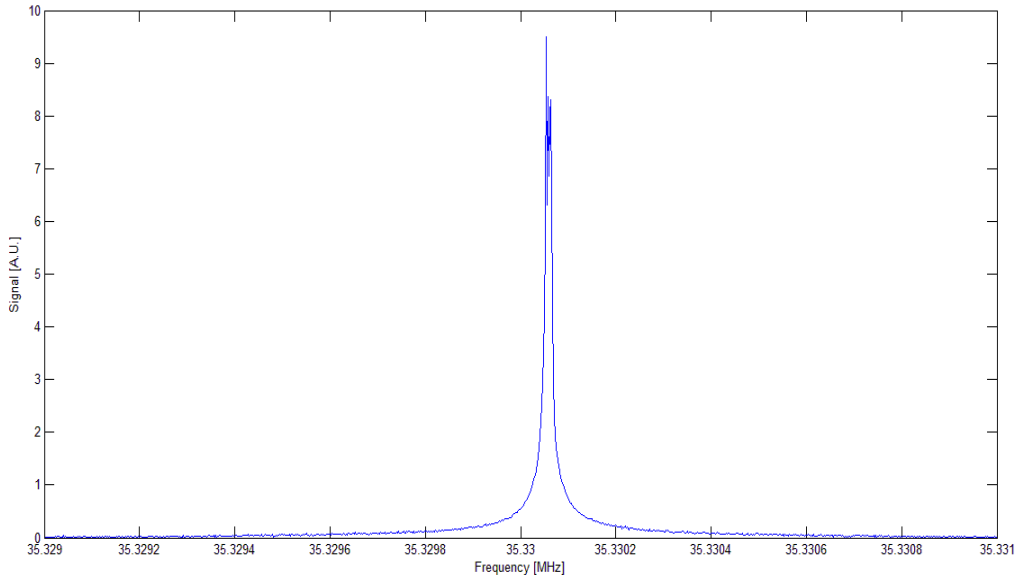

Figure 3.5. NMR spectrum for the optimized pure xenon sample.

The thermal signal of the same measurements is presented at the time domain in figure 3.6.

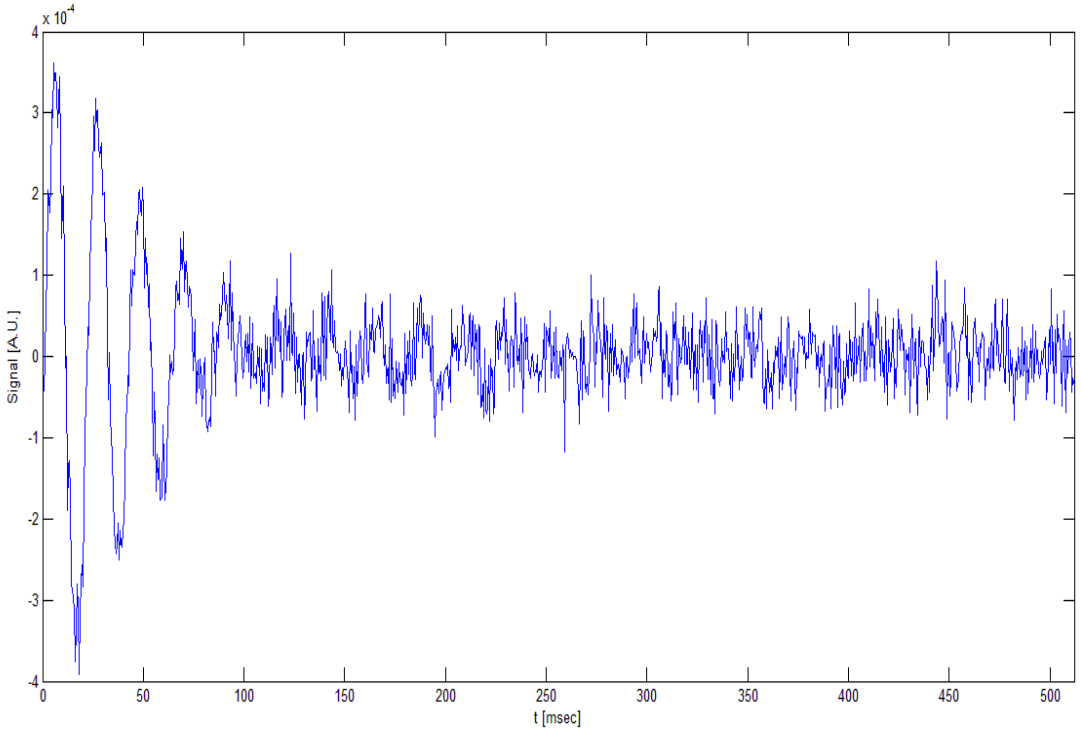

Figure 3.6. Signal as a function of time for the optimized thermally polarized pure xenon sample. TE=0.25 ms. FA=90^0.

The F.T. of the data presented in figure 3.6, is shown in figure 3.7.

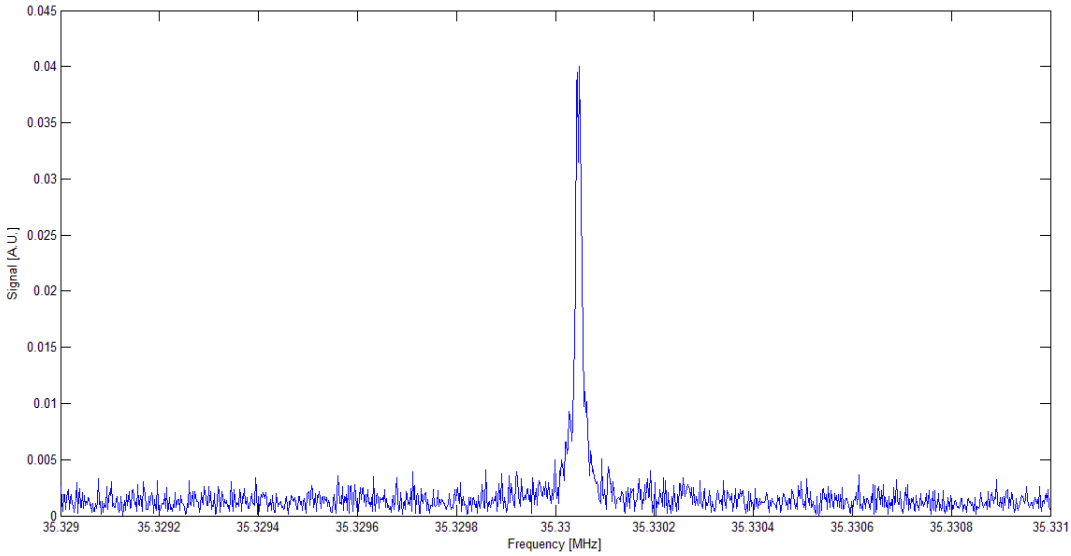

Fig 3.7. NMR spectrum for the optimized thermally polarized pure xenon sample.

Using eq. 2.12, the polarization of the presented sample was calculated, and its value is

3.1 $$p_{Xe,pure}^{Measured} = 0.00096 \pm 0.00030.$$

With respect to the temperature, the calculated polarizations of the pure HP xenon are presented in figure 3.8. The maximal polarization was achieved at 90^0C. However, the actual estimated optimal temperature was assessed as 100 ^{0}C.

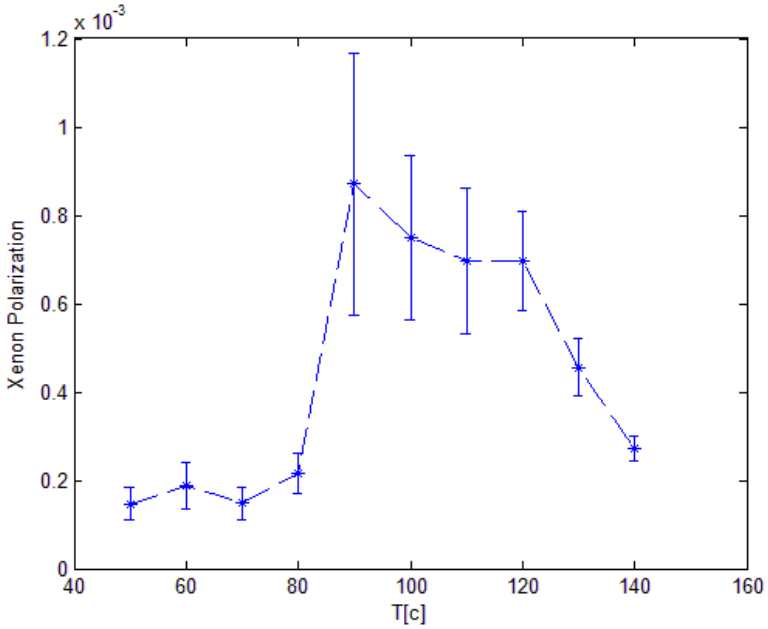

Figure 3.8. Xenon polarization as a function of the temperature for the pure xenon series of measurements. n=2.

3.2.3 Lean Xenon Mixture

Figure 3.9 presents the time domain signal of the HP gas sample that contains lean xenon mixture (1% xenon, 10% nitrogen and 89% helium). It was acquired with the sample produced using the optimal temperature.

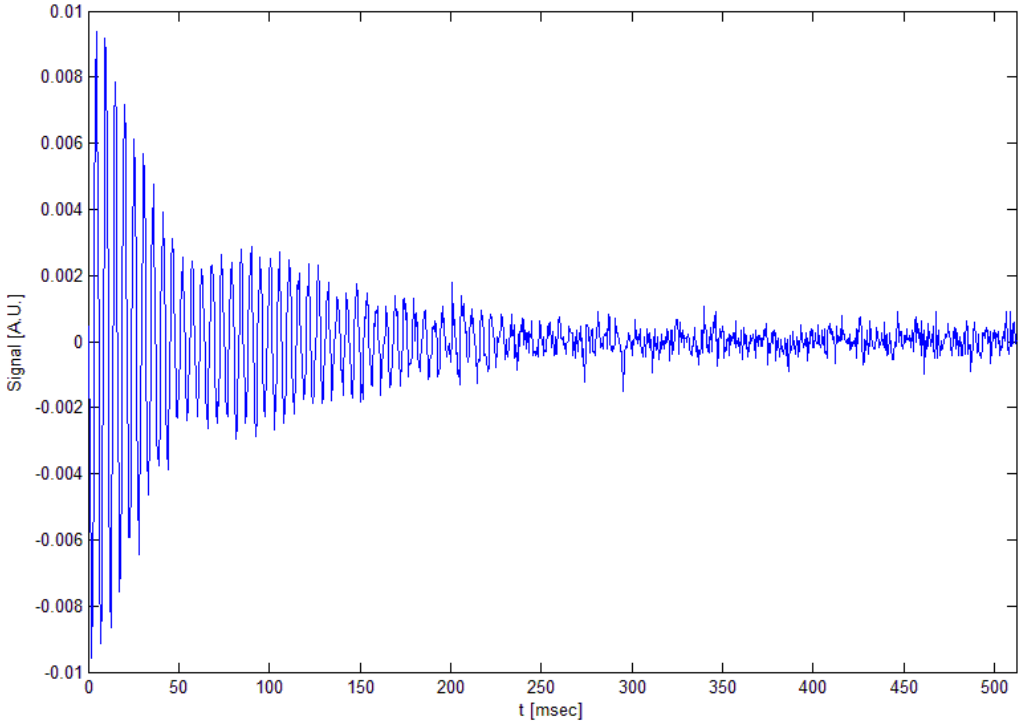

Figure 3.9. Signal as a function of time for the optimized lean xenon mixture sample. TE=0.11 ms. FA=6^0**.**

The F.T. of the data presented in figure 3.9, is shown in figure 3.10.

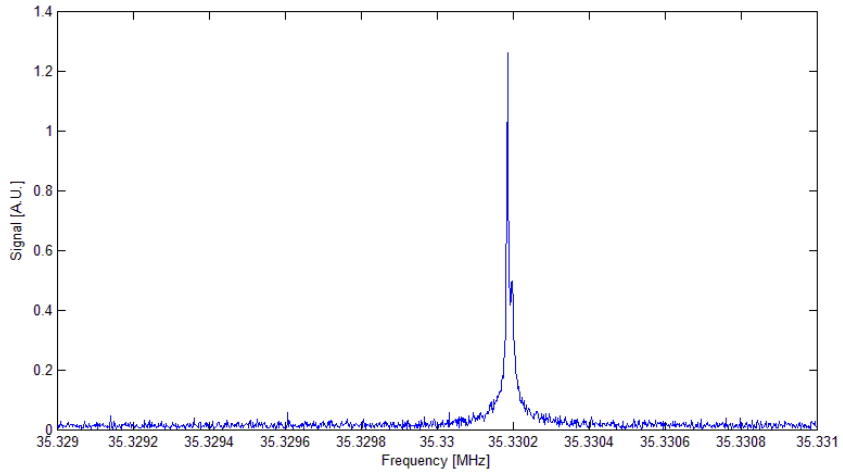

Fig 3.10. NMR spectrum for the optimized pure xenon sample.

Hence, the polarization for the set of measurements of the lean xenon mixture was calculated according to eq. 2.11. The phantom sample is assumed to be a spherical shape with a radius of 2.8 ± 0.2 Cm, containing 90% of ^{129}Xe at pressure of 3.03 atmospheres. The polarization at the optimal temperature was calculated and assessed to be,

$$p_{Xe,lean}^{Measured} = 0.052 \pm 0.029. \qquad 3.2$$

The other data points of the polarization with respect to temperature for the lean xenon mixture were calculated in the same manner, and are presented in figure 3.11. The actual optimal temperature is estimated as 135^{0}C (Although the measured optimal temperature is 140^{0}C).

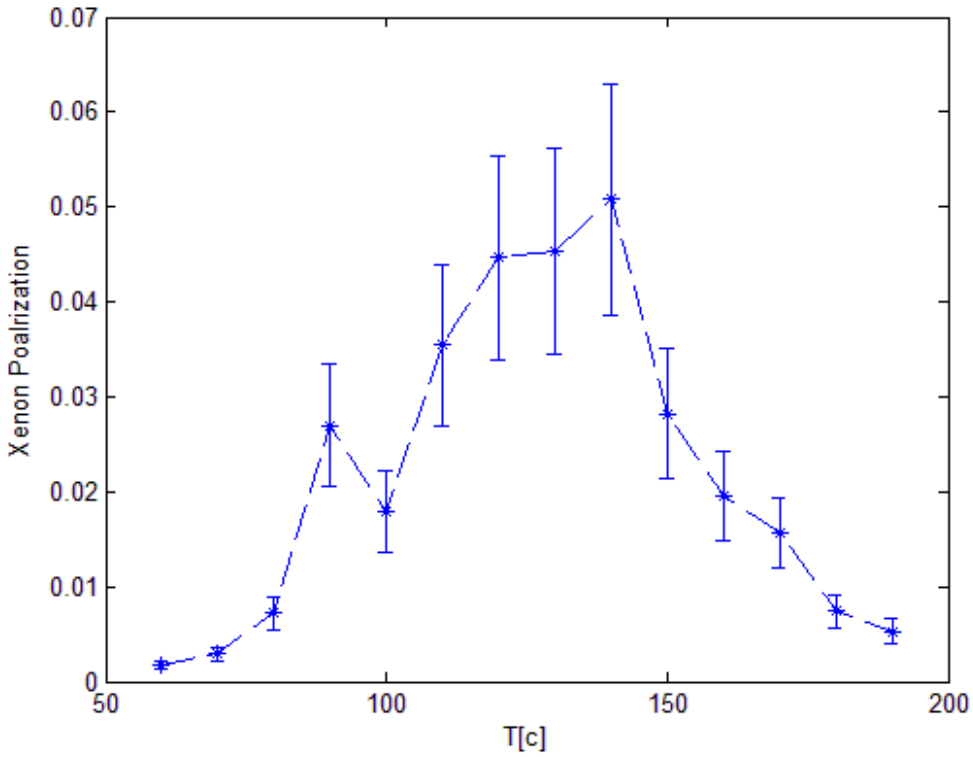

Figure 3.11. Xenon polarization as a function of the temperature for the series of the lean xenon mixture. n=3.

3.2.4 Xenon and Nitrogen Mixture

The spectrum of each measurement in the series of variable partial pressure ratio is presented in figure 3.12. The temperature was set according to the principle that was stressed in section 2.3.4, namely, 120 ^{0}C. Note that the signal is normalized by the volume of the sample at 1 Atm pressure.

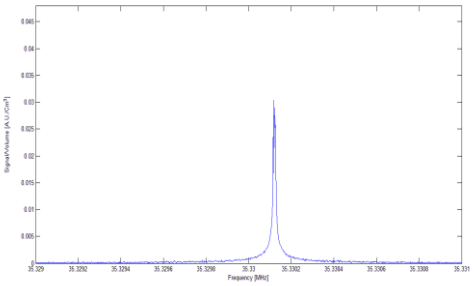

(a) P_{Xe}/P_{Total} = 0.1836±0.0106

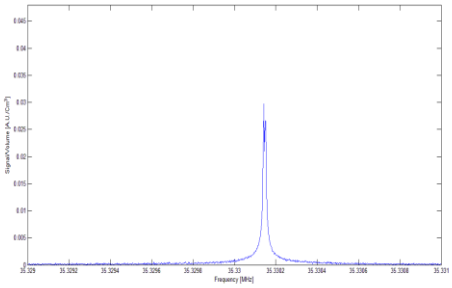

(b) P_{Xe}/P_{Total} = 0.3374±0.0142

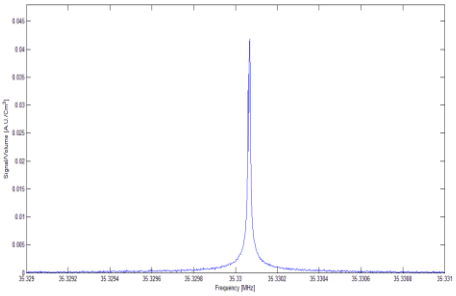

(c) P_{Xe}/P_{Total} = 0.3896±0.0139

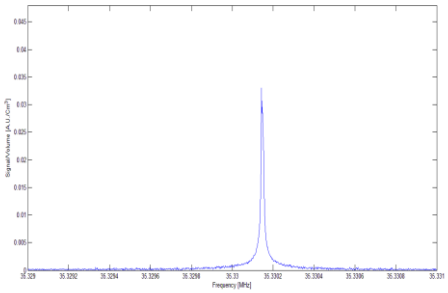

(d) P_{Xe}/P_{Total} = 0.4640±0.0174

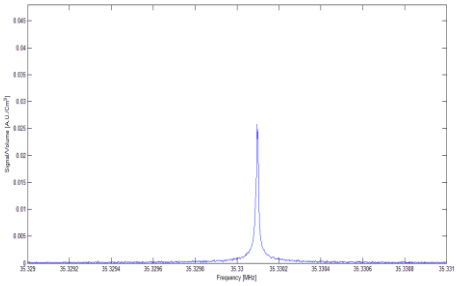

(e) P_{Xe}/P_{Total} = 0.4715±0.0156

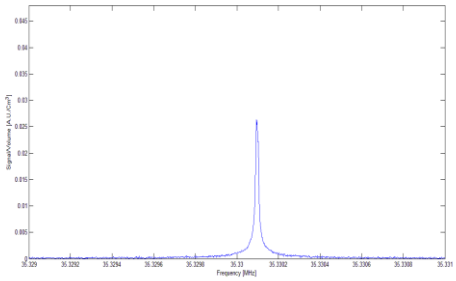

(f) P_{Xe}/P_{Total} = 0.5658±0.0188

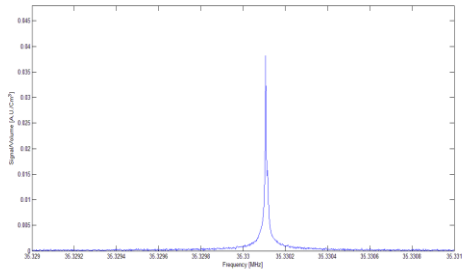

(g) P_{Xe}/P_{Total} = 0.8213±0.0216

Figure 3.12. NMR spectra of the HP gas series with variable xenon pressure to total pressure ratio. TE=0.11. FA=6^0.

The thermal signal of each of the HP gas measurements is presented in figure 3.13 in the same order of xenon pressure to total pressure ratio as in figure 3.12.

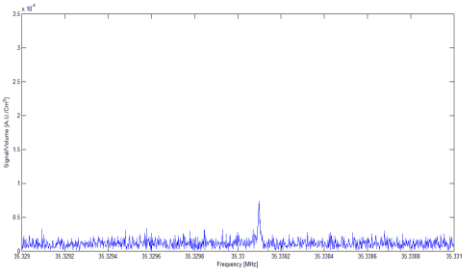

(a) P_{Xe}/P_{Total} = 0.1836±0.0106

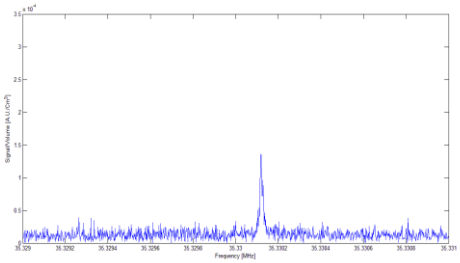

(b) P_{Xe}/P_{Total} = 0.3374±0.0142

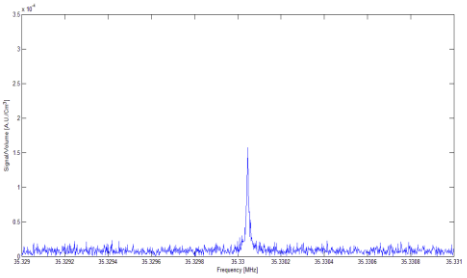

(c) P_{Xe}/P_{Total} = 0.3896±0.0139

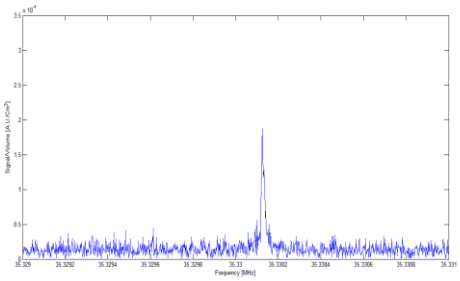

(d) P_{Xe}/P_{Total} = 0.4640±0.0174

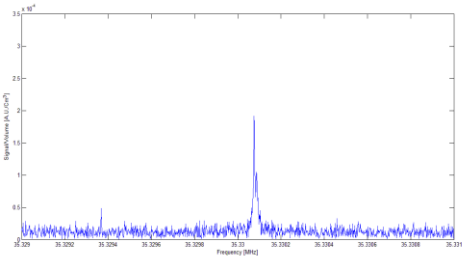

(e) P_{Xe}/P_{Total} = 0.4715±0.0156

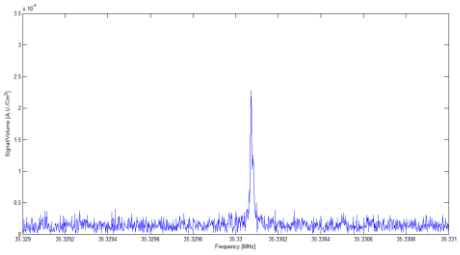

(f) P_{Xe}/P_{Total} = 0.5658±0.0188

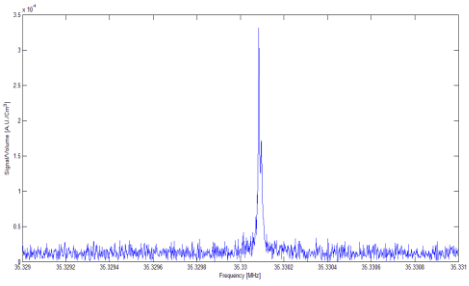

(g) P_{Xe}/P_{Total} = 0.8213±0.0216

Figure 3.13. NMR spectra of the thermal signal of the series with variable xenon pressure to total pressure ratio. TE=0.25. FA=90^0.

The polarization as a function of the xenon partial pressure to the total cell pressure ratio is given in figure 3.14.

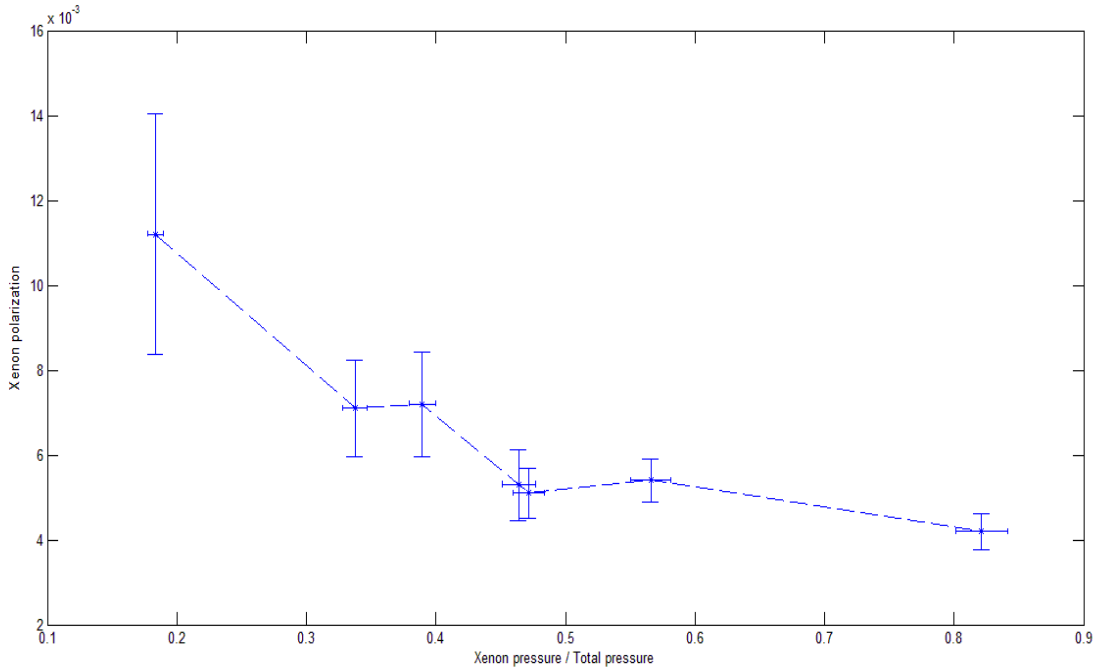

Figure 3.14. The polarization as a function of the xenon pressure to total pressure ratio. T=120 ^{0}C.

3.2.5 Total Cell Pressure

The xenon polarization as a function of the total cell pressure for pure xenon in its optimal polarization temperature (100 ^{0}C) is given in figure 3.15.

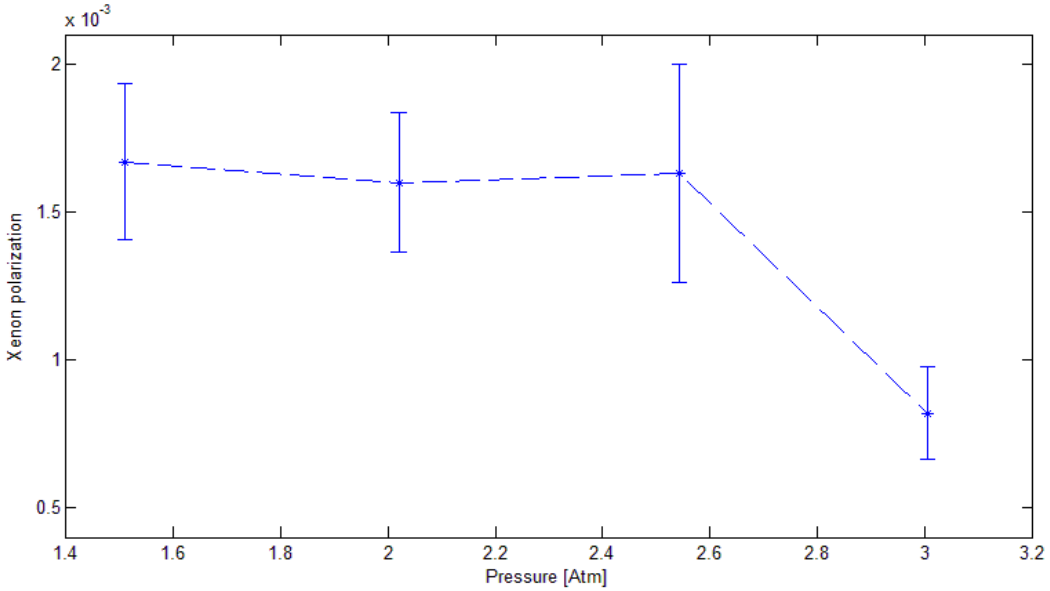

Figure 3.15. Polarization as a function of the total pressure for pure xenon. T=100 ^{0}C.

The xenon polarization as a function of the total cell pressure for lean xenon mixture in its optimal polarization temperature (135 ^{0}C) is given in figure 3.16.

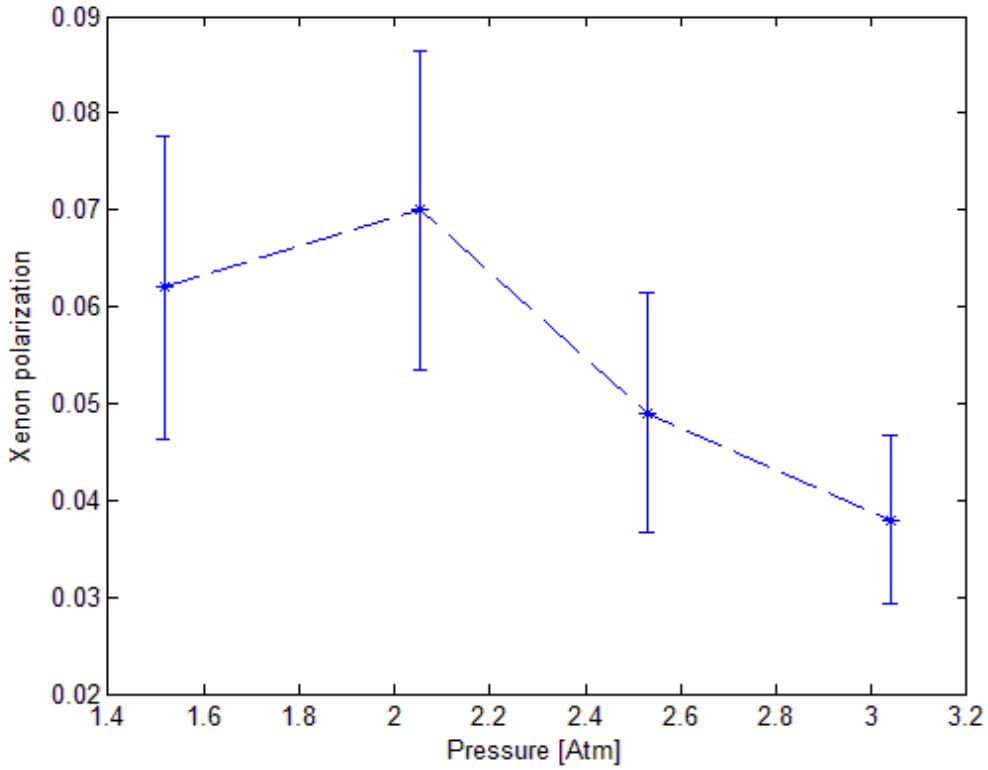

Figure 3.16. Polarization as a function of the total pressure for the xenon lean mixture. T=135 ^{0}C.

4. Discussion and Conclusions

4.1 Error Estimations

4.1.1 Rubidium Polarization

The rubidium polarization calculation was based upon the radiation measurement which involves significant error. Even at a steady state with respect to the radiation incoming flux and the SEOP cell optical properties, there were significant fluctuations in the radiation flux date that cannot be explained theoretically, and therefore were regarded as a measurement error. Two types of fluctuations were observed: fast fluctuations (on a scale of less than 1 s), and slow fluctuations (on a scale of more than 10 s). The error was determined to the larger error.

In order to estimate the error of the slow fluctuation, a series of radiation flux measurements was performed over a substantial amount of time (much longer than the typical change associated with the slow fluctuations). The result of those measurements is presented in figure 4.1.

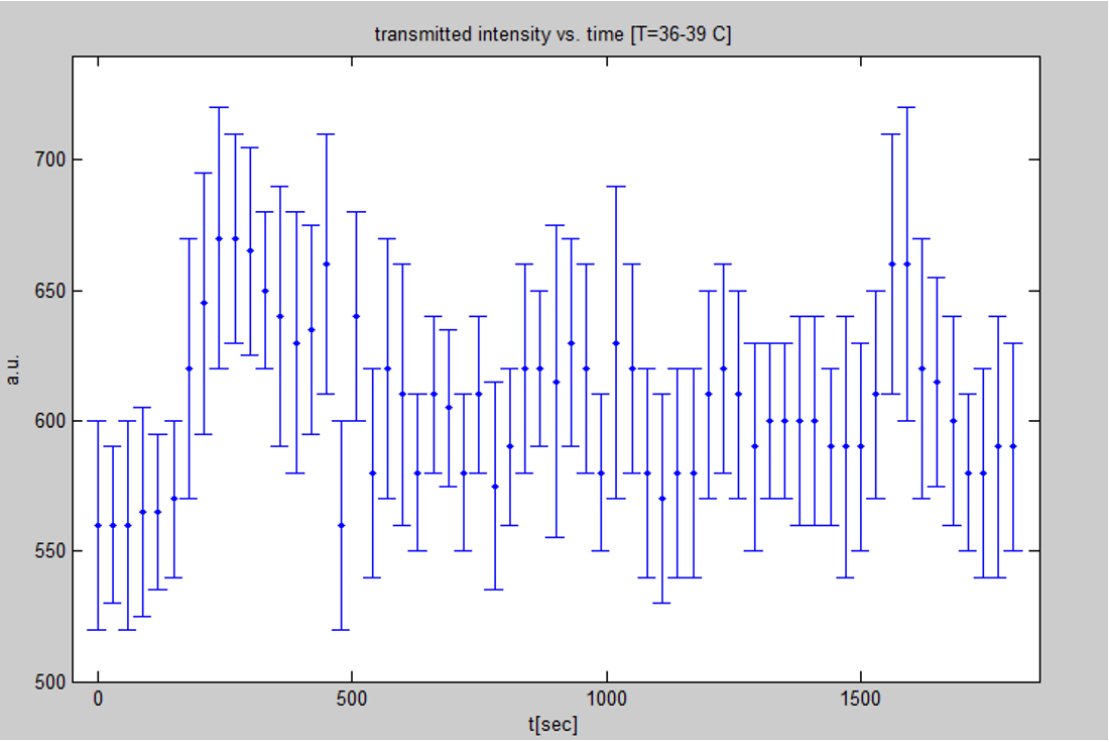

Figure 4.1. The transmitted intensity presented in arbitrary units over a long period of time. The time interval between two measurements is 30 s. The fluctuations seem caustic, and are regarded as a measurement error. The error bar accounts for the fast fluctuation that did not enable precise determination of the counts.

No particular pattern could be detected based on the results present in figure 4.1. The error was evaluated as ± 100 counts. However, as the transmitted intensity decreased with the temperature increase, the fluctuation decreased respectively.

4.1.2 Xenon Polarization

Two measurement methods were used to obtain the xenon polarization, one used a xenon phantom as a control measurement, and the other used the thermal signal from each HP gas sample as a control measurement (see section 2.3.2). The first method introduced larger error as there are four more parameters with errors (namely, the pressure and the volume of the sample and the xenon phantom). To reduce the relative error in the method that uses the xenon phantom, three repetitions were made for the lean xenon mixture polarization measurements, instead of two in the case of the pure xenon polarization measurements. That might have had the effect of compensating the allegedly larger error in the lean xenon polarization measurements. The main source of the error that was calculated is in the flip angle determination: as can be seen from figure 3.3, the relative error in the flip angle is about 0.1. Although figure 3.3 presents spectra after the flip angle has been calibrated, the largest signal was not obtained at the nominal value of 90^0. Yet, due to the relatively large variance in the signal's value, the value of the flip angle at the largest signal can be approximately extrapolated and determined at the nominal value of 90^0. The various factors contributing to the calculated error are systematic and affect each measurement equally, therefore, they could not obscure trends.

However, as it can be seen from figures 3.8, 3.11 and 3.14, there is another type of uncertainty factor that manifests itself in that the data points do not obey any particular curve, even within the frame of the error bars. Hence, there is another source of errors that is inherent to the statistical nature of the polarization. That applies to the SEOP process itself, to the delivery of the sample from the polarizer to the MRI and to the shimming of the magnetic field. Those stages introduce large variance in the measurements in a manner that is beyond of the scope of this study, except for a comment regarding the spin depolarization due to gradients (see section 5.4.2.2): the areas surrounding the Helmholz coils through which the HP gas flowed as it was depleted from the cell, and much more so, as it is brought in to the magnetic MRI bore, are characterized by having magnetic field gradients. The relaxation, however, is stimulated by gradients along the transverse plane, and thus their effect is dependent on the path that the sample takes as it is transferred from the SEOP cell into the MRI magnet bore. The conjecture of the negative influence of gradients at the edge of the magnet bore was tested, by acquiring few spectra after the HP gas sample was put in an area of large gradient for a few minutes. However, no destructive influence on the HP gas polarization was recorded.

Regarding the shimming, it is evident from the results (see figure 3.4 and 3.5 for example) that poor shimming affected the measurements. Due to the deviation from the nominal value of the magnetic field, the signal is distributed over several Larmor frequencies. The signal is measured as the maximal value of the largest Lorentzian, and thus by ignoring the other Lorentzians, the magnitude of the signal might be underestimated. However, in a certain set of measurements the SNR was calculated by integrating all the Lorentzians within the vicinity of the major Larmor frequency. Since the deviation from the value of the polarization as it was evaluated by the maximal value of the largest Lorentzian was negligible in comparison with its value when using integrated SNRs (probably due to the normalization of the SNR with the control measurement), the polarization was calculated based on the maximal value.

4.2 Results

4.2.1 Rubidium Polarization

The results of the rubidium polarization measurements with variable temperature shown in figure 3.2 may suggest the existence of an inverse relation between the rubidium polarization and the temperature. This trend is in accordance to the data presented in [64], although for the non-zero magnetic field, the transmitted radiation intensity did not persist at the same level as in [64] and as expected from the theoretical model (see section 2.3.1). The trend might be explained by the fact that there was light absorption by unpolarized rubidium that remained in the cell, although the magnetic field was on. In contrary to the experiment described in [64], the radiation power was very low (about 14 W in comparison to 200 W in [64]), and thus mainly the area in the cell near the light entrance contained significant polarized rubidium, where the incoming light could be transmitted. Sufficient light flux (evidently, 14 W is not sufficient) pushes the limits of the illuminated area until they reach the back of the cell, such that a path of polarized rubidium is be formed where light can travel without being absorbed (see figure 4.2). A more formal way of describing the discrepancy is by the fact that the assumption of uniform rubidium polarization across the cell from which the expression for calculating the polarization was derived, does not hold. The illumination model is presented in [74].

To conclude, although the rubidium polarization presented the expected trend, the polarization value should be considered with much suspicions. Regardless of the results, the decrease in the rubidium polarization with temperature is expected due to the larger radiation flux required to polarize an exponentially increasing number of rubidium atoms. As the radiation flux is approximately constant in temperature, the rubidium polarization is expected to drop.

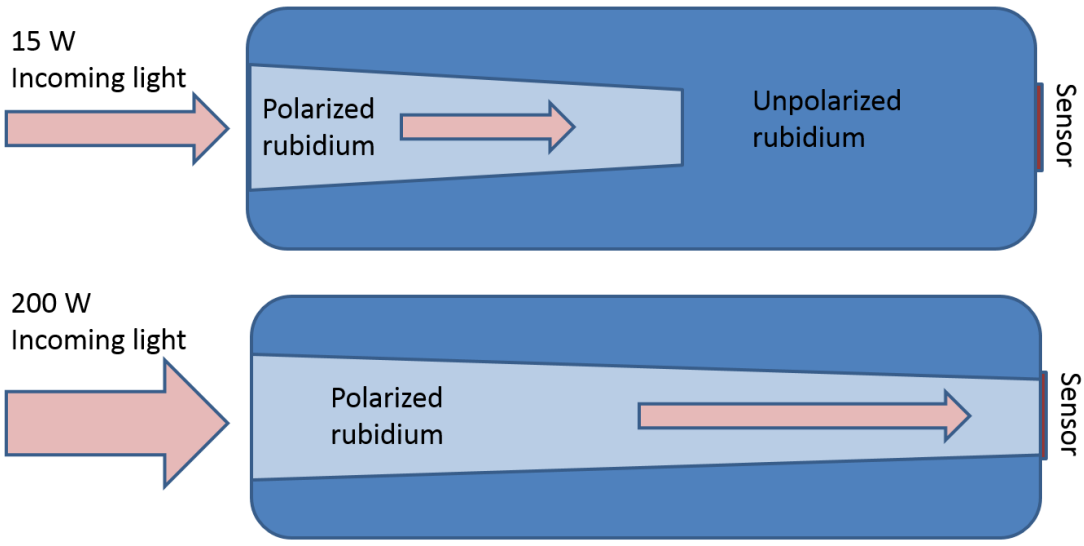

Figure 4.2. The light penetration through the cell depends strongly on the power of the incoming light. Insufficient power may not polarize rubidium gas that is not in the vicinity of the optic entrence, and thus an optical path to the sensor will not be formed.

4.2.2 Xenon Polarization

Two major aspects regarding the xenon polarization results will be addressed: (1) the polarization levels and (2) the observed trends of the polarization with respect to pressure and temperature.

(1) Polarization levels were significantly low in comparison to other studies that measured the xenon polarization in similar conditions. The maximal polarization for the set of measurements with variable Xe/N_2 value, was obtained for the minimal xenon-to-total-cell ratio (about 0.18, and total cell pressure of about 2280 Torr), with ~0.012 polarization, in comparison to polarization of 0.22 in [63] and of 0.90 in [64]. However, while in this study the measured light power was about 14 W, it was 29 W and 200 W in [63] and [64], respectively. The significance of having intense light beam in SEOP experiments is evident from the discussion about the rubidium polarization in 4.2.1. High rubidium polarization is a necessary condition (but not sufficient) for obtaining high xenon polarization, which is limited by the level of the rubidium polarization. Moreover, the polarization measurements in [63] and [64] were performed inside the cell, and did not necessitate a delivery to the magnet bore.

(2) The general trends of the xenon polarization with respect to temperature and pressure were in accordance to the findings in [63-65], although with weak statistical significance. The explanation for the tendency of the xenon polarization to increase in lower temperatures mainly stems from a rubidium density that was too low. In higher temperatures, the xenon polarization decreased since the rubidium polarization also decreased. Moreover, the increase in the rubidium density created “dark areas” in the cell (see section 4.2.1), where the formation of short-lived RbXe molecules increased the xenon spin relaxation rate due to both spin exchange and spin-rotation interaction. The obtained value of the optimal temperature was as expected according to the finding of [63], namely, a higher optimal temperature for a lower partial xenon pressure (in [63] an inverse relation was found between the optimal temperature and partial xenon pressure). This pressure-temperature interdependence is not fully understood, but it probably stems from cell illumination considerations which were discussed in section 4.2.1.

The expected trends were also found in the set of measurements with variable value of xenon-to-total pressure ratio. For higher ratio of xenon-to-total pressure, the spin transfer from the rubidium to the xenon becomes less efficient, and for lower partial xenon pressure a higher polarization is obtained. Moreover, the spin relaxation rate due to the creation of Xe-Xe dimers is linear in the xenon pressure (see section 5.4.1.2), and thus it increased at higher xenon pressures and deteriorated the polarization.

The fundamental question regarding the HP gas production is what would be the optimal gas mixture and temperature combination that results in the best gas sample for the application of MRI. It had been shown that in terms of the temperature, the answer depends on the xenon partial pressure. Nevertheless, given a certain temperature and different combination of xenon and nitrogen, although the lower values of xenon pressure resulted in higher polarization, they also resulted in a smaller

number of aligned spins per unit volume[5]. Considering, for example, the two measurements with the lowest xenon-to-total pressures ratio, the ratio of the number of xenon atoms between the lowest partial pressure measurement and the second lowest partial pressure measurement was 0.54. On the other hand, the polarization ratio between them was only 1.57. Thus the ratio of the number of the aligned spin is 0.85.

Similar comparison between the xenon-nitrogen combination that gives rise to the largest number of aligned xenon atoms per unit volume and the lean xenon mixture at an optimal temperature results in favor of the xenon-nitrogen mixture; the ratio between the number of aligned xenon atoms per unit volume of the lean mixture sample and the xenon-nitrogen combination was only 0.14. In other words, using a xenon lean mixture (containing only 1% xenon) and obtaining almost 12 fold larger polarization, still forming only 0.14 aligned spins per unit volume of those that are be obtained with a xenon-nitrogen mixture with 0.82 ratio of xenon-to-total-cell pressures. One might expect that according to this trend, a pure xenon sample will contain the highest number of aligned spins per volume. However, this is not the case. The presence of nitrogen makes the spin exchange efficient, as it contributes to the formation of VDW RbXe molecules without increasing the xenon polarization relaxation. The fact that this property persists for relatively small values of nitrogen partial pressure is in accordance with the discussion in section 5.3.5 and 5.4.1.2.

Last words and future work

Although the polarization levels that were obtained in this study are insufficient for most of the purposes of HP gas MRI, the results confirm trends that were obtained by previous researches and validate them for the custom-built polarizer at our lab. The two main important results are the inverse relation between the optimal temperature and the xenon partial pressure, and the inverse relation between the xenon polarization and the xenon partial pressure.

As was stressed in the introduction, in the race for an imaging technique that would be efficient and economic at the same time, the HP gas MRI is easily pushed aside due to the requirement to purchase and maintain a polarizer. However, a custom built polarizer might reduce the cost and thereby will become feasible, but only if it could be optimized to the level of a high cost industrial polarizer. Regarding that issue, this study offers a contribution in two aspects: (1) it provides a comprehensive review on the theory which is needed for better understanding the optimization process, (2) and it demonstrates the optimization process experimentally, and thus provides guidelines for improving other custom-built polarizers.

To comply with the gas quantities demanded in clinical usages, continuous flow-mode polarizers may be more suitable than the batch-mode polarizers. In this work, the polarization build-up time was assumed to be no longer than 20 minutes (an assumption that was confirmed by obtaining similar results for longer polarization build-up time). In order to project the results of this work onto continuous flow-mode polarizers, it will have to be verified that the polarization build-up time is much shorter. That was not done in this project, since in the case of the xenon and nitrogen mixture, which was prepared

[5] At pressure of 1 Atm.

inside the cell, the mixture could not flow continuously. Accommodating the SEOP cell for a continuous flow mode using xenon and nitrogen remains a task for future work.

Other issues for future work will be (1) to increase the statistical significance of the results and (2) the modification of the results for variable laser power, mainly higher laser power. Regarding (1), although repetitions were made, as can be inferred from the errors, mainly in the case of the rubidium polarization, more repetitions may strengthen the results and consequently the conclusions. Regarding (2), using higher laser power may result in a polarization level sufficient for clinical usage. However, using a different value of laser power will give rise to different dependence of the polarization on the temperature and pressure (for example, a different optimal temperature might be obtained). Consequently, the conclusion regarding the optimal conditions for acquiring the maximized number of polarized xenon atoms per unit volume will have to be modified.

Finally, I would like to disclose the fact that all the information provided in chapter 1 was based on previous study. Moreover, the polarizer that is described in section 2.1 and the NMR coil that is described in section 2.2 ware not built by the author of this work; this project exploits only facilities that were already installed. However, previously the polarizer was operating in a flow-mode, and was modified for the purpose of this project to operate in a batch-mode. In addition, the theoretical discussion given in the appendix was based upon previous work. The measurement procedure described in section 2.3, although affected by the finding of previous research, was developed by the author to serve and address the specific goals and restrictions of the custom-built polarizer in the lab.

5. Appendix - Theory of Spin-Exchange Optical Pumping

5.1 Mathematical Background

5.1.1 Quantum Angular Momentum

5.1.1.1 Angular Momentum Operators, Eigenstates and Eigenvalues

Contrary to classical physics, the quantum angular momentum corresponds to Hermitian operators (observables) that operate in Hilbert space, namely, on a space that is spanned by the eigenstates of some observable. In the case where the Hamiltonian is commutative with the operators $\vec{J}^2$ and J_z of some angular momentum $\vec{J}$, the eigenstates that span the Hilbert space are common eigenstates of the Hamiltonian (namely, they have well-defined energies), $\vec{J}^2$ and J_z (namely, they have well-defined squared norms of the angular momentum, denoted by $\hbar^2 j(j+1)$ and well-defined values of a z component angular momentum, denoted by $\hbar m$) [32].

In the context of this work, the z component of the nuclear spin[6] of the xenon, for example, will be of interest, since it determines the polarization. The system (namely the Hamiltonian) does not need to be invariant under rotation whose generator[7] is the xenon nuclear spin in order to assign well-defined energies to the eigenstates of the z component of the xenon nuclear spin. That property is provided by the azimuthal symmetry with respect to the xenon nuclear spin.

In a hydrogen-like atom, such as rubidium,

$$\left[H,\vec{J}^2\right] = [H,J_z] = 0, \qquad 5.1$$

applies, where $\vec{J}$ is the total atomic angular momentum, neglecting the nuclear spin. One can deduce from eq. 5.1 that the square of the total angular momentum and its z component are constants of time. Moreover, the following can be stated: The quantum number *j* assumes the values,

$$|s-l| \le j \le |s+l|, \qquad 5.2$$

where l is the orbital angular momentum quantum number, which assumes the values $0 \le l \le n-1$, where *n* is an atomic energy level. Each value of *j* corresponds to a degenerate angular momentum subspace having a dimension of 2*j*+1. The 2*j*+1 states, denoted by $|jm\rangle$ and that span that subspace, are the eigenstates of J_z (thus, they are common eigenstates of $\vec{J}^2$ and J_z), having the eigenvalues $\hbar m$, where *m* is an integer. The values of *m* satisfy the inequality,

$$-j \le m \le j. \qquad 5.3$$

[6] Spins are angular momenta in the sense that they are representations of the generator (see the next footnote) of the rotation group, but they do not have the geometric properties of other representations that can be associated with a regular angular momenta, also known as an orbital angular momentum.

[7] The term generator comes from the group theory terminology; each rotation of the coordinate system is defined by a generator (of the rotation) which is identified as the angular momentum. If the system is invariant under a certain rotation, the angular momentum (or the generator) is a constant of time (Noether theorem).

For a given value of *n*, the energy assigned to each one of the subspaces (each one corresponding to a different value of *j*) is slightly different. Those energy gaps are known as the fine structure. By introducing the nuclear spin, the energy levels further split into sublevels characterized by the quantum number *f*. The total atomic angular momentum $\vec{F}$ is the addition of the nuclear spin $\vec{I}$ and the atomic angular momentum $\vec{J}$ that neglects the spin, in the same sense that $\vec{J}$ is the addition of the electronic spin and orbital angular momentum.

The eigenstate basis $|jm\rangle$ is not unique. One can also choose the basis where each one of the basis states has specified eigenvalues of the operators S_z and L_z, denoted by $|sm_s lm_l\rangle$. The former basis is called the sum space and the latter basis is called the multiplication space. Each one of them can be generalized to any kind of angular momenta.

5.1.1.2 Ladder Operators

In angular momenta algebra, often the operators,

5.4 $$J_+ = J_x + iJ_y$$
$$J_- = J_x - iJ_y \ ,$$

are introduced. The operation of the operators defined in eqs. 5.4 on an angular momentum state with the eigenvalues *j* and *m*, will be as follows,

5.5 $$J_+|jm\rangle = c_+(j,m)|j\ m+1\rangle$$
$$J_-|jm\rangle = c_-(j,m)|j\ m-1\rangle$$

5.6 $$J_+|jj\rangle = 0$$
$$J_-|j-j\rangle = 0 \ ,$$

where $c_+(j,m)$ and $c_-(j,m)$ are some constants that depend on *j* and *m*. Hence, the operation of the creation operator raises the z component of the angular momentum $\vec{J}$ by one unit, while the operation of the annihilation operator lowers it by one unit. They are known as the ladder operators.

Quantum operators may be expressed in terms of the ladder operators in order to clarify the effect of their operation on angular momentum eigenstates. As an example, the two spins, $\vec{S}_1$ and $\vec{S}_2$, and the effect of the interaction term $\vec{S}_1 \cdot \vec{S}_2$ on a state in the multiplication basis will be considered. Exploiting eq. 5.4, $\vec{S}_1 \cdot \vec{S}_2$ can be written as,

5.7 $$\vec{S}_1 \cdot \vec{S}_2 = \frac{1}{2}(S_{1+}S_{2-} + S_{1-}S_{2+}) + S_{1z}S_{2z} \ .$$

The first term lowers the angular momentum z component of the second spin state by one unit and raises the angular momentum z component of the first spin by one unit. The second term does the opposite. If the two spins are spin-1/2, in the case where the two spins are oppositely oriented (one is down and the other is up), exactly one of the first two terms will have a non-zero contribution to the

Hamiltonian. In other words, the terms in eq. 5.7 give rise to non-zero off-diagonal elements in the Hamiltonian. Such elements allow transitions between two quantum states to occur.

5.1.2 Density Matrix

5.1.2.1 The Interpretation of the Diagonal Density Matrix Elements

Basic quantum mechanics addresses small systems very efficiently. However, when an Avogadro number of particles is considered, an additional tool is employed, that is the density matrix formalism[8] [5]. For obtaining the expectation value of the observable *A,* one has to average over all the particles. Given that a portion of a_n particles are in the general state ψ_n, the expectation value of *A* is,

$$\langle A\rangle = \sum_{n=1}^{N} a_n \langle\psi_n|A|\psi_n\rangle, \qquad 5.8$$

where a_n is defined such that $\sum_{n=1}^{N} a_n = 1$, with *N* being the number of particles. Given the expansion of any of the general states in terms of basis states (when the summation is not explicitly specified, it is over of the basis states),

$$|\psi_n\rangle = \sum_i b_i^n |\phi_i\rangle, \qquad 5.9$$

eq. 5.8 can be rewritten as,

$$\langle A\rangle = Tr\{\rho A\}, \qquad 5.10$$

where ρ was defined as,

$$\rho = \sum_{n=1}^{N} a_n |\psi_n\rangle\langle\psi_n| = \sum_{n=1,ij}^{N} a_n b_i^n b_j^{n*} |\phi_i\rangle\langle\phi_j|. \qquad 5.11$$

Inspection of the elements of the density matrix reveals an important physical interpretation. For the purpose of this work, only the diagonal elements are relevant,

$$\langle\phi_k|\rho|\phi_k\rangle = \sum_{n=1}^{N} a_n |b_k^n|^2. \qquad 5.12.$$

Thus, each one of the diagonal elements represents an average weighted by the probability of each particle to be in the $|\phi_i\rangle$ state, and the number of particles that have such probability to be in the state. These elements of the density matrix will be referred to as populations.

The expectation value of the z component of the polarization vector, for example, can be easily calculated for spin-1/2 particles. Given the Pauli matrix,

$$\sigma_z = \begin{bmatrix} 1 & 0 \\ 0 & -1 \end{bmatrix}, \qquad 5.13$$

And using eq. 5.10, one obtains,

$$p = \langle\sigma_z\rangle = \rho_{\frac{1}{2}\frac{1}{2}} - \rho_{-\frac{1}{2}-\frac{1}{2}}, \qquad 5.14$$

[8] Although it is not restricted to many-body system.

where the following notation had been used,

$$5.15 \qquad \rho_{m_s m_s'} = \langle s' m_s' | \rho | s m_s \rangle.$$

More generally, the term polarization will refer to as the expectation value of the z component of some angular momentum, $\vec{J}$, with respect to *2j+1* eigenstates of a certain sublevel *j*.

5.1.2.2 Different Basis States

As it can be inferred from the formulation, the density matrix is not unique; it depends upon the choice of the basis states, $|\phi_i\rangle$. In eq. 5.14, for example, the basis states are the eigenstates of $\vec{S}^2$ and S_z. In the case of the angular momentum basis, the density matrix can be represented in a convenient way, namely, in a multipole expansion [5]. It can be summarized by the connection,

$$5.16 \qquad \rho = \sum_{jj'mm'} \langle j'm'|\rho|jm\rangle \, |j'm'\rangle\langle jm| = \sum_{jj'kq} \langle T(jj')^{\dagger}_{kq}\rangle T(JJ')_{kq}.$$

The term $\langle T(jj')^{\dagger}_{kq}\rangle$ is referred to as a statistical tensor, as it contains the statistical information of the system, similar to the coefficients $a_n b_i^n b_j^{n*}$, and is written as,

$$5.17 \qquad \langle T(jj')^{\dagger}_{kq}\rangle = \sum_{mm'} (-1)^{j-m} (2k+1)^{\frac{1}{2}} \begin{pmatrix} j & j' & k \\ m & m' & -q \end{pmatrix} \langle j'm'|\rho|jm\rangle,$$

where the third bracket on the r.h.s are the Wigner 3-j coefficients. The term $T(JJ')_{kq}$ is an operator taking the role of $|\phi_i\rangle\langle\phi_j|$, and can be expressed as,

$$5.18 \qquad T(JJ')_{kq} = \sum_{mm'} (-1)^{j'-m'} (jmj'-m;kq) \, |j'm'\rangle\langle jm|,$$

where the second bracket on the r.h.s are the Clebsch-Gordan coefficients. The utility of expression 5.16 is that the density matrix can be written in terms of the angular momentum whose eigenstates are used as the basis states, and their expectation values. Considering the case of spin-1/2 particles, for example, by using 5.16, the density matrix is reduced to [33],

$$5.19 \qquad \rho = \frac{1}{[S]} + \frac{3\langle\vec{S}\rangle\cdot\vec{S}}{S(S+1)[S]} = \frac{1}{2}\left(1 + \langle\vec{S}\rangle\cdot\vec{S}\right),$$

where $[s] = 2s+1$.

5.1.2.3 Time Evolution

The operator *O* evolves in time according to,

$$2.20 \qquad O(t) = U(t)O(0)U(t)^{\dagger},$$

Where *U(t)* is the evolution operator,

$$5.21 \qquad U(t) = e^{-\frac{iHt}{\hbar}}.$$

In order to obtain a representation where only perturbative operators will be time-dependent, it is required to transform from the Schrodinger picture into the interaction picture, by

$$5.22 \qquad O(t)_I = U_0(t)^\dagger O(t) U_0(t),$$

Where $U_0(t)$ relates to the unperturbed Hamiltonian by,

$$5.23 \qquad U_0(t) = e^{-\frac{iH_0 t}{\hbar}}.$$

To evaluate the change of the expectation value of *O* with time, 5.10 and the fact that in the Schrodinger picture observables are time-independent, will be used to obtain [5],

$$5.24 \qquad \frac{d}{dt}\langle O\rangle = Tr\left\{\left(\frac{d}{dt}\rho\right) O\right\}.$$

It will be assumed, that during each interval of time *T(O)*, the density matrix changes a little due to a small perturbation (this is the case where the particles compose gas and where collisions occur at a rate of $T(O)^{-1}$ per atom). The change in the density matrix (which when there is no perturbation, evolves according to eq. 5.22) due to the collisions can by expressed as,

$$5.25 \qquad \Delta\rho_I(t) = U_0(t)^\dagger U(t) \rho_I(t) U(t)^\dagger U_0(t) - \rho_I(t).$$

By defining,

$$5.26 \qquad M_{ev} = U_0(t)^\dagger U(t) M U(t)^\dagger U_0(t),$$

eq. 5.24 becomes [33],

$$5.27 \qquad \frac{d}{dt}\langle O\rangle = \frac{1}{T(O)} Tr\{(\rho_{I\,ev} - \rho_I) O\} = \frac{1}{T(O)} Tr\{(O_{ev} - O)\rho_I\}.$$

5.2 Optical Pumping

5.2.1 Atomic Transitions

The rubidium polarization process can be described in terms of the rubidium atomic states and the transitions between those states that are stimulated by a pumping light[9]. In the rubidium polarization process the atomic states of the ground level are redistributed such that an overpopulation is formed in one of these states. One of the most profound reviews on the topic of optical pumping was done by Happer [34] at 1972, and this description follows its guidelines. Another rather more simplified coverage on the topic by Happer was done 15 year later [50]. Earlier summary can be found in [53].

[9] A few terms will be used interchangeably that refer to the same thing: light, pumping light, exciting light and radiation refer to the word light. The word radiation will also be substituted for the word light.

Three main concepts are involved in the rubidium polarization process: the first stage of the process – the ground state depopulation by an exciting radiation, the evolution of the excited level's states, and the repopulation of the ground state.

5.2.1.1 Ground level Depopulation

Depopulation of the ground level occurs due to transitions induced by the interaction of the atom with excited radiation. The rate of these transitions is calculated by perturbation theory. The perturbation will be the dipole interaction between the rubidium atom and the exciting radiation. The exciting radiation can be represented by the electric field,

$$\vec{E} = \vec{\varepsilon} e^{i(\vec{k}\cdot\vec{r}-(\omega-\vec{k}\cdot\vec{v})t)} + c.c. \qquad 5.28$$

corresponding to monochromatic radiation with a general polarization. Different kinds of polarization will be manifested through $\vec{\varepsilon}$. The extra term that is subtracted from the frequency accounts for the effect of the atom's velocity $\vec{v}$. By considering the dipole interaction [35],

$$V = -\vec{E}\cdot\vec{D} \qquad 5.29$$

as a perturbation, the rate of the transitions that are induced by the radiation can be calculated using the Fermi golden rule [36]. The justification for using a perturbative approach is the large wavelength of the exciting light (795nm) in comparison to the scale of the rubidium atom (only few angstroms)[10]. The interaction term does not account for the spontaneous decay of the excited state back to the ground state. This decay can only be properly explained by principles of quantum electrodynamics. However, sufficient results can be obtained by introducing the parameter Γ, which can effectively account for the spontaneous decay by adding it to eq. 5.28 as an a decaying factor.

By following the prescription above, the rate of the transition from a sublevel *i* of the ground state to a sublevel *j* of the excited state is given by[11] [34],

$$R_{ij} = \frac{1}{\hbar^2}\frac{\left|\vec{\varepsilon}\cdot\vec{D}_{ij}\right|^2}{\left[\frac{\Gamma}{2}+i\left(\omega_{ij}+\vec{k}\cdot\vec{v}-\omega\right)\right]} + c.c. \qquad 5.30$$

where,

$$\omega_{ij} = \frac{1}{\hbar}\left(E_j - E_i\right) \qquad 5.31$$

with E_i being the energy of the sublevel *i*. The matrix element $\vec{\varepsilon}\cdot\vec{D}_{ij}$ in the basis of the angular momentum states determines the selection rules. The allowed transitions should meet the requirements of the addition of the angular momenta, namely, the addition of the spherical components of the *i* (initial) state with the spherical components of the electric dipole, which should give the spherical components of the *j* (final) state (note that only the electric dipole is an operator;

[10] That approximation known as the dipole approximation.
[11] For clarification it will be noted that the arrows (as in $\vec{\varepsilon}$, for example) signify 3-dimenssion vectors, where the indices i and j signify states in Hilbert Space.

however, the scalar product with the classical vector of the polarization will determine the selection rules since it will determine which components of the electric dipole will contribute).

For a given initial angular momentum *i* state $|fm\rangle$, and a final *j* state $|f'm'\rangle$, the fact that $\vec{D}_{ij}$ is a tensor of rank one dictates that the angular momentum of the excited state can assume the values,

$$5.32 \qquad |f-1| \leq f' \leq f+1\ .$$

Parity symmetry consideration requires that $f \neq f'$ (in fact, it requires that $|fm\rangle$ and $|f'm'\rangle$ will have a different parity, but with eq. 5.32 that statement is redundant). So,

$$5.33 \qquad \Delta f = f' - f = \pm 1.$$

The selection rule of the quantum number m will be determined according to the light polarization. In general, given q as the magnetic number of the electric dipole tensor,

$$5.34 \qquad \Delta m = m' - m = 0, \pm 1$$
$$m' = m + q\ .$$

Hence, q determines the allowed transitions. In the case where $D_q^k = D_0^1$ (where k is the rank of the tensor) only $\Delta m = 0$ will prevail, meaning that there will be no change in the longitudinal component of the atomic angular momentum. In the case of contributions from D_1^1 and D_{-1}^1, Δm can assume only the values ± 1.

In terms of populations, eq. 5.30 describes the rate at which the population of the state *i*, denoted by ρ_{ii} is depleted. It cannot be ascribed to the rate of populating of the state *j*, as the population of the state *j* may depend on transitions that relate it to other ground states.

To conclude, the allowed atomic transitions between a specific state at the ground level to another specific state in the excited level, are determined by the spherical properties of the electric dipole tensor. Due to the scalar product of the electric dipole with the light polarization vector, the components of the electric dipole that will contribute in eq. 5.30 depend on which are the non-zero components of the light polarization when it is expanded in spherical coordinates (see section 5.2.4).

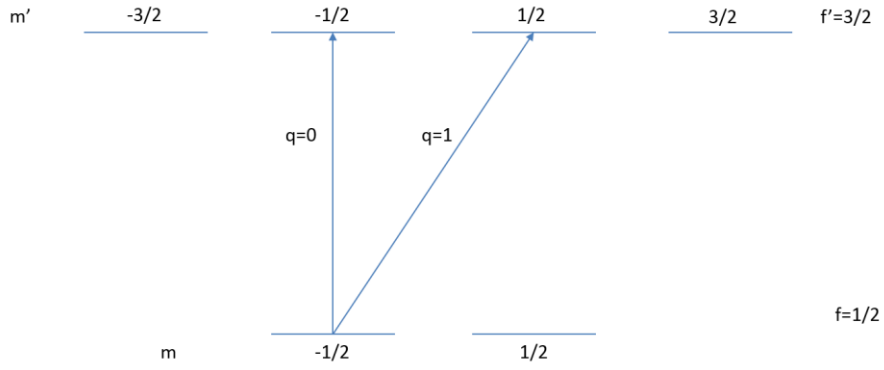

Figure 5.1 Demonstration of the magnetic number's selection rule for the transition $f = \frac{1}{2} \rightarrow f' = \frac{3}{2}$.

5.2.1.2 Excited State

Evidently, the excited level populations are closely related to the rate equation 5.30. The change of the population of a specific excited state *j* will generally have contributions from all the ground states of the ground level [34],

$$5.35 \qquad \frac{d}{dt}\rho_{jj} = \sum_i R_{ij}\rho_{ii} \ .$$

The summation in eq. 5.35 is substantially limited by the selection rules encoded within the rate coefficients.

The excited level polarization depends on the light polarization and the ground level polarization in a manner that can be inferred from figure 5.1. The light polarization will determine which transitions are allowed (or in the language of figure 5.1, which values of q will contribute to eq. 5.35), and the ground state polarization will determine whether there are atoms with the relevant ground state occupied. In figure 5.1, for example, whether the ground state $m = \frac{1}{2}$ is occupied or not will influence the occupation of the excited state $m' = \frac{1}{2}$ in the case of q=0. Thus, selecting a proper light polarization may lead to excited level polarization. Referring again to figure 5.1, radiating the atoms with light polarization corresponding to q=1 transition, will leave the states $m' = -\frac{3}{2}$ and $m' = -\frac{1}{2}$ unpopulated, giving rise to excited level polarization, even with a ground state level that is completely unpolarized [35].

Nevertheless, the initial excited level polarization may not persist long, due to three main mechanisms [34]: interaction with external electric and magnetic fields, collisions with other atoms, and the hyperfine interaction. The longer the excited level exists, the higher the probability that it will become unpolarized. The hyperfine interaction, for example, will cause the excited level (and the ground level) to split into hyperfine sublevels, each corresponding to a different value of the total angular momentum quantum number, f. However, because the energy gaps are small (a few GHz [31]), a change in the electronic spin orientation may occur in a duration longer than the average time between collision of the rubidium atoms. The most important mechanism leading to excited level depolarization is the relaxation mechanism. The collisions of rubidium atoms with buffer gas atoms enhance the relaxation and induce fast excited level depolarization. The importance in the presence of a buffer gas relates to the light absorption efficiency of the rubidium and will be discussed in 5.2.3.2.

5.2.1.3 Ground State Repopulation

An analogous expression to the depopulation rate of the l ground state will be the repopulation rate of the ground level l due to a spontaneous decay from the excited state *k*. This expression can be obtained by quantum electrodynamics consideration, and can be written as [35],

$$5.36 \qquad A_{kl} = \frac{4e^2\omega_{kl}}{3m^2c^3\hbar}|\langle l|\vec{p}|k\rangle|^2.$$

Hence, in the case of spontaneous decay, the selection rules of the transitions are determined by the matrix elements of the atomic momentum. The total contribution to the change in the population of the ground state l due to spontaneous decay from all the excited states, will be [34],

$$\frac{d}{dt}\rho_{ll} = \sum_k A_{kl}\rho_{kk}. \qquad 5.37$$

The ground level can acquire polarization either by depopulating pumping or by repopulating pumping. The latter is governed by eq. 5.37 and the selection rules encoded in eq. 5.36. An important condition for the repopulating pumping is that the spontaneous decay rate will be much larger than the depolarization of the excited level. If, for example, the excited state $m' = \frac{1}{2}$ becomes populated (see figure 5.1), the selection rules in eq. 5.36 will determine the ratio in populations for the ground states level. That is known as repopulating pumping [34].

However, the optical pumping in this experiment is based upon depopulating pumping, namely, instead of relying upon the spontaneous decay to form the overpopulation of certain states needed for polarization, the overpopulation is achieved by constantly depleting the other state. There is still a role reserved for the spontaneous decay: it populates the ground states where the overpopulation of certain states constitutes the atomic polarization. The spontaneous decay also populates other states (according to the selection rules), but those are being constantly depopulated. Hence, this kind of polarization process is known as depopulating pumping.

5.2.2 Rubidium Optical Pumping

As in any other alkali metal, the rubidium atom has one valance electron. The inner shells have not much chemical significance, but physically they dictate a smaller energy gap between the ground and the excited energy levels of the valance electron. This is due to the screening effect formed by the core electrons that screen the electric Coulomb field produced by the nucleus. Thus, the energy gap is reduced as compared with hydrogen atom. The energy gap corresponds to the energy of a photon with a wavelength of 795 nm, which is the same wavelength of the radiation produced by industrially manufactured lasers, and thus makes the rubidium compatible with optically pumped experiments.

In the basis of the total angular momentum, *J* (neglecting the nuclear spin), the first excited state has two angular momentum states, whose degeneracy is lifted due to fine structure interaction. The transition that corresponds to the 795 nm wavelength is labeled D-1, where for the second transition, D-2, the energy gap is slightly lower and corresponds to 780 nm wavelength.

Natural abundant rubidium contains two stable isotopes: 72.17 % ^{85}Rb and 17.83 % ^{87}Rb, having a nuclear spin of $I = \frac{5}{2}$ and $I = \frac{3}{2}$ respectively. This induces further splits, in what is known as the hyperfine structure. Since the hyperfine structure associated with the nuclear magnetic moment, which is 3 order of magnitude smaller than the electronic magnetic moment, it can be ignored.

Given that the excited radiation changes only the orbital angular momentum (from L=0 to L=1) and the z component of the spin [35], the transition diagram for the optical pumping process can be summarized based on principles of section 5.2.1 (see diagram 5.2).

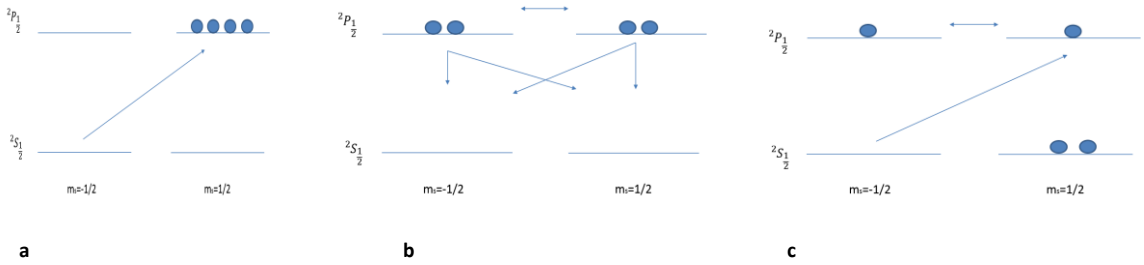

Figure 5.2. **a** Depopulating radiation depopulates the ground down state and overpopulates the excited up state of the electronic spin due to its circular polarization. **b** The excited level becomes unpolarized and the atoms decay back to ground level through spontaneous decay and due to quenching radiation collisions. **c** The ground down state continues to be depopulated, and thus a polarization is formed at the ground level.

5.2.3 Radiation and Absorption Spectral Lines

5.2.3.1 Overview

According to the description above, the probability that a photon will be absorbed by an atom has a sharp peak at the frequency domain corresponding to the atomic energy gap. However, several considerations, which stem mostly from the interaction of each single atom with its environment via collisions, but also from causes that are inert to the atom, modify this idealistic description. The dependence of the absorption probability, or the cross section (which is tightly related to the absorption probability) [36] on the frequency, is usually presented as a curve that will be referred to as the absorption spectral line. The shape of the curve, due to the nature of its origins, is either Lorentzian or Gaussian, according to which origin is the dominant. In the case of a "clean" physical system with no external perturbations, the line shape will be Gaussian whereas when environmental effects are dominant, the line shape becomes Lorentzian.

A comment should be made regarding the comparison between the absorption spectral line and the exciting radiation spectral line as well as the consequences of their properties. The radiation spectral line, as well as the absorption spectral line, are assumed to have a Lorentzian shape. A continuous progression in the field of lasers makes the light source more coherent and more monochromatic. In this work, for example, the full width at half maximum (FWHM) of the spectral line is in the order of a few angstroms (see section 2.1.2). It is desirable to obtain as well-defined frequency as possible, since broad FWHM, in the context of optical pumping experiments, leads to inefficient conversion of photon flux to atomic angular momentum, due to a large segment of photon flux that is off-resonance [37-39].

A few angstroms correspond to a few 10^5 GHz, which is 5-6 orders of magnitude larger than the FWHM of the absorption spectrum [38]. Thus, every narrowing in the laser spectral line will improve the conversion of the photon flux to the atomic angular momentum. On the other hand, it would be a very good approximation to assume a uniform frequency profile of the radiation (a flat spectral profile), since

the flux intensity in the spectral area that is close to the absorption line does not change much as a function of the frequency. The flux can by described by,

$$\Phi(\nu) = cu \quad (5.38)$$

where c is the speed of light, and u is the energy density per unit frequency. This relation will be further exploited in the section 5.2.4.

5.2.3.2 Pressure Broadening

The theory behind the influence of pressure on the atomic levels was well explained in the early work of Margenau and Watson in [40]. Any interaction of the atom with its environment slightly shifts the original energy levels, causing deviations from the exact values of energy differences between them. Accordingly, it might happen that a photon with an energy, which is not exactly the energy deference of two levels of the unperturbed atom, may be still be absorbed by the atom. Several kinds of changes in the spectral line were observed with respect to pressure variation: energy shift [41], satellite lines [40], asymmetric deviation from the Lorentzian dispersion [42] and, of interest in this study, is broadening [43, 54].

Pressure broadening is a subject that is hard to address with fundamental physical principles due to its complexity. Therefore, models with assumptions that are valid in certain conditions behind them were formulated to account for the effect. One early model is the impact theory [44] that uses a classical approach. Another model treats the system of the optically pumped atom with the perturbing atoms as a quasi-molecule, based on the fact that the atom experiences the perturbations constantly, in what is known as the quasi-molecular model [45]. This model addresses only the case of one-atomic buffer gas. The requirement to include two nuclei with each perturber (such as in this study, where one of the perturbers (i.e. the buffer gas atoms) is a nitrogen molecule) increases the degrees of freedom dramatically and accordingly, the complexity of the model [46].

In this study, nitrogen and helium serve as the buffer gases creating the pressure broadening in two different setups: the first is a combination of the two, and in the other the nitrogen alone is used. It should be mentioned that the nitrogen has an additional role in the optical pumping of the rubidium: it quenches the radiation emitted as a result of the decaying of the rubidium from the excited state to the ground state. A photon that is emitted due to spontaneous decay will propagate in an arbitrary direction with an arbitrary polarization, thereby depolarizing a rubidium atom that it might collide with. By collisions with nitrogen molecules the energy of the excited atom is transferred to the vibrational and rotational degrees of freedom of the nitrogen molecules, and thus the decaying back to the ground state occurs without the emission of a photon.

5.2.3.3 Doppler Effect

This section examines the effect of the velocity of the atoms on the atomic spectral line. Generally, it can be referred to as a Doppler effect, since the kinetic energy shifts the atomic energy gap. Due to a certain velocities' distribution, assumed to be Gaussian, the energy gap will present a Gaussian

distribution around the value of the energy gap of a static atom. Heuristically, it can be explained by the small shift of the energy level of two atoms that possess two different velocities. The averaging is done by factorizing each contribution to the polarizability tensor from a certain velocity by its proper weight, namely, the probability of finding the atoms in that velocity. The three-dimension velocities' Gaussian distribution is also known as the Maxwell-Boltzmann distribution,

$$5.39 \qquad N(\vec{v}) = \left(\frac{M}{2\pi RT}\right)^{\frac{3}{2}} e^{\frac{-Mv^2}{2RT}},$$

where T is the temperature, M is the molar mass and R is the gas constant.

The broadening of the atomic spectral line has to be compared with similar effects that stem from other sources like Γ and pressure broadening. The minimum value of these effects is approximately a few GHz. The frequency Doppler broadening can be estimated by [34],

$$5.40 \qquad f_D = \frac{k(2RT)^{\frac{1}{2}}}{M^{\frac{1}{2}}}.$$

Setting k to correspond with the rubidium *D1* transition, $M = 86m$ and $T = 350K$, obtains $f_D \cong 8MHz$, which is three orders of magnitude less than the typical broadening effects of other sources. Therefore it will be sufficient to consider the lowest order in the corrections, which according to the above consideration, does not contribute to the absorption spectral line broadening.

To conclude, it can be stated that the conditions in the cell, from the aspect of thermodynamics and optics, are such that the velocity of the atoms is sufficiently well-defined, and thereby permits to assume a Lorentzian spectral line for the absorption process.

5.2.4 Light Absorption

The radiation absorption can be described within the regime of low gas density, which allows the assumption of linear susceptibility[12]. Physically, it means that the gas is so diluted that the amplitude of the electric field changes within much larger length scale (or equivalently, it significantly changes only over the length of the entire cell, which is a few tens of centimeters) than the wavelength. That permits the beam of the excited radiation to serve also as a probe beam that provides information regarding the atomic polarization. Moreover, it can be assumed that the light polarization spans the transverse plane with respect to the direction of propagation, with no longitudinal component.

The two-dimensional light polarization vector evolves according to [47],

$$5.41 \qquad \frac{d}{dz}\vec{\varepsilon} = 2\pi i \mathrm{X}^{\perp}\vec{\varepsilon}$$

where $\mathrm{X}^{\perp}$ is the projection of the susceptibility tensor on the transverse plane. Hence, by choosing harmonic solutions to eq. 5.41, one obtains the following eigenstates equation,

[12] Meaning that there is a linear relation between the light polarization and the electric field via the susceptibility tensor.

5.42 $$2\pi \mathrm{X}^{\perp} \cdot \hat{e}_{\lambda} = (k_{\lambda} - k)\hat{e}_{\lambda}.$$

The light polarization can then be expressed in terms of the two eigenvectors, including at the moment of entrance into the cell,

5.43 $$\vec{\epsilon}(0) = \hat{e}_1 a_1 + \hat{e}_2 a_2.$$

The phase velocities are determined by the eigenvalues k_{λ}. As the light travels a distance l, the electric field will be,

5.44 $$\vec{\epsilon}(l) = \vec{\epsilon}(0) \cdot e^{2\pi i \mathrm{X}^{\perp} k l}.$$

It is interesting to point out that $X^{\perp}$ has an analogous role in the evolution of the electric field under the influence of gas, to the role of the Hamiltonian in a quantum system. The analogy is constituted on the relations with other physical identities: the electric field is analogous to the wave function, and the eigenstate equation to the stationary Schrodinger equation. By expanding eq. 5.44 to first order in $\mathrm{X}^{\perp}$, it has been shown [48] that the change in the light intensity after propagating distance l inside the cell is,

5.45 $$\Delta I = \int d\nu \Phi(\upsilon) \int_0^l dz \, 2\pi i k N \hat{e}^* \cdot \alpha^{\perp} \cdot \hat{e} + c.c.$$

where, $\mathrm{X}^{\perp} = N\alpha^{\perp}$, and N is the optically pumped gas density. The term $2\pi i k N \hat{e}^* \cdot \alpha^{\perp} \cdot \hat{e}$ is known as the absorptivity.

From inspection of the integrand in the first integration in eq. 5.45, it may be considered as an infinitesimal contribution that proportional to the withdrawal of energy from light at the infinitesimal length element dz somewhere along l. Since this withdrawing was taken from a light with specific frequency ν, the contribution from all the other frequencies has to be taken into account. That explains the second integration.

The expression in eq. 5.45 should be regarded as proportional to the spin dependent cross section of an atom-photon collision. The absorption coefficient is related to $\alpha^{\perp}$, which its spherical symmetry properties impose selection rules based on the angular momentum states of the atoms that are composed from the electronic spin as well. The light absorption is also light-polarization dependent, which is evident by the multiplications with $\hat{e}$.

It is beneficial to review light polarization vectors in terms of the quantum mechanics eigenstate of the angular momentum operator, since by that the selection rules discussed here and in 5.2.1 can be explained in terms of angular momentum conservation. Quantum mechanically, the photon is a spin-1 particle, meaning that the angular momentum states of the photon can be represented by a three dimensional vector [35]. The relation to the Cartesian component polarization (which should not be regarded other than the same phenomenon, namely the direction of the electric field, besides the fact that it is represented in other set of coordinates) to the z component angular momentum eigenstates is given by,

$$5.46 \quad \hat{e}_1 = -\frac{1}{2^{\frac{1}{2}}}(\hat{x} + i\hat{y})$$
$$\hat{e}_0 = \hat{z}$$
$$\hat{e}_{-1} = \frac{1}{2^{\frac{1}{2}}}(\hat{x} - i\hat{y}).$$

Left circular polarized light will correspond to $\hat{e}_1$ polarization. Again in the quantum mechanical language, the photonic system would be in an angular momentum state corresponding to $m_z = 1$. The eigenstate $\hat{e}_{-1}$ corresponds to left circular polarization and the analogy to quantum mechanics is clear. Linear or elliptic polarization will be a superposition of those two. The fact that the light can have only transverse polarization is translated to quantum mechanics by leaving the $m_z = 0$ state not realized. The fact that the 3-dimension Hilbert space of the photon is reduced to 2-dimension Hilbert space due to electrodynamics considerations stands behind the treatment of the photon as a spin-1/2 particle in quantum optics experiments [35].

A term strongly related to eq. 5.45 and that is used in the experimental section is the absorption coefficient of the light. Generally, the absorption of the light is a localized property, therefore it is proportional to the spatial derivative of the expression in eq. 5.18. By assuming that the rubidium polarization is uniform across the cell, the integration over the light path will factorize the expression by l, thereby making the differentiation with respect (to the distance to obtain the absorption coefficient) trivial, and l is cancelled.

To conclude, given a right-handed circular polarized light and a uniform rubidium polarization, the absorption coefficient will be composed out of a spin-independent cross section, and a spin-dependent part that imposes the selection rules: In the case of optically pumped rubidium it should account for the fact that no absorption occurs in the case where the atoms are at spin up. Hence it can be simply expressed as [39],

$$5.47 \quad A = \sigma N_-,$$

where σ is the spin-independent cross section for the photon-atom collision, and N_- is the density of atoms in a spin up state.

5.2.5 The Polarization Equation

The expression for the polarization as a function of time now will be derived while ignoring the nuclear spin[13]. Accordingly, the density matrix should describe only two ground states and thus be 2-dimensional matrix. For calculating the rubidium polarization, one should consider the populations.

The evolution of the populations will be constructed based on physical consideration. The change in the up state is proportional to the optical pumping rate per atom, γ_{op}, and to the population of the down state that initiates the process. On top of that, the spin relaxation term should be added.

[13] By describing the optical pumping as a process that transfers angular momenta, the nuclear spin can be regarded as another reservoir that the angular momentum of the light can be transferred to. However, the only effect that it has is in slowing down the rubidium polarization process [19].

Relaxation processes will be covered in a later chapter, and the relaxation of the rubidium will be denoted by the constant Γ_{sd}, which accounts for all the relaxation processes of the rubidium polarization. Thus the evolution of the population of the up state is given by [49],

$$5.48 \qquad \frac{d\rho_{\frac{11}{22}}}{dt} = -\frac{\Gamma_{sd}}{2}\left(\rho_{\frac{11}{22}} - \rho_{-\frac{1}{2}-\frac{1}{2}}\right) + \gamma_{op}\rho_{-\frac{1}{2}-\frac{1}{2}}.$$

The first term that corresponds to the relaxation is proportional to the difference in the up and down population; at completely unpolarized state, no relaxation can occur. The discussion in section 5.2.4 is closely related to the optical pumping rate per atom, but from the point of view of light attenuation. Here, γ_{op} describes the absorption efficiency of light by an atom. Hence, similar to the arguments that were stressed in 5.2.4, the optical pumping rate per atom will correspond to an effective absorption that depends on the overlap integral of the spectral line from the light part, and the spin-independent cross section from the atomic part (the selection rules are encoded within the way the evolution equation is constructed). Thus, the optical pumping rate per atom can be written as,

$$5.49 \qquad \gamma_{op}(\vec{r}) = \frac{1}{2\pi}\int \Phi(\vec{r},\omega)\sigma(\vec{r},\omega)d\omega,$$

where in this notation, γ_{op} is the special average of $\gamma_{op}(\vec{r})$.

A similar equation to eq. 5.48 can be written for the down state. By combining the two equations and by the definition of the rubidium polarization (see section 5.1.2.1),

$$5.50 \qquad p_{rb} = \rho_{\frac{11}{22}} - \rho_{-\frac{1}{2}-\frac{1}{2}},$$

one obtains the differential equation for the rubidium polarization,

$$5.51 \qquad \frac{d}{dt}p_{rb} = \gamma_{op}(1 - p_{rb}) - \Gamma_{sd}p_{rb},$$

with the solution,

$$5.52 \qquad p_{rb} = \frac{\gamma_{op}}{\Gamma_{sd}+\gamma_{op}}\left(1 - e^{-t(\Gamma_{sd}+\gamma_{op})}\right),$$

given an unolarized initial state.

5.3. Spin Exchange

5.3.1 Overview

The SEOP can be described in a flowchart of angular momenta (see figure 5.3). The circular polarization of the light constitutes the source; spin destruction processes (see section 5.4) prevent complete transfer of the angular momentum, and thus even at a steady state, the polarization level of the rubidium will depend on the dominancy of these processes. By colliding with xenon atoms, part of

the angular momentum that is stored in the rubidium[14] is lost to the angular momentum associated with the rotation of the rubidium and the xenon atoms around each other. The other part is transferred to the nuclear spin of the xenon in such a way that the latter will be oriented similarly to the orientation of the rubidium spin, prior to the collision. Such a process is known as spin-exchange, and its idea is easily conveyed symbolically,

$$5.53 \qquad Rb(\uparrow) + Xe(\downarrow) \rightarrow Rb(\downarrow) + Xe(\uparrow).$$

Analogically to the rubidium polarization destruction, depolarization processes deteriorate the ultimate xenon polarization levels [27].

Every kind of spin transfer that was mentioned in this preliminary description will be explained (or has been already explained) in terms of spins and angular momenta interactions. Unlike the angular momentum transfer between the light and the rubidium, the mechanism of the spin transfer between the rubidium and the xenon should be inspected more carefully with respect to different pressure regimes [33]. However, the spin interactions in each of these regimes are always of the same kind, which grants section 5.3.2 with generality. The following description follows the guidelines presented in [33]. Another treatment can be found in [60].

The total electronic wave function of a noble gas is spherically symmetric and thus corresponds to zero angular momentum. Therefore, no interaction that depends on any form of xenon electronic angular momentum can take place in the event of collision with another particle. However, 26.4% out of the xenon gas in its natural abundance is the xenon isotope ^{129}Xe that possesses a spin-1/2 nucleus. The description of the spin-exchange is based on the assumption that a bound state is formed for a short time (also is known as correlation time) in which the two atoms are revolving around each other [51]. The term "short time" is used to distinguish fast collisions from a stable molecule that persists at any timescale longer than micro seconds; the persistence is not restricted to a well-defined short timescale. Collisions have a large range of bound state duration, from 10^{-7} to 10^{-12} seconds [33]. Section 5.3.2 will focus on a description that is independent of the lifetime of the bound state, which is closely related to the statement above about the pressure regime, since the lifetime of the RbXe molecule[15] is closely related to the pressure. In sections 5.3.3 and 5.3.4 the classification to short and long lifetime molecules and their applications will be discussed.

[14] The polarization associated with the rubidium is sometimes ascribed to the rubidium's valance electron. Since there is no description preferred over the other, the rather more compact term of rubidium polarization will be employed. However, it will often be convenient to refer to it as the electronic spin.

[15] Due to its short lifetime, it is often referred to in the literature as a quasi-molecule. It is also referred to as a Van-Der-Waals molecule. For abbreviation, here it will only be referred to as a molecule.

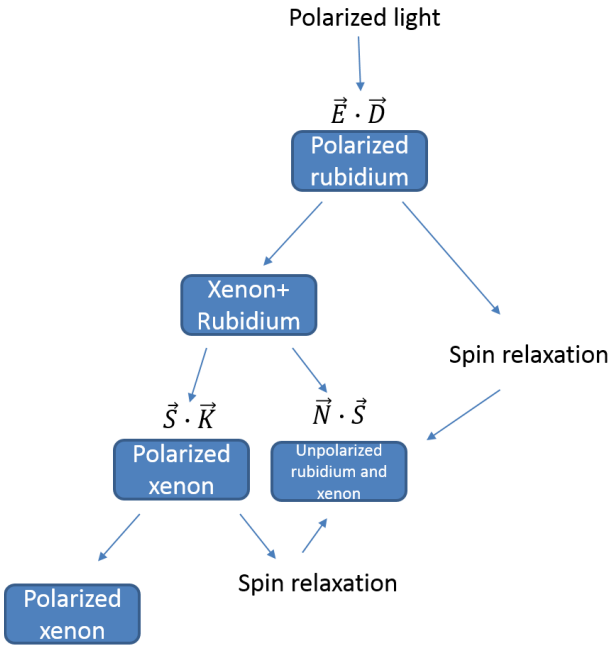

Figure 5.3. A flowchart that describe roughly the SEOP process. The angular momentum is transferred according to the direction of the arrows. The scalar multiplications will be explained later.

5.3.2 Spin Transfer Formulation

This section offers a brief guideline for reconstructing the spin exchange formulation (it follows the treatment given by Happer *el al* [33]). The explicit calculations were not included, but the relevant quantities and their relations with each other, as well as the principles of the formulation are presented. The starting point will be an approximated Hamiltonian. With the aid of the density matrix machinery and the multipole expansion, the ending point will be an equation that is parallel to eq. 5.51, i.e. a differential equation according to which the expectation value of the longitudinal component of the nuclear xenon polarization evolves in time.

5.3.2.1 Perturbative Approach

The spin-dependent Hamiltonian[16] of the total system of the rubidium and the xenon atoms consists of the following contributions [33],

$$H = A\vec{I} \cdot \vec{S} + \gamma\vec{N} \cdot \vec{S} + \alpha\vec{K} \cdot \vec{S} + g_S\mu_B\vec{B} \cdot \vec{S} + g_I\mu_B\vec{B} \cdot \vec{I} + \\ + g_K\mu_B\vec{B} \cdot \vec{K} + \cdots, \qquad 2.54$$

where μ_B is the Bohr magneton and g_i is the Lande g-factor that is associated with the i angular momentum; $\vec{S}$, $\vec{I}$ and $\vec{K}$ are the spin of the rubidium's valance electron, the rubidium's nucleus and the xenon nucleus, respectively; $\vec{N}$ is the rotational angular momentum of the molecule. The first term

[16] The Hamiltonian includes also an electrostatic attraction term which determines the strength of the bond. The question of the bond stability will be addressed in section 3.3. Here only spin-dependent terms are considered.

corresponds to the hyperfine interaction of the rubidium atom. The second term corresponds to the interaction of the electronic spin with the molecular angular momentum. The molecular centrifugal force usually gives rise to an angular momentum that is of a larger scale than any other angular momentum (or more specifically, spin) in the system. Hence, $\vec{N}$ is usually large [51] (it can be about tens of units of $\hbar$, while as was already stated in section 2.2.2, $\vec{S}$ or $\vec{I}$ corresponds to $\frac{1}{2}$, $\frac{3}{2}$ or $\frac{5}{2}$ $\hbar$). That fact deteriorates the spin transfer efficiency. Since the electronic spin interacts with such a large angular momentum, most of the polarization is lost in this interaction. In fact, on average, in each collision only less than 10% of the polarization is transferred to the xenon nuclear spin [33]. The hyperfine interaction that is responsible for the spin exchange is expressed in the third term. The other three terms are the coupling of the magnetic field to the electronic spin, the rubidium nuclear spin and the xenon nuclear spin.

The direction of the external magnetic field that served as the symmetry axis in the analysis of a single atom and photon system can no longer serve as such, as another preferred direction is introduced into the system combined out of two atoms; that is, the direction perpendicular to the plane of rotation of the two atoms (the direction of $\vec{N}$). However, the interaction of the electronic spin with the molecular angular momentum can be put on equal footing with the interaction with the magnetic field (the standard Zeeman interaction) by assigning a rotational frequency [33],

$$\vec{\omega}_1 = \frac{\gamma \vec{N}}{\hbar}, \qquad 5.55$$

where γ is a constant associated with the strength of the interaction, which makes the units match. Thus a new direction can be defined, one that gives rise to an interaction of the electron with an effective magnetic field,

$$\vec{\omega} = \vec{\omega}_1 + \vec{\omega}_0 = \omega \hat{\xi}, \qquad 5.56$$

where $\vec{\omega}_0$ is at the direction of the external magnetic field, having a magnitude that is equal to the electronic Larmor frequency.

In anticipation of the usage of the perturbation theory, a part that does not contain an interaction with the xenon nuclear spin is defined (since the nuclear spin Zeeman splitting of the two nuclei is not important for the discussion, it was disregarded),

$$H_0 = A\vec{I} \cdot \vec{S} + \hbar\vec{\omega} \cdot \vec{S} = A\vec{I} \cdot \vec{S} + \hbar\omega S_\xi \ . \qquad 5.57$$

Each term reflects a different order of magnitude: the first term corresponds to the fine interaction in the rubidium atom having energy gaps associated with a frequency of about $\frac{A}{2\pi\hbar} \cong 3400\ MHz$ [33]. The second term corresponds to the effective Zeeman splitting with frequency of about $\omega = 116\ MHz$ (the values are for $^{87}Rb^{129}Xe$ molecule). Since it is desirable to work in the basis of the total atomic angular momentum where $\vec{I} \cdot \vec{S}$ is diagonal, $\vec{S}$ will be expressed in terms of the projections of the total angular momentum on each of its subspaces (see section 5.1.1.1), which corresponds (in the case of an electron) to two multiplets [33, 52],

$$5.58 \qquad f = \begin{cases} a = I + \frac{1}{2} \\ b = I - \frac{1}{2} \end{cases},$$

as[17],

$$5.59 \qquad \vec{S} = \frac{1}{[I]}\left(\vec{a} - \vec{b}\right),$$

where $[x] = 2x + 1$. The important interaction between the electronic spin and the xenon nuclear spin is considered to be the small perturbation, which is written as,

$$5.60 \qquad V = \alpha \vec{K} \cdot \vec{S},$$

where for $^{87}Rb^{129}Xe$ molecule, $\frac{\alpha}{2\pi\hbar} = 37\ MHz$ [33]. Only the square of the strength of interaction constants will have physical relevancy, and thus it can be safely stated that the condition,

$$5.61 \qquad A^2 \gg (\gamma N)^2 \gg \alpha^2,$$

applies.

5.3.2.2 Evolution of the Expectation Values

Using the evolution operator (see section 5.1.2.3), any component of the angular momentum $\vec{Y}$ will be calculated by,

$$5.62 \qquad Y_{ev} = U^{-1} U_n Y U_n^{-1} U.$$

The evolution of the expectation value of Y is given by (again, see section 5.1.2.3),

$$5.63 \qquad \frac{d}{dt}\langle Y \rangle = \frac{1}{T(Y)} Tr\{(Y_{ev} - Y)\sigma\},$$

where σ is the density matrix in the interaction picture, and $\frac{1}{T(Y)}$ is the formation rate per atom for the atoms having any sort of angular momentum $\vec{Y}$. The fact that $T(Y)$ is much larger than τ, the average lifetime of a molecule, implies that there is no interaction between atoms during the time interval between collisions. Thus it can be assumed that at the instant when two atoms are binding together, the density matrix can be written as an outer product of the rubidium and the xenon separated density matrices,

$$5.64 \qquad \sigma = \sigma_{Rb}\sigma_{Xe},$$

where each of the uncoupled density matrices can be written down as a multipole expansion (see section 5.1.2.3),

[17] This fact can be shown heuristically by representing geometrically the vectors $\vec{a}$ as the addition of $\vec{I}$ and $\vec{S}$, and the vector $\vec{b}$ as their subtraction. Then, the subtraction of $\vec{b}$ from $\vec{a}$ will give a vector in the direction of $\vec{S}$. In order to bring its magnitude to that of $\vec{S}$, it has to be divided by $[I]$.

5.65 $$\sigma_{Rb} = \frac{1}{2[I]} + \sum_f \frac{3\langle\vec{f}\rangle\cdot\vec{f}}{f(f+1)[f]} + \cdots$$

5.66 $$\sigma_{Xe} = \frac{1}{[K]} + \frac{3\langle\vec{K}\rangle\cdot\vec{K}}{K(K+1)[K]} + \cdots .$$

In eq. 5.65, $S = \frac{1}{2}$ has been substituted and the summation includes the two multiplets of f. The dimension of σ is $2[I][K]$. In the case of xenon, $K = \frac{1}{2}$, and the expansion in eq. 5.66 contains only the first two terms. However, keeping the noble gas nuclear spin unspecified will emphasize the generalization feature of this method.

Substituting eqs. 5.62, 5.64, 5.65 and 5.66 into eq. 5.63 gives rise to the following expression for the evolution of the expectation value of the $\vec{Y}$ angular momentum [33, 52],

5.67 $$\frac{d}{dt}\langle\vec{Y}\rangle = \frac{1}{T(Y)}\sum_L\left[q(Y,L)\langle\vec{L}\rangle - \vec{S}(Y,L)\right],$$

where $q(Y,L)$ is known as the spin transfer coefficient. The only effect that $\vec{S}(Y,L)$ has is shifting the Larmor frequency of the nuclear xenon spin and the electronic spin, and thus will be ignored. The trace, the evolution operators and the numerical factors of the terms of the multipole expansions are all part of the definition of $q(Y,L)$.

5.3.2.3 Spin Transfer Coefficient

The spin transfer coefficient which relates the expectation value of some angular momentum $\vec{L}$ to the time derivative of the expectation value of $\vec{Y}$ will contain contributions from allowed transitions determined by terms of the form (see eq. 5.67),

5.68 $$\mathcal{g}_{ij}\left(\vec{Y},\vec{L}\right) = \langle i|\vec{Y}|j\rangle\cdot\langle j|\vec{L}|i\rangle.$$

Particular interest will be in the expression of the spin transfer coefficient that relates the expectation value of the ξ component of the xenon nuclear spin to that of the expectation value of the total angular momentum of the rubidium. That kind of transition will contribute to the spin transfer coefficient terms of the form,

5.69 $$\mathcal{g}_{ij}\left(K_\xi,F_\xi\right) = \langle i|K_\xi|j\rangle\langle j|F_\xi|i\rangle.$$

The states *i* and *j* are the eigenstate of the complete Hamiltonian; i.e., they contain the effect of the perturbation. They can be presented as the transformation of the non-perturbed states (the eigenstates of H_0), denoted by $|f,m_f,m_k\rangle_0$. The set of eigenvalues that label unambiguously the eigenstates of H_0 remain good labeling also for the perturbed states. Thus, by assuming that the effect of the perturbation is given by the operator *R*, one can label a general state *i* by [33],

5.70 $$|i\rangle = |f,m_f,m_k\rangle = R|f,m_f,m_k\rangle_0 .$$

The transformation *R* can be described as operating on the operator (namely, the observable) rather than on the states. Then instead of substituting eq. 5.70, one can substitute in eq. 5.68 the unperturbed states with the perturbed operators given by,

$$\tilde{Y} = R^{-1} Y R. \qquad 5.71$$

The perturbation (eq. 5.60) gives rise to a spin transfer coefficient that has off-diagonal angular momentum matrix elements. In other words, the matrix elements that appear in 5.69 connect eigenstates with different values of m_f (through the factor $\langle j|F_\xi|i\rangle$) and eigenstates with different values of m_k (through the factor $\langle i|K_\xi|j\rangle$). This can by demonstrated by adapting the second approach given by eq. 5.71. While the unperturbed operator contains only longitudinal terms (namely, the longitudinal component of the angular momenta), the perturbation introduces axial components to the angular momenta, which can be expressed in terms of the ladder operators [33].

Another factor that is absorbed in the spin transfer coefficient arrives from the operation of the evolution operators in eq. 5.62. The evolution for the complete system is given by,

$$U(t) = e^{-i\frac{Ht}{\hbar}}, \qquad 5.72$$

where for the transformation to the interaction picture, the unperturbed operator should appear in the exponent. The value of *t* should represent the duration in which the two atoms are bound to each other. However, there is an inherent uncertainty about the exact duration. In order to resolve it, the spin transfer coefficient should be integrated over time while each point in time should be factorized by the probability that the two atoms did not unbind from their bound state. An assumption should be made regarding the functional form of the density probability for such event, and thus it assumes the form,

$$P(t) = \frac{1}{\tau} e^{-\frac{t}{\tau}}, \qquad 5.73$$

where τ is the average time of the RbXe molecule lifetime. Accordingly, the contribution from each point in time should be multiplied by the weight $\frac{1}{\tau} e^{-\frac{t}{\tau}} dt$.

5.3.2.4 Angular Momentum Transitions

As the operator *R* can be expressed as a power series expansion in a small parameter that reflects the strength of the perturbation in comparison to a typical unperturbed energy gap, so it can be done to the perturbed operators [33].

The longitudinal components, $\tilde{K}_\xi$ and $\tilde{F}_\xi$ will possess terms such as $K_- F_+$ and $K_+ F_-$. The first describes a process with transitions where $\Delta m_F = 1$ and $\Delta m_K = -1$, while the second term describes a process with transitions where $\Delta m_F = -1$ and $\Delta m_K = 1$. By substituting other components of the angular momenta, one will obtain terms that correspond to the process where $\Delta m_F = 0$ and $\Delta m_K = 1$, or $\Delta m_F = 1$ and $\Delta m_K = 0$. Nevertheless, processes that give rise to transitions where $\Delta m_F \geq 2$ or $\Delta m_K \geq 2$ can be obtained by considering higher order terms in the power series expansion of *R*, but

those terms are negligibly small. A summary of the energy level splits according to their order of magnitude as well the possible transitions is given in figure 5.4.

The symmetry of the equations for the nuclear xenon polarization and the atomic rubidium polarization under interchanging the rubidium angular momentum with the xenon nuclear spin suggests that there is no one direction of the spin transfer preferred over the other. Hence the polarization of the xenon, which is formed by overpopulating the up state, for instance, will tend to equalize with the polarization of the rubidium that is based on the overpopulation of a certain spin state. The continuous pumping guarantees that the rubidium gas will maintain a certain level of polarization, although it will be deteriorated due to spin destructive processes, according to eq. 5.52. It will be mentioned again, that this idealistic description of the spin exchange is degraded significantly by other spin interactions ascribed to the rubidium, such as the spin-rotation interaction [55].

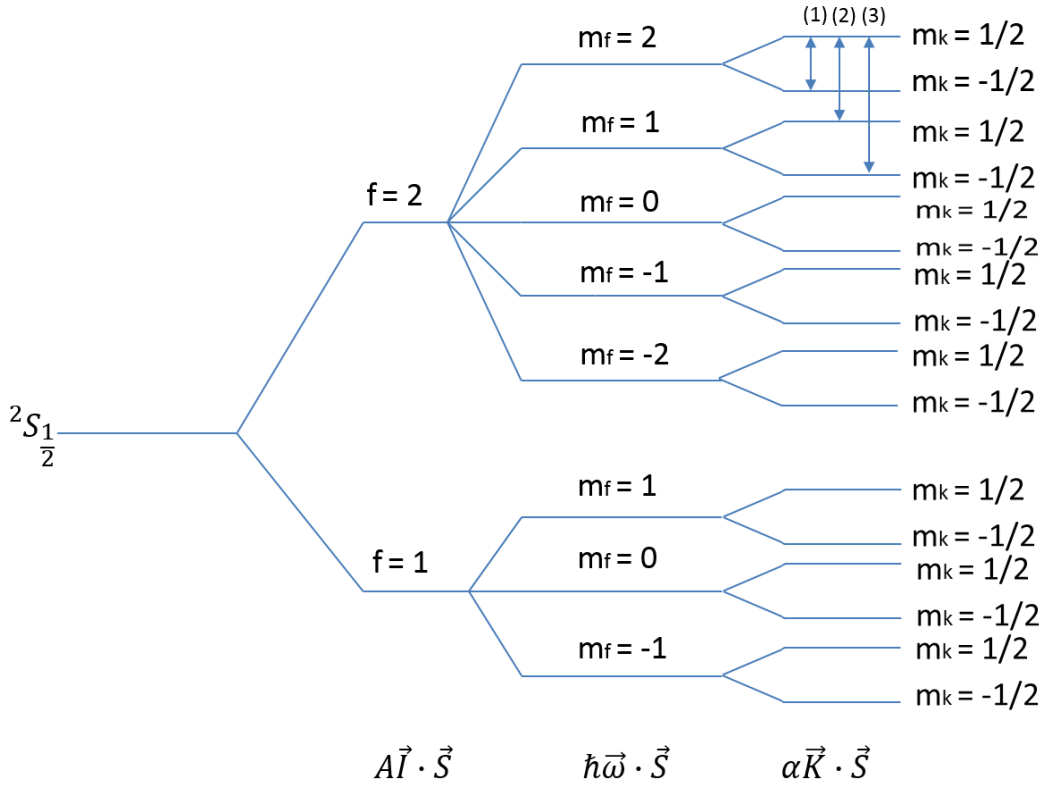

Figure 5.4. A state diagram of the splits in the energy levels due to the various spin interaction, for $I = \frac{3}{2}$ (^{87}Rb). The split of the largest order of magnitude is of the hyperfine structure (first split from the left). The next split is the effective Zeeman split of the rubidium atom, which is of a smaller order of magnitude, and the last split is of the smallest order of magnitude due to the interaction between the rubidium electronic spin and the xenon nuclear spin. The vertical arrows that connect the energy levels correspond to angular momentum transitions due to a certain collision, that change the ξ component quantum number of each one of the spins: (1) corresponds to $\Delta m_F = 0$ and $\Delta m_K = \pm 1$, (2) corresponds to $\Delta m_F = \pm 1$ and $\Delta m_K = 0$ and (3) corresponds to $\Delta m_F = 1$ and $\Delta m_K = -1$ or $\Delta m_F = -1$ and $\Delta m_K = 1$. (Based on [33]).

5.3.3 Binary collisions

5.3.3.1 Cross Section

The magnitude of the cross section between a rubidium atom and various types of noble gases atom, varies dramatically, and it has an immediate effect both on the noble gas polarization and the polarization's growing rate. The larger the cross section is, the larger the spin-transfer efficiency and the faster the growing rate [27].

As was stated in section 5.3.2.1, the term of the Hamiltonian that corresponds to the spin interaction between the rubidium atom and the xenon nucleus, has the form,

$$H_{SE} = \alpha \vec{K} \cdot \vec{S}. \qquad 5.74$$

The strength of the spin interaction, can be written as [56],

$$\alpha = \frac{16\pi}{3} g_n \mu_B \mu_n u_1^2(R) \eta^2, \qquad 5.75$$

where g_n is the xenon's nuclear gyro magnetic ratio, μ_B is the Bohr magneton, μ_n is the magnitude of the xenon's nuclear magnetic dipole, $u_1(R)$ is the rubidium valence electronic wave function, estimated at the location of the xenon nucleus (R being the inter-nuclear distance) and η is the enhancement factor that will be discussed shortly. The cross section is related to the expression in eq. 5.75, as it can be written as [56],

$$\sigma = \frac{2}{3}\left(\frac{8\pi g_n \mu_B \mu_n u_1^2(R) \eta^2 R^2}{3\hbar \bar{V}}\right)^2 I(I+1)\sigma_{kin}\,, \qquad 5.76$$

where $\sigma_{kin} = \pi R^2$ and $\bar{V}$ is the mean thermal relative velocity. Hence the cross section is one of the parameters that determine the strength of the interaction [59].

5.3.3.2 Enhancement Factor

The enhancement factor is a correction to the wave function that emerges due to the Pauli principle. Assuming that the wave function of each of the noble gas' electrons is an s-wave (zero orbital angular momentum), each one of the electron, taken separately, will have a non-zero probability to be found in the vicinity of the xenon nucleus. That fact, along with the restrictions posed by the Pauli principle, influence the wave function of the rubidium's valance electron (heuristically, it pushes it away from the xenon nucleus). That influence is formulated by the expression,

$$\eta(R) = 1 - \sum_{i=2}^{n} \frac{\langle i|1\rangle u_i(R)}{u_1(R)}\,. \qquad 5.77$$

That factorizes the wave function of the rubidium's valance electron. The summation is over all the noble gas atom's electrons. The summation term largely increases the absolute value of η. For example, η assumes values of -7, 9, 17, and -23 for helium, neon, krypton and xenon respectively. Since the cross

section is proportional to the fourth power of η (see eq. 5.76), the enhancement in the case of xenon with respect to the enhancement in the case of helium is almost 117 fold greater [56].

5.3.4 Three-Body Collisions

Generally, the molecular lifetime depends on the identity of the gas needed to be polarized, which is usually noble gas. For the purposes of MRI, helium and xenon are usually used. For more compact atoms, such as helium, the cross section for a collision with rubidium atoms is relatively low, and the probability for forming a long-lived molecule with a rubidium atom is negligible. In that case, the bound state will persist for the order of a magnitude of 10^{-12} [33]; thus, apart from formally speaking, one can no longer describe the spin exchange occurring through a meta-stable molecule. Xenon, on the other hand, by having larger polarizability interacts more substantially electrostatically with the rubidium, thus forming a deeper potential well, giving rise to a more stable molecular bound state. The bound state can be even more stable if the collision occurs in the presence of a third body buffer gas.

5.3.4.1 Evidence for the Existence of Van-Der-Waals (VDW) Molecules

The effect of the buffer gas on the stability of the RbXe molecule was demonstrated experimentally [57]. It is presented from the point of view of the rubidium polarization relaxation, based on the assumption that the major contribution to the relaxation stems from the collisions with xenon atoms (and wall collisions that can be disregarded, since it can be isolated from the spin exchange relaxation with the xenon). The dependence of the rubidium relaxation on the magnetic field reveals the mechanism leading to the spin exchange. The rubidium spin relaxation is proportional to a term of the form, $\Delta B_0^2/(\Delta B_0^2 + B^2)$, where ΔB_0 correspond to a Larmor period that matches the correlation time. Should the spin exchange occur through fast collisions, no field dependence will exist, since the magnetic field can suppress the relaxation only if the spin interaction persists for the time duration of the Larmor period. The correlation time associated with ΔB_0 was found to be depended on the buffer gas density, which suggests that the RbXe molecules were also formed by three-body collisions with the buffer gas. The explicit dependence of the rubidium relaxation on the buffer gas density will be shown in section 5.3.5.

The dependence of the rubidium relaxation on the buffer gas density conceals the possibility that the xenon will be polarized by the formation of quasi-stable molecules through three-body collisions

5.3.4.2 Semi-Classical molecular energy states

The number of xenon atoms (or rubidium) in a bound state can be evaluated quantitatively, using semi-classical considerations [58]. In the first stage, the number of available energy states will be assessed. Then, according to the occupancy distribution in thermal equilibrium, one can assess the number of atoms in a bound state.

As a first stage, a system of two particles is described. A collision between atoms can be formulated by writing a semi-classical potential in the center-of-mass coordinates,

5.78 $$U(r) = u(r) + \frac{L^2}{2mr^2} = u(r) + \frac{N(N+1)\hbar^2}{2mr^2},$$

where $u(r)$ is any attractive potential originating in the electrostatic property of the particles. The second term is known as the centrifugal term with *N* being any nonnegative integer. *L* is the angular momentum which assumes the form $N(N+1)\hbar^2$. Above certain value of N, the centrifugal barrier does not permit the formation of bound states. Hence, the value of N determines which type of collision is possible: for large values of N, no bound state can exist; this limit permits only fast collisions, where the spin-dependent potential has a little effect. For medium values of N, a minimum point can be formed in the potential curve, and below certain value of N, denoted by N_{max}, bound ground states exist. The bound states can be found by applying the Bohr-Sommerfeld quantization, by which the energies are calculated by integration in the phase space,

5.79 $$2\pi\hbar\left(n+\frac{1}{2}\right) = 2\int_{r_1}^{r_2}\left[2m\left(E(n,N) - u(r) - \frac{N(N+1)\hbar^2}{2mr^2}\right)\right]^{\frac{1}{2}} dr,$$

where $E(n,N)$ is the quantized energies and n is a nonnegative integer. The momentum is expressed in the integrand in terms of the total energy and the potential energy. By solving 5.79 for $E(n,N)$ one obtains,

5.80 $$E(n,N) = E_n + \frac{N(N+1)\hbar^2}{2I(n)},$$

where $I(n)$ is the moment of inertia. Since the first term in 5.80 is independent of N, namely the rotational motion, it can be associated with the vibration modes of the molecule. Regardless of 5.80, the combined system has a maximal energy state, above which the atoms are not bound, or equivalently, the collision is classified to be at the fast collision regime. The smaller the value of N is, the larger the centrifugal barrier and the larger the number of bound states (each labeled by n). Larger values of *N* correspond to a more classical behavior resembling two billiards balls that bounce off each other.

The probability that an incoming particle will tunnel through the centrifugal barrier depends on the height of the barrier. However, generally, it is small, unless the incoming particle possesses energy that corresponds to the energy of one of the bound states. This well-known concept in scattering theory is termed resonance [36]. In the context of scattering theory, the time duration that the resonance persists is referred to as "dwell-time." In the current context, it is the lifetime of the molecule. This duration can be evaluated by calculating the tunneling probability. Above certain values of *N*, that time is finite and converges to zero with increasing values of *N*. However, for very small values of N, bound states with negative energy may be formed in which the bound state is sustained infinite amount of time, since no tunneling can occur from a negative energy state. On the other hand, those states would not be available to an incoming particle; however, they can become occupied in the presence of a third particle, i.e. via a three-body collision. As a result of that kind of collision, the third particle is in an unbound state, and the incoming particle occupies one of the bound states of negative energy, and forms a quasi-stable molecule with the particle at rest (at the appropriate frame of reference). Since in that case no probability of tunneling out of the bound state exists, the only way in which the molecule

will break apart is by a successive collision with a third particle. Hence, that kind of process leads to the maximal molecular lifetime [58].

5.3.4.3 Bound States Occupancy

The qualitative description above enables a crude statistical argumentation that provides an estimate regarding the fraction of rubidium (or xenon) atoms that participate in a Van Der Waals (VDW) molecule with a xenon (or rubidium) atom. The number of RbXe molecules in the *n* energy state having an $N(N+1)\hbar$ angular momentum, can be estimated by [58],

$$5.81 \qquad s(n,N) = N_{Rb}N_{Xe}p(n,N),$$

where N_i is the number of atoms of the i species, and $p(n,N)$ is the probability that the state is occupied. Considering N as the orbital angular momentum quantum number, it is $2N+1$ times degenerate. Thus the expression for the probability, assuming thermal equilibrium, is given by,

$$5.82 \qquad p(n,N) = \frac{(2N+1)e^{-E(n,N)\beta}}{\sum_j g_j e^{-E_j\beta}},$$

where $\beta^{-1} = k_b T$ (Boltzmann constant times the temperature) and g_j is the degeneracy of the j energy level. The summation is only formal, since the energy levels for unbound states are practically continuous. In fact, the value of the integration over all the continuous states,

$$5.83 \qquad Z_c = V\left(\frac{1}{2\pi\hbar}\right)^3 \int d^3p e^{-\frac{p^2\beta}{2m}} = V\lambda_T^{-3}$$

(where V is the volume of the cell) is much larger than the number of discrete states [58]. Hence the number of discrete states are neglected, and 5.82 becomes,

$$5.84 \qquad p(n,N) = V^{-1}\lambda_T^3(2N+1)e^{-E(n,N)\beta},$$

Where,

$$5.85 \qquad \lambda_T = \hbar\left(\frac{2\pi\beta}{m}\right)^{\frac{1}{2}}.$$

For a xenon and rubidium mixture, $\lambda_T = 1.4\cdot 10^{-11}m$ [58]. Summation over all the bound states in equation 5.81 and division by the number of rubidium atoms, while exploiting 5.83, gives a formal expression for the required ratio of the number of RbXe molecules to the number of rubidium atoms. Denoting the number of RbXe molecules density by n_{RbXe}, that expression is,

$$5.86 \qquad \frac{n_{RbXe}}{N_{Rb}} = N_{Xe}V^{-1}\lambda_T^3\sum_{n,N\le N_{max}}(2N+1)e^{-\frac{E(n,N)}{\tau}}.$$

At T=300 ^{0}K and krypton at pressure of 1 Atm, that ratio was evaluated as $3.56\cdot 10^{-3}$ [58] for the rubidium-krypton pair. Given the larger cross section for rubidium and xenon atoms [27,56], that value can be regarded as the minimum limit, and the ratio can be assumed to be of the order of 10^{-3}.

5.3.5 Phenomenology

To conclude the statements above, there are two channels by which the spin exchange can occur: (1) By binary collisions, no stable molecular bound state can be formed and the spin-exchange rate is related to the cross-section by [61],

$$5.87 \qquad T_{SE,binary}^{-1} = [Rb]\langle\sigma v\rangle,$$

where v is the relative velocity and the bracket signifies the average of the cross section with respect to all thermal velocities. (2) In the presence of a buffer gas (nitrogen and xenon itself can serve as such), in contrast to eq. 5.87, the spin exchange rate becomes dependent on the formation of relatively stable RbXe molecules. Those molecules are relatively stable in the sense that they will break apart only in the case of a successive three-body collision with a buffer gas atom or molecule.

As was demonstrated (see section 5.3.4.3), the existence of such occupied bound states is non-negligible for noble gas partial pressure at 1 Atm. The spin transfer occurring through the three-body collision channel may be more efficient in comparison to the two-body collision spin transfer due to the larger timescale in which the rubidium and the xenon are bound together. The strength of the hyperfine interaction between the rubidium's valance electron and the xenon nuclear spin is of the order of magnitude of a few tens of MHz [33]. Thus the duration required for the interaction to be effective[18] is of the order of 10^{-7} s. That makes the RbXe molecules that were formed by a three-body collision particularly qualified for spin transferring, whereas unstable RbXe molecules formed by a two-body collision persist only for 10^{-12}, a fact that significantly reduces the spin-transfer probability.

The spin exchange rate for the spin exchange channels (binary and three-body collision) can be written as proportional to [61],

$$5.88 \qquad \frac{1}{T_{SE}} \sim \frac{1}{T_k}\left(\frac{\alpha\tau}{\hbar}\right)^2,$$

where T_k^{-1} is the formation rate of RbXe molecules per molecule, either by a two or three-body collision. The appearance of α can be inferred from the fact that the spin exchange will be proportional to the square of the interaction term in eq. 5.74, and the appearance of τ can be inferred from the previous paragraph. Moreover, for both of the cases, the spin exchange will be proportional to the rubidium density. However, for the spin exchange resulting from three-body collisions, there is a dependence on the buffer gas or the xenon gas densities from all its isotopes, since any xenon atom may participate in a collision as a third body [61]. Above a certain buffer gas pressure (of about 0.4 Atm for xenon [61], and 0.015 Atm for nitrogen [52]), further increase in the buffer gas pressure will slow down the spin exchange rate since the buffer gas atoms are also responsible for the molecules' unbinding, which is a

[18] The frequency associated with the interaction can be regarded as the Rabi frequency of the oscillation between two spin configurations: in one configuration, one spin is in the up state and the other is in the down state, and in the other configuration, it is the opposite. Hence, given an initial state at one spin configuration, the duration after which the system will transform into the other configuration is a quarter of the Rabi period. The transition between the two-spin configurations is analogous to the spin transfer.

time inversion of the process of their formation. Thus, higher buffer gas pressure will shorten the molecular lifetime and consequentially deteriorate the spin transfer efficiency.

5.4 Spin Relaxation

When the pumping light is turned off, the last term in eq. 1.18 is zero, and the solution for the new differential equation, given a maximal polarization at t=0, is,

$$p_{xe}(t) = p_{xe}(0)e^{-\Gamma t}. \quad (5.89)$$

This section looks at the polarization relaxation rate, which by inspecting eq. 5.89 can be identified as the polarization decay constant.

Generally, the relaxation contributors are divided into two groups: the first composed of intrinsic terms, i.e., terms that are associated with interactions of the xenon atoms among themselves, and the second composed of extrinsic terms, i.e., all the terms that are not included in the first group [68].

5.4.1 Intrinsic Spin Relaxation

5.4.1.1 Persistent and Transient Dimers

The mechanism of intrinsic xenon polarization relaxation is analogous to the mechanism of the rubidium polarization relaxation due to the spin-rotation interaction. The analogy is extended as the different channels of short-lived molecular formation are considered.

In the case of intrinsic relaxation, the terminology in the literature refers to relaxation via the formation of a transient xenon dimer, which results from Xe-Xe binary collisions, as transient relaxation, and to the relaxation via the formation of a persistent xenon dimer that results from VDW molecule, as persistent relaxation [68]. Xenon dimer is a Xe_2 molecule, that similar to a RbXe molecule, can be formed as an outcome of a collision between two Xe atoms with or without the presence of a third particle. As was pointed out regarding the RbXe collision, the xenon dimer that is formed in a binary collision has a very short lifetime (similar to RbXe molecule – about 10^{-12} seconds) and hence is called transient dimer, whereas the dimer that is formed in a three-body collision persists as long as no successive collision with a third body has occurred; hence, it is called persistent dimer. The formation of a persistent dimer is by no means a negligible phenomenon in a low pressure regime. For example, at the conditions of 1 amagat, the ratio of the number of xenon dimers (the transient dimers can be neglected) to the total number of Xe atoms was estimated at about 0.5% [68].

The range of pressure where the formation of VDW xenon dimer molecules can occur includes higher pressure value in comparison with RbXe molecules. Thus, under the conditions of SEOP experiments, persistent dimer relaxation is dominant over transient-dimer relaxation [69].

5.4.1.2 Persistent Dimers

There are three factors that constitute the persistent dimer relaxation rate [68]: (1) the fraction of xenon atoms bound in a VDW molecule, which is expressed by $\kappa_{Xe}[Xe]$, where κ_i is the chemical equilibrium coefficient, where *i* is the buffer gas; (2) the squared interaction strength, which is composed out of two contributions. One of them originates in the chemical shift anisotropy (CSA) term in the Hamiltonian, and is significant only at a high external magnetic field, and thus can be ignored. The other contribution originates in the spin-rotation interaction between the xenon nuclear spin and the molecular angular momentum, analogically to the spin-rotation interaction discussed in the context of RbXe; and (3) the third factor is referred to as the power spectrum of magnetic fluctuations [70] that depends on the correlation time and the xenon nuclear Larmor frequency, Ω. To conclude, in the case where only xenon serves as the buffer gas, the persistent relaxation rate can be written as,

$$\Gamma_p^{Xe} = (2\kappa_{Xe}[Xe])(M^{sr} + M^{csa})\left(\frac{\tau}{1+\Omega^2\tau^2}\right). \quad 5.90$$

Hence it is clear that the persistent relaxation is independent of the xenon density.

By introducing into the cell different kinds of buffer gases, there will be an additional factor to eq. 5.90. To conclude, in the presence of buffer gas, the spin relaxation due to persistent dimers is modified according to [71],

$$\Gamma_p = \frac{\Gamma_p^{Xe}}{1+\frac{k_{N_2}[N_2]}{k_{Xe}[Xe]}}. \quad 5.91$$

Theoretically, the expression in eq. 5.90 should be constant as a function of the temperature (there is a temperature dependence in the two first factors that cancel each other). However, an unexplained inverse quadratic relation was found experimentally [69].

5.4.2 Extrinsic Spin Relaxation

The relaxation caused by any factor besides the xenon gas itself, is considered as extrinsic relaxation.

5.4.2.1 Wall Relaxation

Collisions of xenon atoms with the walls of the SEOP cell constitute another source of xenon polarization relaxation. Analogically to intrinsic relaxations, a correlation time and a spin transfer process are involved in wall collisions. In this case, however, the xenon nuclear spin may interact with a larger variety of the non-zero-spin particles, or particles possess a magnetic moment that make up the wall. For a low field, the xenon polarization relaxation is mainly due to dipolar interaction with hydrogen [72]. Although it is possible to divide the spin interactions during wall collisions to nucleus-nucleus spin interactions and nucleus-electron spin interactions [64], the interaction between two nuclear spins is negligible in comparison to the nucleus-electron spin interaction, due to the larger magnetic moment of the electron. In order to minimize the wall relaxation the cell can be coated with an anti-relaxation layer, reducing the processes that were described.

Another consideration regarding wall relaxation is geometric. Constructing a cell with a minimum surface-to-volume ratio will minimize the wall relaxation. Naturally, it is impractical to use a spherical cell for SEOP experiments, due to illumination efficiency considerations. Nevertheless, a cylindrical shape with rounded basis serves as the preferable compromise (see figure 2.6).

5.4.2.2 Magnetic Field Inhomogeneity

The relaxation rate associated with the magnetic field inhomogeneity at high pressure can be written as [73],

$$\Gamma_{\nabla B} = D\frac{\left|\vec{\nabla}B_{\perp}\right|^{2}}{B_{0}^{2}}, \qquad 5.92$$

Where *D* is the diffusion coefficient, B_0 is the magnitude of the longitudinal magnetic field, and $B_{\perp}$ is the magnetic field magnitude on the transverse plane. The relaxation rate in eq. 5.92 is pressure dependent through the diffusion coefficient. Higher total cell pressure results in a shorter average time between collisions, causing a decrease in the diffusion coefficient. Therefore, higher pressure may reduce the relaxation rate due to field inhomogeneity.

5.4.2.3 Dipolar Interactions

Molecules that possess strong magnetic moment give rise to spin polarization destruction. In the context of the SEOP experiment, oxygen is the relevant molecule that possesses such a property. The interaction between the xenon nuclear spin and the molecular magnetic moment of the oxygen (dipolar interaction) enhances significantly the xenon spin relaxation. Thus, as was elaborated on in section 2, much effort is made to minimize the presence of oxygen anywhere the hyperpolarized gas reaches.

Another dipolar interaction is the one between the xenon nuclear spin and an electronic spin, such as that of the rubidium valance electron. This kind of interaction was discussed in section 5.3, although the spin transfer in that case resulted in gaining xenon polarization. However, a remnant of rubidium that becomes unpolarized after the SEOP process may be another source of xenon depolarization. Moreover, poor SEOP cell illumination results in areas with low or zero rubidium polarization [74], where the effect of the rubidium on the xenon polarization will be destructive. Nevertheless, most of the spin relaxation during collisions between xenon and rubidium atoms is due to the spin rotation interaction [75].

C. References

[1] Magnetic Resonance Imaging - Physical Principles and Sequence Design; Robert W. Brown, Yu-Chung N. Cheng, E. Mark Haacke, Micheal R. Thompson, Ramesh Venkatesan; 2014.

[2] Ray H. Hashemi, William G. Bradley Jr., Christopher J. Lisanti; MRI the Basics; 2010.

[3] A. Abragam; Principles of Nuclear Magnetism; 1961.

[4] Malcolm H. Levitt; Spin Dynamics – Basics of Nuclear Magnetic Resonance; 2007.

[5] Karl Blum; Density Matrix Theory and application (Second edition); 2010.

[6] Dwight G. Nishimura; Principles of Magnetic Resonance Imaging; 2010.

[7] Charles Kittel; Introduction to Solid State Physics (8^{th} edition); 2005.

[8] Marcus J. Couch, Barbara Blasiak, Boguslaw Tomanek, Alexei V. Ouriadov, Matthew S. Fox, Krista M. Dowhos, Mitchell S. Albert; Hyperpolarized and Inert Gas MRI: The Future; Molecular Imaging and Biology; 2014.

[9] Boyd M. Goodson; Nuclear Magnetic Resonance of Laser-Polarized Noble Gases in Molecules, Materials, and Organisms; Journal of Magnetic Resonance; 155 157-216; 2002.

[10] Albert MS, Cates GD, Driehuys B, Happer W, Saam B, Springer CS, Wishnia A; Biological magnetic resonance imaging using hyperpolarized 129Xe; Nature; 370:199; 1994.

[11] Eduard E. de Lange, John P. Mugler, James R. Brookeman, Jack Knight-Scott, Jonathon D. Truwit, C. David Teates, Thomas M. Daniel, Paul L. Bogorad, and Gordon D. Cates; Lung Air Spaces: MR Imaging Evaluation with Hyperpolarized 3He Gas; Radiology; 210(3); 1999.

[12] Sven Mansson, Jan Wolber, Bastiaan Driehuys, Per Wollmer, Klaes Golman; Characterization of Diffusing Capacity and Perfusion of the Rat Lung in a Lipopolysaccaride Disease Model Using Hyperpolarized 129Xe; Magnetic Resonance in Medicine; 50:1170–1179, 2003.

[13] Marcus J. Coucha, Iain K. Ball, Tao Li, Matthew S. Fox, Alexei V. Ouriadov, Birubi Biman, Mitchell S. Albert; Inert fluorinated gas MRI: a new pulmonary; NMR in Biomedicine; 2014.

[14] Fain SB, Korosec FR, Holmes JH, O'Halloran R, Sorkness RL, Grist TMl; Functional lung imaging using hyperpolarized gas MRI; Journal of Magnetic Resonance Imaging ;25(5):910-23; 2007.

[15] Zackary I. Cleveland, Rohan S. Virgincara, Yi Qi, Scott H. Robertsona, Simone Degana, Bastiaan Driehuys; 3D MRI of impaired hyperpolarized 129Xe uptake in a rat model of pulmonary fibrosis; NMR in biomedicine; 2014.

[16] Bastiaan Driehuys, Gary P. Cofer, Jim Pollaro, Julie Boslego Mackel, Laurence W. Hedlund, G. Allan Johnson; Imaging alveolar– capillary gas transfer using hyperpolarized 129Xe MRI; PNAS; 103(48) 18278–18283; 2006.

[17] Abe C. Thomas, John C. Nouls, Bastiaan Driehuys, James W. Voltz, Boma Fubara, Julie Foley, J. Alyce Bradbury, and Darryl C. Zeldin; Ventilation Defects Observed with Hyperpolarized 3He Magnetic

Resonance Imaging in a Mouse Model of Acute Lung Injury; American Journal of Respiratory Cell and Molecular Biology; 44 648–654; 2011.

[18] Marcus J. Couch; Regional Ventilation Mapping Of The Rat Lung Using Hyperpolarized ^{129}Xe Magnetic Resonance Imaging; MSc Thesis; University of Western; 2011.

[19] Zackary I. Cleveland, Gary P. Cofer, Gregory Metz, Denise Beaver, John Nouls, S. Sivaram Kaushik, Monica Kraft, Jan Wolber, Kevin T. Kelly, H. Page McAdams, Bastiaan Driehuys; Hyperpolarized ^{129}Xe MR Imaging of Alveolar Gas Uptake in Humans; Plos One (available online; 2010.

[20] Kasim Abul-Kasim, Majda Thurnher, Stefan Puchner, Pia Sundgren; South African Journal of Radiology; 17(1); 2013.

[21] Mary L. Mazzanti, Ronn P. Walvick, Xin Zhou, Yanping Sun, Niral Shah, Joey Mansour, Jessica Gereige, Mitchell S. Albert; Distribution of Hyperpolarized Xenon in the Brain Following Sensory Stimulation: Preliminary MRI Findings; PLoS One (freely, available online) 6(7); 2011.

[22] Mitchell S. Albert, Dilip Balamore, Daniel F. Kacher, Arvind K. Venkatesh, Ferenc A. Jolesz; NMR in Biomedicine; Hyperpolarized 129Xe T1 in oxygenated and deoxygenated blood; 13 407-414; 2000

[23] Mitchell S. Albert, Victor D. Schepkin, and Thomas F. Budinger; Journal of Compliler Assisled Tomography; Measurement of 129Xe T 1 in Blood to Explore the Feasibility of Hyperpolarized 129Xe MRI**;** 19(6) 975-978, 1995.

[24] Mikhail G. Shapiro, R. Matthew Ramirez, Lindsay J. Sperling, George Sun, Jinny Sun, Alexander Pines, David V. Schaffer, Vikram S. Bajaj; Genetically encoded reporters for hyperpolarized xenon magnetic resonance imaging; Nature Chemistry; Published Online; 2014.

[25] Witte C, Martos V, Rose HM, Reinke S, Klippel S, Schroder L, Hackenberger CP; Live-cell MRI with xenon hyper-CEST biosensors targeted to metabolically labeled cell-surface glycans; PubMed.gov; 23;54(9):2806-2810; 2015.

[26] R. C. Greenhow; Optical Pumping in He-3; Physical Review; 136 A660; 1964.

[27] Thad G. Walker, William Happer; Spin-exchange optical pumping of noble-gas nuclei; RMP; 69(2) 629-642; 1997.

[28] Kevin Knagge, Jonathan Prange, Daniel Raftery; A continuously recirculating optical pumping apparatus for high xenon polarization and surface NMR studies; Chemical Physics Letters; 397 11–16; 2004.

[29] Muhammad G. Mortuza, Satyanarayana Anala, Galina E. Pavlovskaya, Todd J. Dieken, and Thomas Meersmann; Spin-exchange optical pumping of high-density xenon-129; Journal of Chemical Physica; 118(4) 1581-1586; 2003.

[30] Anthony L. Zook, Bhavin B. Adhyaru, and Clifford R. Bowers; High capacity production of >65% spin polarized xenon-129 for NMR spectroscopy and imaging; Journal of Magnetic Resonance; 159 175–182; 2002.

[31] Iulian C. Ruset; Hyperpolarized 129Xe Production and Applications; PhD Thesis; University of Bucharest; 2005.

[32] M Chaichian, R Hagedorn; Symmetries in Quantum Mechanics; 1998.

[33] W. Happer, E. miron, S. Schaefer, D. Schreiber, W. A. van Wijngaarden, X. Zeng; Polarization of the nuclear spins of noble-gas atoms by spin exchange with optically pumped alkali-metal atoms; Physical Review A; 29(6) 3092-3110; 1984.

[34] William Happer; Optical Pumping; Review of Modern Physics; 14(2) 169-250; 1972.

[35] Marcis Auzinsh, Dmitry Budker, Simon M. Rochester; Optically Polarized Atoms; 2010.

[36] J. J. Sakurai; Modern Quantum Mechanics (Revised edition); 1994.

[37] N. D. Bhaskar, J. Camparo, W. Happer, A. Sharms; Light narrowing of magnetic resonance lines in dense, optically pumped alkali-metal vapor; Physical Review A; 23(6) 3048-3065; 1981.

[38] N. Whiting, P. Nikolaou, N.A. Eschmann, N.J. Barlow, R. Lammert, J. Ungar, W. Hu, L. Vaissie, B.M. Goodsom; Using frequency-narrowed, tunable laser diode arrays with integrated volume holographic grating for spin-exchange optical pumping at high resonant fluxes and xenon densities; Applied Physics B; 106,775-788; 2012.

[39] P. Nikolaou, N. Whiting, N. A. Eschmann, K. E. Chaffee, B. W. Goodson, M. J. Barlow; Generation of laser-polarized xenon using fiber-coupled laser-diode arrays narrowed with integrated volume holographic gratings; Journal of Magnetic Resonance; 197, 249-254; 2009.

[40] Henry Margenau, William W. Watson; Pressure effects on spectral lines; 8 22-55; 1936.

[41] P. W. Anderson; A method of synthesis of the statistical and impact theory of pressure broadening; Physical Review; 68(809); 1952.

[42] R. E. Walkup, A Spielfiedel, D.E. Pritchard; Observation of non-lorentzien spectral line shapes in Na-noble-gas systems; Physical Review Letters; 45(12) 986-990; 1980.

[43] Antoine Royer; Expansion of the spectrum in power of the density in the adiabatic theory of pressure broadening; 3(6) 2044-2050; 1971.

[44] Shang-Yi Ch'en, Makoto Takeo; Broadening and shift of spectral lines due to the presence of foreign gases; Review of Modern Physics; 59(1) 20-77; 1957.

[45] Jozef Szudy, William E. Baylis; Profiles of line wings and rainbow satellites associated with optical and radiative collisions; Physics Reports; 266 127-227; 1996.

[46] Wm. R. Kearney, K.M. Sando; Classical-path theory for broadening of atomic lines by diatomic perturbers; Physical Review A; 46(11) 6977-6987; 1992.

[47] Andrew Zangwill; Modern Electromagnetism; 2012.

[48] B. S. Mathur, H. Y. Tang, W. Happer; Light propagation in optically pumped alkali vapors; Physical Review A; 2(3) 648-661; 1970.

[49] M. E. Wagshul, T. E. Chupp; Laser optical pumping of high-density Rb in polarized ^{3}He targets; Physical Review A; 49(5) 3854-3869; 1994.

[50] W. Happer, W.A. Van Wijngaarden; An optical pumping primer; Hyperfine interaction; 38 435-470; 1987.

[51] C. C. Bouciat, M. A. Bouchiat, C. L. Pottier; Evidence for Rb-rare-gas molecules from the relaxation of polarized Rb atoms in a rare gas. Theory; Physical Review; 181(1) 144-165; 1969.

[52] X. Zeng, Z. Wu, T. Call, E. Miron, D. Schreiber, W. Happer; Experimental determination of the rate constants for spin exchange between optically pumped K, Rb, and Cs atoms and ^{129}Xe nuclei; Physical Review A; 31(1) 260-279 ;1985.

[53] W. Happer, B. S. Mathur; Effective operator formalism in optical pumping; Physical Review; 163(1) 12-25; 1967.

[54] M. V. Romalis, E. Miron, G.D. Cates; Pressure broadening of Rb D_1 and D_2 lines by ^{3}He, ^{4}He, N_2 and Xe: Line cores and near wings; Physical Review A; 56(6) 4569-4578; 1997.

[55] I. A. Nelson, T. G. Walker; Rb-Xe spin relaxation in dilute Xe mixtures; Physical Review A; 65 012712(1-6); 2001.

[56] R.M. Herman; Theory of Spin Exchange between Optically Pumped Rubidium and Foreign Gas Nuclei; Physical Review; 137(4A) A1062-A1065; 1965.

[57] N. D. Bhaskar, W, Happer, M. Larsson, X. Zeng; Slowing Down of Rubidium-Induced Nuclear Spin Relaxation of l29Xe Gas in a Magnetic Field; Physical Review Letters; 50(2) 102-105; 1983.

[58] Z. Wu, T. G. Walker, W. Happer; Spin-rotation interaction of noble-gas alkali-metal atom pairs; Physical Review Letters; 54(17) 1921-1925; 1985.

[59] C. H. Volk, T. M. Kwon, J. G. Mark; Measurement of the Rb-^{129}Xe spin-exchange cross section; Physical Review A; 21(5) 1549-1555; 1980.

[60] S. Appelt, A Ben-Amar Baranga, C. J. Erickson, M. V. Romalis, A. R. Young, W. Happer; Theory of spin-exchange optical pumping of ^{3}He and ^{129}Xe; Physical Review A; 58(2) 1412-1440; 1998.

[61] G. D. Cates, R. J. Fitzgerald, A. S. Barton, P. Bogorad, M. Gatzke, N. R. Newbury, B. Saam; Rb-^{129}Xe spin-exchange rates due to binary and three-body collisions at high Xe pressures; Physical Review A; 45(7) 4631-4639; 1992.

[62] S.R. Schaefer, GD Cates, W. Happer; Determination of spin-exchange parameter between optically pumped rubidium and ^{83}Kr, Physical Review A, 41(11) 6063; 1990.

[63] Nicholas Whiting, Panayiotis Nikolaou, Neil A. Eschmann, Boyd M. Goodson, Michael J. Barlow; Interdependence of in-cell xenon density and temperature during Rb/Xe-129 spin-exchange optical pumping using VHG-narrowed laser diode arrays; Journal of Magnetic Resonance; 208 298-304; 2011.

[64] Panayiotis Nikolaoua, Aaron M. Coffeya, Laura L. Walkup, Brogan M. Gust, Nicholas Whiting, Hayley Newton, Scott Barcus, Iga Muradyan, Mikayel Dabaghyan, Gregory D. Moroz, Matthew S. Rosen,i, Samuel Patz, Michael J. Barlow, Eduard Y. Chekmenev, Boyd M. Goodson; Near-unity nuclear polarization with an open-source ^{129}Xe hyperpolarizer for NMR and MRI; PNAS; 110(35) 14150-14155; 2013.

[65] Panayiotis Nikolaou, Aaron M Coffey, Laura L Walkup, Brogan M Gust, Cristen D LaPierre, Edward, Koehnemann, Michael J Barlow, Matthew S. Rosen, Boyd Mclean Goodson, Eduard Y Chekmenev; A 3D-Printed High Power Nuclear Spin Polarizer; Journal of the American Chemical Society; 2014.

[66] Panayiotis Nikolaou, Aaron M Coffey, Kaili Renta, Laura L Walkup, Brogan M Gust Michael J Barlow, Matthew S. Rosen, Boyd Mclean Goodson, Eduard Y Chekmenev; Multidimensional mapping of the spin-exchange optical pumping in clinical-scale batch-mode ^{129}Xe hyperpolarizers; The Journal of Physical Chemistry B; 118 4809-4816; 2014.

[67] Panayiotis Nikolaou, Aaron M. Coffey, Laura L. Walkup, Brogan M. Gust, Nicholas Whiting, Hayley Newton, Iga Muradyan, Mikayel Dabaghyan, Kaili Ranta, Gregory D. Moroz, Matthew S. Rosen, Samuel Patz, Michael J. Barlow, Eduard Y. Chekmenev, Boyd M. Goodson; XeNA: An automated 'open-source' 129Xe hyperpolarizer for clinical use; Magnetic Resonance Imaging; 32 541–550; 2014.

[68] B.N. Berry-Pusey, B. C. Anger, G. Laicher, B. Saam; Nuclear spin relaxation of ^{129}Xe due to persistent dimers; Physical Review A; 74 063408(1-9); 2006.

[69] B. C. Anger, G. Schrank, A Schoeck, K. A. Butler, M. S. Solum, R. J. Pugmire, B. Saam; Gas-phase spin relaxation of ^{129}Xe; Physical Review A; 78 043406(1-10), 2008.

[70] N. Bloembergen, E. M. Purcell, R. V. Pound; Relaxation Effects in Nuclear Magnetic Resonance Absorption; 73(7) 679-712; 1948.

[71]B. Chann, I. A. Nelson, L. W. Anderson, B. Driehuys, T. G. Walker; ^{129}Xe-Xe Molecular spin relaxation; Physical Review Letters; 88(11) 113201(1-4); 2002.

[72] B. Driehuys, G. D. Cates, W. Happer; Surface relaxation mechanism of laser-polarized ^{129}Xe; Physical Review Letters; 74(24) 4943-4946; 1995.

[73] G. D. Cates, S. R. Schaefer, W. Happer; Relaxation of spins due to field inhomogeneities in gaseous samples at low magnetic fields and low pressures; 37(8) 277-285; 1988.

[74] N.D. Bhaskar, M. Hou, B. Suleman, W. Happer; Propagating, Optical-Pumping Wave Front; Physical Review Letters, 43(7) 519-521; 1979.

[75] I. A. Nelson, T. G. Walker; Rb-Xe Spin Relaxation in Dilute Xe mixture; Physical Review A; 65 012712(1-6); 2001

[76] Thomas J. Killian; Thermionic phenomena caused by vapors of rubidium and potassium; Physical Review; 27 578-587; 1926

[77] Joel Mispelter, Mihaela Lupu, Andre Briguet; NMR Probeheads for biophysical and biomedical experiments; 2006.

D. List of figures

Figure 5.4. A state diagram of the splits in the energy levels due to the various spin interaction, for $I = \frac{3}{2}$ (^{87}Rb). The split of the largest order of magnitude is of the hyperfine structure (first split from the left). The next split is the effective Zeeman split of the rubidium atom, which is of a smaller order of magnitude, and the last split is of the smallest order of magnitude due to the interaction between the rubidium electronic spin and the xenon nuclear spin. The vertical arrows that connect the energy levels correspond to angular momentum transitions due to a certain collision, that change the z component quantum number of each one of the spins: (1) corresponds to $\Delta m_F = 0$ and $\Delta m_K = 1$, (2) corresponds to $\Delta m_F = 1$ and $\Delta m_K = 0$ and (3) corresponds to $\Delta m_F = 1$ and $\Delta m_K = -1$ or $\Delta m_F = -1$ and $\Delta m_K = 1$. (Based on [33]).

E. Abbreviations

CT	Computed Tomography
PET	Positron Emission Tomography
r.f.	Radio Frequency
FA	Flip Angle
SNR	Signal to Noise Ratio
CEST	Chemical Exchange Spin Transfer
FID	Free Induction Decay
MRI	Magnetic Resonance Imaging
fMRI	Functional Magnetic Resonance Imaging
ppm	Parts Per Million
FWHM	Full Width at Half Maximum
VDW	Van Der Waals
PMH	Powermeter Head
SEOP	Spin-Exchange Optical Pumping
ADC	Analog to Digital Convertor
TE	Echo Time
TR	Time to Recovery
NMR	Nuclear Magnetic Resonance
CNR	Contrast to Noise Ratio
HP	Hyperpolarized
CSA	Chemical Shift Anisotropy